



**Classificação de Hidrometeoros usando dados de
radar de dupla polarização para melhoria da
previsão numérica e assimilação de dados**

Relatório de Atividades

Processo 2016/16932-8

BCO - Pós-Doutorado / Fluxo Contínuo

Beneficiário: Jean-François Ribaud

Responsável: Dr. Luiz Augusto Toledo Machado

Período do Relatório: 1 de novembro de 2016 ao 31 de outubro de 2018

INTRODUÇÃO:

Este relatório descreve as atividades de pós-doutorado que o bolsista (processo 2016/16932-8) esteve envolvido entre ao 01/11/2016 e ao 31/10/2018 no âmbito do Projeto SOS-CHUVA no seio do Instituto Nacional de Pesquisas Espaciais (INPE), no Centro de Previsão de Tempo e Estudos Climáticos (CPTEC), na Divisão de Satélites e Sistemas Ambientais (DSA) em Cachoeira Paulista sob a direção de Luiz Augusto Toledo Machado.

Neste período de dois anos o objetivo principal do estudo foi desenvolver uma classificação de hidrometeoros para o radar banda X de dupla polarização. As classificações são todas realizadas para regiões de latitudes médias e esta classificação seria adaptada para a região tropical. Para tanto, foi necessária dispendir um longo período de desenvolvimento de uma técnica que não se baseia em limites pré-determinados, mas define as classes naturalmente para a região em estudo. Foi selecionado uma nova técnica baseada em agrupamentos, não supervisionada, que permitia definir classes de forma natural, sem existência de classes pré-definidas. Essa técnica foi inicialmente analisada para a Amazônia, onde existia um grande conjunto de dados auxiliares e de características pré conhecidas, principalmente em função dos voos de aeronaves e estudos durante o GoAmazon.

Com base na classificação e sua validação os estudos foram voltados a aplicação em diversas atividades voltadas a previsão imediata. Cita-se, a análise da evolução de hidrometeoros que antecedem as tempestades, a classificação de hidrometeoros para análise dos processos de eletrificação e consequente uso em assimilação de dados e finalmente, na análise dos hidrometeoros previstos pelos modelos com microfísica explícita e sua comparação com as observações de radares. Todos esses trabalhos foram ou estão sendo submetidos a revistas especializadas e a realização de Tese de Doutorado ou Mestrado.

Apresentamos abaixo uma descrição mais detalhada destes tópicos, contudo, podemos afirmar que esses estudos foram fundamentais para a evolução do projeto Temático.

1 - CLASSIFICACOES DOS HIDROMETEOROS

a) Desenvolvimento da técnica chamada “clustering”

Hoje em dia, novos radares equipados com dupla polarização permitem conseguir mais informações sobre as partículas que constituem as nuvens. Com quatro variáveis (contra somente uma para os radares “clássicos”), esses radares polarimétricos podem nos informar sobre o tamanho, a forma, a orientação e a fase dos hidrometeoros (conjunto de partículas de água líquida ou sólida em queda ou suspensão na atmosfera). Desde o surgimento desses radares, várias técnicas foram desenvolvidas para identificar diretamente o tipo do hidrometeoro dominante na nuvem.

Embora a classificação dos hidrometeoros a partir dos radares com dupla polarização seja muito conhecida desde os anos 2000, até no início do ano 2016 ainda nenhuma foi desenvolvida para as regiões tropicais. Assim optamos por desenvolver uma nova classificação dos hidrometeoros para as regiões tropicais brasileiras a partir do radar da banda X envolvido no projeto SOS-CHUVA.

A maioria das classificações (booleano, lógica fuzzy, entre outras) usam limites que podem ser específicos para cada hidrometeoro, cada região, ou ainda cada comprimento de onda. A metodologia de “unsupervised clustering” permite precisamente deixar toda a liberdade o conjunto dos dados polarimétricos sem nenhum a priori. Das principais metodologias de clustering, foi escolhido seguir o artigo de Grazioli et al 2015, que se baseia num tipo específico chamado “Agglomerative Hierarchical Clustering”. Nesta metodologia apresenta-se uma sequência de iterações que agrupem N objetos em n_c clusters fazendo com que os objetos de um mesmo cluster apresentem mais similaridades (físicas) que àqueles que pertençam dos outros. No início da metodologia, cada objeto corresponde a um cluster ($N = n_c$). Depois de uma iteração, fica sempre N objetos, mas separados desta vez dentro n_c-1 clusters. Essas iterações devem ser repetidas até que no final fiquem N objetos para somente um cluster. Posteriormente, o utilizador poderá escolher quando tiver a “melhor” distribuição entre clusters (por exemplo: 5, 6, ou mais clusters) com ferramentas estatísticas e sua interpretação pessoal.

Todas as informações sobre o desenvolvimento e as características dessa técnica de classificação são disponíveis no artigo em curso de publicação no Atmospheric Measurement Techniques (AMT) e apresentados no anexo 1.

b) Resultados do GO-AMAZON

Os dados polarimétricos usados foram coletados com o radar polarimétrico da banda X. Como a técnica de clustering precisa de muitos dados para aprender / se construir (data-driven) e considerando que no início desse trabalho havia poucos eventos no projeto de SOS-CHUVA, escolhemos desenvolver a técnica com os dados do projeto Go-Amazon ACRIDICON (mesmo radar) ocorrido em Manaus no ano de 2014 (Machado et al. 2017). Deve notar-se que como as regiões estratiformes e convectivas são caracterizadas pelas assinaturas dinâmica e microfísica diferentes, uma separação entre os dois foi feita no conjunto dos dados, assim como entre as estações chuvosa e seca.

Em geral, as regiões estratiformes são constituídas de 5 tipos de hidrometeoros: chuva fraca, chuva, água-neve, neve, e gelos, enquanto que as regiões convectivas são feitas de: chuva fraca, chuva moderada, chuva forte, graupels, neves, e gelos. A diferença principal entre as estações chuvosa e seca resulta da existência de dois tipos de graupels (baixa e alta densidade) na estação seca, nas regiões convectivas. Já na estação chuvosa observa-se somente um tipo geral de graupel. Por último, foi demonstrado que os hidrometeoros de neves e gelos são caracterizadas pelas assinaturas polarimétricas mais alta comparativamente as latitudes médias e poderia ser explicada pela umidade mais alta nas regiões tropicais.

Note-se que todos os resultados são disponíveis no artigo em curso de publicação no Atmospheric Measurement Techniques (AMT) e apresentados no anexo 1. Este artigo está na fase final de aceitação, já tendo passado pela discussão aberta e pelos revisores.

c) Resultados do SOS-CHUVA

A mesma metodologia de classificação dos hidrometeoros foi aplicada aos dados coletados pelo radar banda X na região de Campinas-São Paulo durante o projeto do SOS-CHUVA e a diferença entre as regiões estratiformes e convectivas. Assim foi demonstrado que de uma forma semelhante a Manaus, a região de precipitação estratiforme é composta de: chuva fraca, chuva, agua- neve, neve, e gelos; enquanto que a região de precipitação convectiva é formada de três tipos de chuva (fraca, moderado, forte), granizo, dois tipos de graupel (alta e baixa densidade), neve e gelos.

Numa segunda parte, uma atenção particular foi dedicada nas células convectivas mais severas que estão no centro das preocupações do projeto SOS-CHUVA. Por isso, a evolução microfísica de 23 células convectivas foi investigada na região de Campinas. De maneira geral, foi demonstrado que as células convectivas seguem um ciclo de vida normal com os volumes de: chuva forte, granizo, graupels, e neves que são relacionados às taxa de raios. Assim quando tem mais raios, tem mais desses 4 tipos de hidrometeoros e por conseguinte constituem os melhores indicadores para prevenir os riscos potenciais. Além disso, foi demonstrado que as altitudes associadas ao graupel e gelos (tipos de hidrometeoros os mais importantes sobre a eletrificação da nuvem) estão em conformidade com estudos anteriores realizadas no EUA e Japão. Assim, seguir a evolução das altitudes em relações com os graupel e gelos pode informar-nos sobre a intensidade da atividade eléctrica.

Todos os resultados são disponíveis no artigo em curso de publicação no Weather and Forecasting e apresentado no anexo 2.

d) Assimilação de dados de descargas eléctricas

Este estudo trata da Dissertação de Mestrado da aluna Carolina Araújo que analisou o uso dos dados do sensor de descargas eléctricas do GOES em modelos de alta resolução. A classificação de nuvem foi realizada para caracterizar os perfis de hidrometeoros em tempestades com potencial de

assimilação de diferentes espécies de partículas na redução do spin up do modelo para previsão no intervalo de 0 a 6 horas.

A análise de classificação hidrometeoros (HC) permitiu caracterizar a distribuição vertical de hidrometeoros para diferentes classes de densidade de descargas elétricas. Essas classes de descargas elétricas que definem os perfis a serem assimilados no modelo. Os resultados mostraram seis classes distintas de hidrometeoros com diferentes distribuições em função das classes de eletrificação. Nota-se que com o aumento da intensidade de eletrificação da nuvem a altura de maior concentração de partículas graupel e gelo são encontradas em partes distintas da nuvem. Na classe mais baixa de eletrificação, por exemplo, a concentração máxima graupel é de 7,5 km e a maior quantidade de gelo encontra-se a cerca de 9,5 km, e para de maior atividade elétrica as concentrações máximas de desses hidrometeoros são cerca de 8 km e 13 km respectivamente. Considerando que o cristal de gelo e graupel são as principais partículas no processo de eletrificação de nuvem, já que eles formam duas regiões opostas cobrado (gelo-negativo, graupel-positivo). Esta distância entre essas regiões impacta na força do campo elétrico, uma vez que a distância aumenta e intensifica a força do campo elétrico. Esse trabalho está sendo finalizado para ser submetida ao um Jornal da American Meteorological Society.

e) Comparação entre diferentes parametrizações de microfísica de nuvens.

Este trabalho é o que se apresenta em fase mais incipiente. Ele utiliza a classificação de nuvens para comparar simulações elaboradas com diferentes microfísicas das nuvens. A aluna Lianet Pardo está realizando o Doutorado no INPE e utilizando estes estudos. Os resultados estão sendo analisados, com base em um conjunto de classificações de hidrometeoro dos eventos como referência a análise da melhor parametrização de microfísica das nuvens.

Esses estudos, bem como futuros outros irão se beneficiar desta ferramenta de análise de imagens de radares, bem como o possível desenvolvimento de um produto de nowcasting.

2 – PARTICIPAÇÕES NAS CONFERENCIAS

Durante os dois anos de pós-doutorado, varias comunicações foram feitas no Brasil através de conferências nacionais ou internacionais. Assim, os resultados foram apresentados nos Workshops do projeto SOS-CHUVA em São Paulo (dezembro 2016) e em Piracicaba (dezembro 2017). Além disso, o bolsista participou da campanha de medições efetuada na região de Campinas durante a última semana de novembro 2017, em apoio das medições do radar da banda X.

Por último, os resultados foram apresentados na 38 Conferência do American Meteorology Society sobre os radares meteorológicos que se desenrolou no final de agosto 2017 em Chicago (IL, EUA; cf anexo 3).

3 – CO-ORIENTAÇÃO DE ALUNO DE MESTRADO

Durante os dois anos de pós-doutorado, o bolsista teve uma oportunidade de participar a um enquadramento de Mestrado. Assim, com o Dr. Luiz Augusto Toledo Machado, orientamos a aluna Carolina de Souza Araújo sobre o assunto descrito acima: “Relação entre raios e microfísica para potencial uso em assimilação de dados”, que foi defendido o 28 maio 2018 (cf. Anexo 4). Conforme mencionado, os resultados obtidos estão sendo preparados para uma publicação e foram aprovados para apresentação oral na próxima conferência da American Meteorology Society em Phoenix no início do ano 2019.

ANEXO 1:

Ribaud, J.-F., Machado, L. A. T., and Biscaro, T.: *X-band dual-polarization radar-based hydrometeor classification for Brazilian tropical precipitation systems*, Atmos. Meas. Tech. Discuss., <https://doi.org/10.5194/amt-2018-174>, in review, 2018.

ANEXO 2:

Ribaud, J-F and Machado L.A.T. *Insight into brazilian microphysical convective clouds observed during SOS-CHUVA*. Weather and Forecasting, to be submitted, 2019.

ANEXO 3:

J.-F. Ribaud, L.A.T. Machado, and T. Biscaro. *Dominant Hydrometeor Type Distributions within Brazilian Tropical Precipitation Systems Inferred from X-Band Dual Polarization Radar Measurements*. Poster, 38th Conference on Radar Meteorology, Chicago, IL, USA, 28 August-1 September 2017.

ANEXO 4:

Declaração de participação na banca examinadora final de aluna de Mestrado – Carolina de Souza Araújo, 28 de Maio de 2018, INPE/CPTEC, Cachoeira Paulista, SP, Brasil.

ANEXO 1:

Ribaud, J.-F., Machado, L. A. T., and Biscaro, T.: *X-band dual-polarization radar-based hydrometeor classification for Brazilian tropical precipitation systems*, *Atmos. Meas. Tech. Discuss.*, <https://doi.org/10.5194/amt-2018-174>, in review, 2018.

X-band dual-polarization radar-based hydrometeor classification for Brazilian tropical precipitation systems

5

Jean-François Ribaud¹, Luiz Augusto Toledo Machado¹, and Thiago Biscaro¹

10

¹National Institute of Space Research (INPE), Center for Weather Forecast and Climate Studies (CPTEC), Rodovia Presidente Dutra, km 40, Cachoeira Paulista, SP, 12 630-000, Brazil

Submitted to Atmospheric Measurement Techniques

15

GoAmazon2014/5 special Issue

May 2018

First Revised Version September 2018

Second Revised Version December 2018

20

Correspondence to: Jean-François Ribaud (jean-francois.ribaud@inpe.br)

Abstract.

25 The dominant hydrometeor types associated with Brazilian tropical precipitation systems are identified via research X-band dual-polarization radar deployed in the vicinity of the Manaus region (Amazonas) during both the GoAmazon2014/5 and ACRIDICON-CHUVA field experiments. The present study is based on an Agglomerative Hierarchical Clustering (AHC) approach that makes use of dual polarimetric radar observables (reflectivity at horizontal polarization Z_H , differential reflectivity Z_{DR} , 30 specific differential phase K_{DP} , and correlation coefficient ρ_{HV}) and temperature data inferred from sounding balloons. The sensitivity of the agglomerative clustering scheme for measuring the inter-cluster dissimilarities (linkage criterion) is evaluated through the wet season dataset. Both the weighted and Ward linkages exhibit better abilities to retrieve cloud microphysical species, whereas clustering outputs associated with the centroid linkage are poorly defined. The AHC method is then applied to 35 investigate the microphysical structure of both the wet and dry seasons. The stratiform regions are composed of five hydrometeor classes: drizzle, rain, wet snow, aggregates, and ice crystals, whereas convective echoes are generally associated with light rain, moderate rain, heavy rain, graupels, aggregates and ice crystals. The main discrepancy between the wet and dry seasons is the presence of both low- and high-density graupels within convective regions, whereas the rainy period exhibits only 40 one type of graupel. Finally, aggregate and ice crystal hydrometeors in the tropics are found to exhibit higher polarimetric values compared to those at mid-latitudes.

Keywords: hydrometeor identification, tropical microphysics, dual-polarization radar, clustering.

45 1. Introduction

The use of dual-polarization (DPOL) radars over several decades by national weather services as well as research laboratories has deeply changed the understanding and forecasting of many precipitation events around the world. By using a second orthogonal polarization, such weather radars enable inference of the size, shape, orientation, and phase state of different particles detected within the
50 sampled cloud. To date, the major advances that have been made as a result of DPOL radar sensitivities are mainly related to improvement in the distinction between meteorological and non-meteorological echoes, attenuation correction, quantitative rainfall estimation, and bulk hydrometeor classification (Bringi and Chandrasekar 2001; Bringi et al., 2007). By combining DPOL radar observables (generally, reflectivity at horizontal polarization, Z_H ; differential reflectivity, Z_{DR} ; specific differential phase, K_{DP} ;
55 and correlation coefficient, ρ_{HV}) with some extra information such as temperature to locate the freezing level, the hydrometeor identification task has been the subject of many research studies. Indeed, potential benefits from this research topic are numerous such as the evaluation of microphysical parametrization in high-resolution numerical weather prediction models (e.g., Augros et al., 2016; Wolfensberger and Berne, 2018), investigation of relationships between microphysics and lightning
60 (e.g., Ribaud et al. 2016a), and improvement in weather nowcasting for high-impact meteorological events (hailstorms, flight assistance, road safety).

Three hydrometeor classification schemes have been developed since the emergence of DPOL radar in the 1980s: (i) supervised, (ii) unsupervised, and (iii) semi-supervised techniques (Figure 1).

65 i. The supervised method constitutes, by far, most of the literature and is subdivided into three
different techniques: the boolean tree method, fuzzy logic and the Bayesian approach. Here, the
supervised technique refers to a priori and arbitrarily identified hydrometeor types from which
DPOL radar responses have been derived from either theoretical models or empirical
70 knowledge. Polarimetric observations are then assigned to the most suitable hydrometeor types
according to their similarities.

- Boolean method. This technique is the easiest way to identify dominant hydrometeor
populations and has consequently been the first to be used. The algorithm relies on the
beforehand definition of the ranges of DPOL radar-observable values for each hydrometeor
type by the user. Then, a simple Boolean decision is applied to retrieve the dominant
75 hydrometeor type (Seliga and Bringi, 1976; Hall et al, 1984; Bringi et al, 1986; Straka and
Zrnić, 1993; Höller et al, 1994). This approach, nevertheless, does not take into account the
fact that different hydrometeor types can be defined on the same range of values for the
same polarimetric radar observable and, therefore, frequently leads to misclassification.

- Fuzzy logic technique (Mendel et al., 1995). This supervised algorithm type fixed the
80 previous limitation by allowing a smooth transition of DPOL radar-observable ranges for all
hydrometeor types. The originality of fuzzy logic is its ability to transform sets of nonlinear
radar data into scalar outputs referring to different microphysical species. In this regard, each
hydrometeor type distribution is characterized by a membership function coming from either
T-matrix simulations (Mishchenko and Travis, 1998) or, less frequently, aircraft in situ
85 measurements. The hydrometeor inference is finally the result of a combination of

membership functions and a set of a priori rules defined by the user (Straka et al., 1996; Vivekanandan et al., 1999; Liu and Chandrasekar, 2000; Marzano et al, 2006; Park et al., 2009, Dolan and Rutledge, 2009; Al-Sakka et al., 2013; Thompson et al., 2014). This method is relatively simple to implement and computationally inexpensive. Few studies such as the Joint Polarization Experiment (Ryzhkov et al., 2005) for hail detection or even the recent use of a fuzzy logic algorithm as an operational tool for national weather services (Al-Sakka et al., 2013) have demonstrated the robustness of this hydrometeor classification algorithm type in singular environments.

- Bayesian approach. In this case, the hydrometeor identification task is expressed in a probabilistic form based on synthetic data derived from polarimetric radar simulation of different hydrometeor types (with each one being characterized by a centre and a covariance matrix). The final supervised hydrometeor inference is then performed by adapting the maximum a posteriori rule. Another interesting attribute of the Bayesian technique resides in the appealing possibility of retrieving the liquid water content associated with each hydrometeor type (Marzano et al., 2008; Marzano et al., 2010).

- ii. More recently, Grazioli et al. (2015) or even Grazioli et al. (2017) proposed an innovative unsupervised approach to identifying the dominant hydrometeor distribution within precipitation events, where hydrometeor types are retrieved by gathering DPOL radar data observable similarities. Indeed, the unsupervised technique refers to a set of unlabelled data observations in which the goal is to group them into clusters sharing similar properties based on innate structures of the data (variance, distribution, etc.) and without using a priori knowledge. To

achieve this goal, the authors used an agglomerative hierarchical clustering technique together with a spatial constraint on the consistency of the classification (homogeneity). This data-driven approach mainly avoids the numerical-scattering simulations used in fuzzy logic, which are well-designed for the liquid phase but questionable for ice-phase microphysics. Finally, interpretation of the clusters (labelling) is done manually.

- iii. Although initially mentioned by Liu and Chandrasekar (2000), the first complete study based on a semi-supervised approach was done by Bechini and Chandrasekar (2015), recently followed by the works of Wen et al. (2015), Wen et al. (2016) and Besic et al. (2016). This technique combines the advantages of the fuzzy logic and clustering methods. The algorithm initially begins with a fuzzy logic classification, which is then adjusted by a K-means clustering method that iteratively allows for rectifying the initial membership function of each hydrometeor type according to the observed DPOL radar measurements. In addition, constraints such as temperature limits and/or spatial distribution can be implemented in this self-adapting methodology.

Overall, these Hydrometeor Classification Algorithms (HCAs) still require in situ aircraft validations (especially within convective cores) that are problematic due to their cost and, obviously, the danger of obtaining such measurements. Only a few studies have had the opportunity to use limited aircraft measurements and generally compared a few isolated in situ images with HCA outputs (Aydin et al., 1986; El-Magd et al., 2000; Cazenave et al., 2016; Ribaud et al., 2016b). Another limitation of these studies using methods such as the fuzzy logic approach is the dependency of their validity, since

they are generally both wavelength- and climatically radar-dependent. Although T-matrix simulations for a radar wavelength have been theoretically demonstrated, each final algorithm is then tuned by giving weights to each DPOL radar observable to allow them to fit as closely as possible with local ground observations. Finally, one can also see that the related hydrometeor identification literature is mainly concerned with the middle latitudes. Indeed, the methods were initially developed for S-band radar before being adapted to both C- and X-band radars, and research studies have largely been done in North America, Europe, and Oceania.

135

The present study aims to develop the first HCA for Brazilian tropical precipitation systems via an X-band dual-polarization radar used in both the GoAmazon2014/5 and ACRIDICON-CHUVA field experiments (Martin et al., 2016; Wendisch et al., 2016; Martin et al., 2017; Machado et al., 2018). Although the area constitutes an intriguing location with both a high amount of rain and complex aerosol-cloud interaction (e.g., Cecchini et al., 2017; Machado et al., 2018), there are almost no references for hydrometeor classification over tropical land, especially for the Amazon region. In this regard, the studies by Dolan et al. (2013) and Cazenave et al. (2016) took place in singular locations (Darwin, Australia, and Niamey, Niger, respectively). Both of these studies used a supervised fuzzy logic approach to retrieve the hydrometeor distribution within precipitation events with a C- and adapted X-band scheme, respectively. As aforementioned, fuzzy logic algorithms use weights to constrain the final identification. Another issue that might be related to hydrometeor identification tasks is the use of the melting layer as a parameter to detect liquid-ice delineation. However, liquid water above the melting layer within the convective tower of tropical systems is not unusual (Cecchini et al.,

2017; Jakel et al., 2017). For instance, Cecchini et al. (2017) retrieved liquid water at as low as $-18\text{ }^{\circ}\text{C}$
150 within polluted tropical convective clouds. Classification using cluster analysis allows the use of natural
(non-imposed) classes of ice-water species. For all these reasons, the present paper deals with the first
unsupervised clustering method based on X-band DPOL radar measurements in the Brazilian tropical
region. Three main questions are addressed in this paper: (1) What is the sensitivity of the clustering
algorithm to the different linkage methods, and how can one improve the liquid-solid delineation? (2)
155 What are the hydrometeor classification output characteristics for both wet and dry tropical seasons in
Amazonas? And (3) what are the microphysical distribution differences within tropical convective and
stratiform cloud systems between the wet and dry seasons?

The article is organized as follows: section 2 provides a brief description of the radar dataset,
while section 3 presents the AHC method. The sensitivity of the AHC to the linkage methods together
160 with a potential temperature improvement is assessed and discussed in section 4. The hydrometeor
identification for Brazilian tropical system events is presented in terms of wet-dry seasons and
stratiform-convective regions in section 5, while a discussion of hydrometeor distribution comparisons
is presented in section 6.

165 **2. Datasets and processing**

The data used in this study are mainly based on DPOL radar data observations collected during
both the GoAmazon2014/5 and ACRIDICON-CHUVA experiments that took place around the city of
Manaus in the Amazonas state of Brazil (Figure 2). Both of these research experiments aimed to
investigate the complex mechanisms at play within tropical weather through intriguing interactions

170 between human activities and the neighbouring tropical forested region. In this regard, the present study considers the wet and dry seasons as corresponding to the intensive operating periods (IOPs) of the GoAmazon2014/5 field experiment (Martins et al., 2016), which were from 1 Feb – 31 Mar 2014 (wet season: 59 days) and 15 Aug – 12 Oct 2014 (dry season: 60 days).

Among all the instruments deployed, a Selex-Gematronik X-band DPOL radar was located in the
175 city of Manacapuru in 2014 to complete the radar coverage from the Manaus Doppler radar, as well as to provide more microphysical details about the South American monsoon meteorological systems (Oliveira et al., 2016). The X-band DPOL radar was operated at 9.345 GHz with a 1.3° beam width at -3 dB and in simultaneous transmission and reception (STAR) mode (Schneebeli et al., 2012; and Table 1). The latter characteristic allows the reflectivity at horizontal polarization Z_H , differential reflectivity
180 Z_{DR} , differential phase Φ_{DP} , and correlation coefficient ρ_{HV} to be obtained. The scanning strategy was designed to complete an entire volume scan in 10 minutes by combining 15 different plan position indicators (PPIs) ranging from 0.5° to 30° , as well as two range height indicators (RHIs) towards randomly different directions.

The raw radar dataset has been processed beforehand to be used for the hydrometeor identification
185 task. In this regard, a four-step process has been applied to the DPOL radar dataset which consists of i) calibration of Z_{DR} , ii) identification of meteorological and non-meteorological echoes, iii) Φ_{DP} filtering and estimation of the derivative specific differential phase K_{DP} (Hubbert and Bringi, 1995), and iv) attenuation correction applied to both Z_H and Z_{DR} based on the ZPHI method proposed by Testud et al. (2000). The calibration of Z_{DR} has been adjusted by using vertically pointing scans for cases with no rain
190 attenuation (drizzle/light rain). This method allows to temporally calculate the Z_{DR} offset since 0 dB is

expected. The offset has been then removed in subsequent Z_{DR} measurements. A second analysis of Z_{DR} was occasionally realized by checking Z_{DR} values within stratiform light rain medium and characterized by Z_H values between 20 and 22 dBZ. The expected Z_{DR} value was 0.2 dB as showed by Illingworth and Blackman 2002 or Segond et al. 2007. Note that the dataset has also been restricted to precipitation
195 events wherein the radome of the X-band DPOL radar was dry in order to remove any additional attenuation (Bechini et al, 2010). In addition to these considerations, a signal-to-noise ratio of $SNR \geq +10$ dB, as well as a reduced radar coverage ranging from 5 to 60 km have been considered for this study to mitigate potential remaining errors. The last processing step relies on the separation of stratiform and convective radar echoes. The methodology used in the present paper is the same as that
200 used by Steiner et al. (1995) and has been applied from a horizontal reflectivity field at a constant altitude plan position indicator (CAPPI) generated at 3 km height ($T > 0$ °C).

The present study also deals with external temperature information coming from soundings launched near the X-band radar (downwind of Manaus) at 00, 06, 12, 15, and 18 UTC, respectively. The sounding with the closest time to the radar measurements has been considered to derive the temperature
205 profile associated with both PPIs and RHIs.

3. Unsupervised Agglomerative Hierarchical Clustering

The present hydrometeor classification algorithm is an unsupervised AHC method that aims to partition a set of n observations into N different clusters. This technique works as an iterative “bottom-
210 up” method where each observation starts in its own cluster and pairs of clusters are aggregated step by step until there is one final cluster, which comprises the entire dataset. Each cluster is composed of a

group of observations sharing more similar characteristics than the observations belonging to the other clusters. Here, there is no a priori information concerning the shape and size of each cluster or the final optimized number of clusters. A posteriori analysis is then performed through the final iterations to
215 retrieve the optimal clustering partition and respective labels.

Since associated background already exists, the reader is especially referred to Ward (1963) and Jain et al. (2000) for detailed mathematical reviews of the technique. Additionally, the present clustering framework is mainly based on the methodology developed by Grazioli et al. (2015 – section 4 and Figure 2), hereafter referred to as GR15, and only relevant and important information will be
220 addressed hereafter to avoid being redundant. The main steps of the present AHC can be summarized as follows:

- Vectorized objects of radar observations are defined for each valid radar resolution volume as

$$x = \{Z_H, Z_{DR}, KDP, \rho_{HV}, \Delta Z\},$$

- where ΔZ is the difference between the radar resolution height and the altitude of the isotherm at
225 0 °C, deduced from sounding balloons.
- Since scales of radar polarimetric variables differ by orders of magnitude, data normalization is applied to concatenate all the observations into a [0;1] common space. The first four components of each object are based on the minimum-maximum boundaries rule. The temperature information is redistributed by applying a soft sigmoid transformation that allows setting a value
230 of zero (one) for altitudes below (over) the bright band. Here, the thickness of the bright band over the whole GoAmazon2014/5 – ACRIDICON-CHUVA database has been manually estimated and set up to spread over a layer of ± 700 m. To obtain the maximum degrees of

freedom in the initial dataset coming from the DPOL radar measurements, here, the influence of the temperature information is mitigated by distributing its values into a $[0;0.5]$ range space.

- 235
- Although the radar data are now suitable for clustering, the choice of two criteria still remains. At each iteration of the AHC method, similarities/dissimilarities must be evaluated to determine which clusters merge. In this regard, the Euclidean metric is considered to calculate the distance between different single objects. The generalization of this distance metric to an ensemble of objects is called the merging linkage rule. Various methods exist to evaluate inter-dissimilarities
- 240
- such as single (nearest neighbour), complete (farthest neighbour), averaged, weighted, centroid, or even Ward (variance minimization) linkages (see Müllner, 2011). Herein, we consider the weighted, centroid and Ward linkage rules (see section 4.a).
- Running such a clustering method over the whole dataset is computationally very expensive. To tackle this problem, a subset of approximately 25 000 initial observations is randomly chosen
- 245
- through the whole precipitation events database. The clustering method is initially applied to the subset and then extended to the whole dataset by using the nearest cluster rule at each iteration.
- One of the major novelties proposed by GR15 relies on the implementation of a spatial constraint that aims to check the homogeneity of the clustering distribution at each iteration. More precisely, one assumes that a smooth, horizontal transition exists between the resulting
- 250
- hydrometeor field outputs. Therefore, a spatial smoothness index is calculated at the end of each iteration step and individual object by checking the four closest geographical radar gates. In the very same way as that used in GR15, results are summarized into a confusion matrix, from

which several spatial indexes can be extracted to analyse the individual and global spatial smoothness of a partition.

- 255 • The merging of two clusters is realized by identifying the cluster which presents the lowest spatial similarities among all clusters. Objects belonging to this spatially poor cluster are then constrained to be redistributed through the other existing clusters according to the linkage method chosen. This final step allows decreasing the total number of clusters by one.
- 260 • If the iteration process does not reach a single and unique cluster, the iteration loop then restarts at the initial PPIs classification and goes through the evaluation of spatial homogeneity.
- Finally, an analysis of the variance explained has been implemented to evaluate the consistency of the clustering classification outputs. This quality metric allows definition of the theoretically appropriate number of clusters by analysing the ratio between the internal and external variance of each cluster at each step of the iteration. The main idea here is to find the optimal cluster
265 distribution beyond which considering one more cluster is not meaningful.

4. Methodology discussions

a) Linkage rule sensitivity

According to the setup described in section 3, different linkage rules have been tested through the
270 special wet season observation period (February to March) of 2014. To perform this sensitivity test, three different linkage rules have been considered here: (i) weighted, (ii) centroid, and (iii) Ward (see Table 2 for their respective formulas). Since the clustering method randomly picks observations within the whole wet season period, a set of numerous runs for each linkage method have been performed to

extract, as much as possible, the most representative behaviour of each one. The general common setup
275 is composed of a subset of 25 000 observations randomly picked through more than 50 precipitation
days. The temperature information is based on radiosounding observations and is dispatched in a [0;0.5]
interval to place twice as much importance on the initial DPOL radar observations. The number of
clusters reached in the first step of the AHC method is set at 50 (far enough from the final partition and
not too computationally expensive). Finally, the clustering method has been conducted separately on
280 stratiform and convective regions.

In this respect, Figure 3 presents the evolution of the variance explained (the ratio between the
internal and external variance) for the three different linkage rules as a function of the number of
clusters considered, together with their associated precipitation regimes (stratiform or convective).
285 Overall, the three methods exhibit an “elbow” curvature with an optimal number of clusters ranging
from approximately 5 to 8 (orange background on Figure 3). One can see that from 2 to 5 clusters, the
variances explained sharply increases, meaning that each added cluster within this interval contributes
significantly to retrieving the most adequate cluster partition. From 5 to 8 clusters, the increase starts to
slow down, indicating that considering a greater number of clusters is not meaningful. In this regard, the
290 best “compromise” seems to be the weighted and/or Ward linkage method for both stratiform and
convective regions. Indeed, these methods have the highest scores, with approximately 99 % reached
within the 5-8 clusters interval.

Due to the inherent complexity of representing all the potential combinations, manual analysis and
295 selection have been performed beforehand to find the optimal number of clusters between the stratiform
and convective regions. The results from this partitioning are presented through one stratiform and one
convective RHI (Figures 4 and 5).

In addition, fuzzy logic information has been implemented to make comparisons with cluster outputs.
300 The fuzzy logic scheme is mainly based on the X-band algorithm of Dolan and Rutledge (2009),
hereafter referred to as DR09, and has been slightly enriched for the wet snow and melting hail
hydrometeor types by Besic et al (2016) through scattering simulations and a temperature membership
function (Besic et al, 2016 – Appendix A). Finally, the adapted fuzzy logic allows discrimination
between nine hydrometeor types: light rain (LR), rain (RN), melting hail (MH), wet snow (WS),
305 aggregates (AG), low-density graupel (LDG), high-density graupel (HDG), vertically aligned ice (VI),
and ice crystals (IC).

Figure 4 shows a stratiform system exhibiting a well-defined bright band signature from polarimetric
observations that occurred on the shores of the Amazon River on 21 February 2014. Overall, the
310 centroid linkage method does not reproduce the event well, and the final representation is
microphysically poor (Figure 4-f). Indeed, this linkage rule simply divides the cloud into three
homogeneous regions ($T > 0$ °C, $T \sim 0$ °C, and $T < 0$ °C). Additionally, the centroid linkage fails to
identify a clear bright band region (Figure 4f, clusters 2S and 3S). On the other hand, the weighted and
Ward linkage methods are very close to the fuzzy logic output descriptions (Figure 4e-g-h). They both

315 exhibit two kinds of rain, and a bright band region sits below of what appears to be an aggregates-ice crystals mixture. The main discrepancy here concerns the representation of the rain structure. The Ward linkage rule retrieves two more distinct liquid species (as does fuzzy logic), whereas the weighted linkage method exhibits a smoother rainy region.

320 Figure 5 presents a decaying convective cell that occurred on 02 February 2014 at 13:57 UTC (0-7 km from the radar: stratiform region, 7-40 km from the radar: convective region). As is the case for the stratiform RHI in Figure 4, the centroid linkage rule fails to retrieve a detailed microphysical structure and only presents very homogeneous liquid and solid regions. Once again, both the weighted and the Ward linkage rule stand out and display a more realistic hydrometeor description of the convective
325 cloud in comparison to the DPOL radar observations and the fuzzy logic outputs (Figure 5 a-b-c-d-e-g-h). Although they both present three clusters for $T > 0$ °C, the weighted linkage rule puts more emphasis on the convective region located ~ 20 -30 km from the radar than does the Ward linkage (Figure 5-e, cluster 6C vs. Figure 5-g, cluster 11C). The representation of the solid region ($T < 0$ °C) is almost the same, except for in the aggregates region (Figure 5h), which seems to be smaller for the weighted
330 linkage rule (Figure 5e cluster 8C) than for the Ward method (Figure 5g cluster 10C). Another discrepancy between the weighted and Ward linkages concerns the layer around the isotherm at 0 °C. Although Figure 5 does not exhibit any bright band region, the Ward linkage rule does exhibit one due to the temperature input (Figure 5g cluster 12C), whereas the weighted rule does not. The bright band region is known to be well-defined for stratiform regimes but quasi-undetectable (if detectable at all) for
335 convective areas (Leary and Houze, 1978; Smyth and Illingworth, 1998; Matrosov et al., 2007).

Throughout the present paper, one will thus consider only a bright band cluster for the stratiform regions, whereas convective areas will be lacking one.

Overall, Figures 3, 4, and 5 have shown that the centroid linkage method is inappropriate for the present
340 task, whereas both weighted and Ward linkage rules are able to retrieve a detailed microphysical structure within the sample cloud. Based on the present description and our personal analysis over the whole dataset, we chose to keep working with the weighted linkage rule throughout the remainder of the paper.

345 **b) Potential improvement around isotherm 0 °C**

High amounts of liquid water a few kilometres above the isotherm at 0 °C are not rare within the core of convective tropical cells. Sometimes, super-cooled liquid drops can be maintained and even moved upward within the melting layer, thus occasionally giving distinctive column-shaped polarimetric signatures for Z_{DR}/K_{DP} (e.g., Kumjian and Ryzhkov, 2008). A simple liquid-solid delineation based only
350 on the temperature profile is therefore unsuitable.

Figure 6 presents an adaptive solution to tackle this issue based on the clustering outputs of the weighted linkage rule. The solution proposed here relies on a posteriori analysis of the clustering outputs associated with the convective regions. First, one proceeds to identify the convective core under the isotherm at 0°C (here, cluster 6C). Then, all radar observations within the solid region are assigned
355 by calculating their distance from the 6C cluster centroid without applying any temperature constraint (objects are thus defined only by the first four radar components). If the distance is smaller than $D < 0.25$

and there is no discontinuity throughout the liquid-solid delineation, then the solid identification is switched to liquid (cluster 6C). Note that the distance D has been empirically chosen for the present radar observations and could consequently be adjusted by exploring more convective days. Overall, with this simple hypothesis, one can see the potential of a such method (Figure 6b). The liquid cluster can thus reach 8 km in the core of the convection at 25 km from the radar, which matches well with the convective tower (>35 dBZ) visible in Figure 5a. Around this convective core, the enhancement allows raising raindrops by about one kilometre upward in the 0°C isotherm, restraining cluster 6C at ~ 5 km. In comparison to a simple binary delineation such as that used for the fuzzy logic outputs (Figure 6a), the focus on radar observables in a second phase is then promising.

5. Wet and dry season dominant hydrometeor classifications

This section aims to interpret and label each cluster retrieved through both the wet and dry seasons over the Manaus region by using the AHC method setup described in section 3. As the use of classification allowing liquid water above the melting layer of convective towers needs further validation, a standard classification is used to classify and analyse the wet and dry hydrometeors using the temperature parameter.

a) Wet season clustering outputs

The distributions of Z_H , Z_{DR} , K_{DP} , ρ_{HV} , and ΔZ for each cluster from the stratiform and convective clouds of the wet season together with their probability densities are presented in the violin plot in

Figure 7 and Figure 8, respectively. The contingency table between the stratiform (convective) clustering outputs and the nine microphysical species retrieved by the DR09 adapted fuzzy logic algorithm is shown in Table 3 (Table 4). The complete wet season cluster centroids are given in Appendix A.1.

1) Stratiform region

Cluster 1S is only defined for negative temperatures and is associated with high ρ_{HV} and low Z_H , Z_{DR} and K_{DP} values (Figures 4e and 7). One can see from contingency Table 3 that the cluster 1S repartition is mostly associated with aggregates ($\sim 33\%$) and ice crystals ($\sim 12\%$) for high altitudes. Although the horizontal and differential reflectivity values are slightly higher than those for the DR09 T-matrix microphysical outputs and polarimetric characteristics retrieved by GR15, one can make the assumption that the cluster 1S behaviour stands for ice crystals. On the other hand, cluster 2S is closer to the DR09 T-matrix aggregates microphysical features. This cluster is characterized by a mean horizontal (differential) reflectivity of ~ 27 dBZ (~ 1.3 dB), a low specific differential phase (~ 0.27 degree/km) and a high coefficient of correlation (0.97). Overall, the polarimetric signatures of cluster 2S are mostly divided into the associated wet and dry snow (aggregates) from the microphysical categories of fuzzy logic (Table 3). Figure 4e allows discrimination between these categories, and one can consider that cluster 2S is here associated with aggregates. Once again, its polarimetric signatures are slightly higher than the DR09 T-matrix values or even the GR15 aggregates clustering output. One explication behind these distributions being slightly shifted to higher values can be the relative humidity, which is

higher in the tropics than at higher latitudes. The growth of ice crystals/aggregates by vapor diffusion
400 within this cloud region (Houze, 1997) may lead to bigger solid particles (higher Z_H and Z_{DR} values).

The bright band region is well-represented here by cluster 4S. Indeed, its global distribution spreads only at the altitude of the isotherm at 0 °C and exhibits high Z_H and Z_{DR} values, as well as low K_{DP} and ρ_{HV} values. Finally, clusters 3S and 5S present rain characteristics since more than 90 % of these clusters are in agreement with the drizzle and rain fuzzy logic types from DR09. Although the two
405 clusters have the same behaviours, cluster 3S is characterized by polarimetric signatures higher than those in cluster 5S, except for the coefficient of correlation (0.97 vs. 0.99, respectively). In this regard, one can consider that cluster 3S represents the rain microphysical species, whereas cluster 5S is related to drizzle characteristics.

410 **2) Convective region**

Overall, one can see from Figures 5 and 8 that the convective regions of the wet season are composed of three types of hydrometeors for both positive (clusters 6C-10C-11C) and negative temperatures (clusters 7C, 8C and 9C).

Hail precipitation in the Amazonas region is rare, and as expected, no clusters represent melting hail
415 characteristics, as in Ryzhkov et al. (2013) or Besic et al. (2016) (Table 4). Therefore, clusters 6C, 10C, and 11C can be associated with three distinct rainfall precipitation regimes. In this regard, cluster 10C presents the same light rain characteristics as both DR09 and GR15. The cluster is characterized by Z_H (Z_{DR}) values approximately 13 dBZ (0.68 dB), and a K_{DP} (0.14 degree/km) that is in high agreement

with the drizzle hydrometeor type from the adapted fuzzy logic ($\sim 97\%$, Table 4). According to this
420 description, one can attribute cluster 11C to the light rain precipitation type. The two remaining liquid
clusters are associated with moderate and heavy rainfall types with almost the same polarimetric
signatures as those given in GR15. Indeed, cluster 6C presents higher Z_H (44 vs. 31 dBZ), Z_{DR} (2.1 vs
1.4 dB), and K_{DP} (1.9 vs 0.8 degree/km) mean values than those for cluster 11C. In this regard, one can
link cluster 6C to heavy rainfall and cluster 11C to moderate rainfall.

425 Concerning negative temperatures, cluster 9C stands out by being spread at the highest altitudes (Figure
8-e). This cluster is defined by low Z_H , Z_{DR} , and K_{DP} values together with a moderate ρ_{HV} (~ 0.97). One
can note that cluster 9C is close to the ice crystals/small aggregates retrieved by GR15 and is also the
only cluster related to the T-matrix ice crystals species from DR09 (Table 4). Within the decaying
convective cell presented in Figure 5, one can observe that cluster 7C is associated with the low-density
430 graupel characteristics proposed by DR09 and exhibits Z_H (Z_{DR}) values approximately 36 dBZ (0.8 dB).
In addition, cluster 7C is mainly classified ($\sim 69\%$) as low-density graupel (Table 4). Finally, the last
cluster, 8C, is surrounded by ice crystals and presents polarimetric signatures lower than those for
cluster 7C. Although it is defined by higher values than those given by DR09 and GR15, one can
associate cluster 8C with the aggregate microphysical species. Indeed, contingency Table 4 shows that
435 45 % of the cluster 8C points are in agreement with this hydrometeor type.

440 **b) Dry season clustering outputs**

As for the previous section, the clustering outputs retrieved by the AHC method and the weighted linkage rule are identified and associated with their corresponding microphysical species through the dry tropical season. The corresponding cluster centroids are detailed in Appendix A.2.

445 **1) Stratiform region**

Figure 9 shows the clustering classification outputs extracted from an RHI presenting a melting layer region within a stratiform event that occurred on 08 September 2014 in the region of Manaus. Overall, the clustering outputs are close to the hydrometeor distribution retrieved by the adapted DR09 fuzzy logic. Clusters 1S-2S retrieved for positive temperatures appear well located in terms of polarimetric signatures and fuzzy logic outputs. One can see that the melting layer region is clearly characterized by cluster 4S, whereas for negative temperatures, clusters 3S-5S show patterns close to the fuzzy logic outputs.

The violin plots in Figure 10 and contingency Table 5 allow discrimination and labelling of these clusters. For DR09 classification, clusters 1S and 2S exhibit rainfall signatures. Cluster 2S is in agreement with the fuzzy logic drizzle category (~ 92 %), whereas cluster 1S is divided into the drizzle (~ 76 %) and rain (~ 22 %) microphysical species. Between these two clusters, one can observe that cluster 1S contains the highest Z_H , Z_{DR} and K_{DP} values, and one can consequently label it as a rainfall type. Cluster 2S is, however, associated with the drizzle/light rain category according to the polarimetric radar signatures (GR15).

460 The liquid-solid delineation is represented here by cluster 4S. It presents a low ρ_{HV} (~ 0.93) and a large Z_H distribution around ~ 30 dBZ and is almost only defined for altitudes close to the 0°C isotherm. In addition, contingency Table 5 matches well with this hydrometeor association.

For the negative temperatures, the clustering outputs exhibit two clusters, 3S-5S. The first is located within the edge region of the cloud, whereas cluster 5S is distributed at lower altitudes and is closer to
465 particles of greater densities (Figure 10). Cluster 5S is in $\sim 70\%$ agreement with the aggregate fuzzy logic outputs (Table 5), and its polarimetric signatures are close to those of GR15 and T-matrix simulations from DR09. One can then define cluster 5S as the aggregate microphysical species. Finally, ice crystals/small aggregates are represented through cluster 3S, which is defined by low Z_H , Z_{DR} , and K_{DP} values and a high ρ_{HV} .

470

2) Convective region

Figure 11 shows an RHI of a convective system that occurred in the late afternoon on 06 October 2014 in the region of Manaus. Overall, this RHI shows a convective cell (at 24-50 km from the radar) together with its relative stratiform region (0-23 km). Note that the abrupt transition from the convective
475 and stratiform classification areas (Figure 5-6-11) is inherent to the Steiner et al. (1995) algorithm. In terms of microphysical distribution, there should be some consistency between the two cloud types. The implementation of continuity analysis may prevent the latter artefacts. The convective cell is characterized by Z_H values up to 25 dBZ at 14 km, and the cloud top exceeds 16 km. According to the fuzzy logic outputs (Figure 11-f), the cell exhibits mostly rainfall precipitation for positive
480 temperatures. The corresponding cluster outputs retrieve the same signatures, dividing the rain pattern

into three different clusters: 6C, 7C, and 12C. Once again, the fuzzy logic collocates a bright band around the isotherm at 0°C, whereas neither polarimetric signatures nor clustering outputs exhibit a bright band. For negative temperatures, the AHC method retrieves four clusters (8C, 9C, 10C and 11C), the same as the fuzzy logic outputs.

485

The violin plots in Figure 12 and contingency Table 6 allow discrimination and labelling of these clusters. For the convective regions observed during the wet season, hail precipitation is rare in the Amazonas. Contingency Table 6 is also in agreement with this description, since none of the clustering outputs exceed 3 %. Therefore, one can attribute clusters 6C, 7C, and 12C to three different rainfall
490 precipitation regimes, ranking the cluster positions as follows: 12C presents weaker Z_H , Z_{DR} , and K_{DP} values than does cluster 7C, which presents lower values than does cluster 6C (Figure 12). In addition, one can see from contingency Table 6 that all three are in very high agreement with the drizzle and rain microphysical species. Based on the aforementioned description together with Figure 11 analysis, one can attribute cluster 12C to light rainfall, cluster 7C to moderate rainfall and, finally, cluster 6C to the
495 heavy rainfall type.

Concerning all clusters spreading at negative temperatures, cluster 11C matches well with the high-density graupel category defined by DR09 such as “graupel growing in regions of large supercooled water contents, melting graupel, and freezing of supercooled rain”. Based on contingency Table 6, this cluster is mainly associated with wet snow and slightly with the low-density graupel microphysical
500 specie. Nevertheless, one can see that the ρ_{HV} distribution is pretty low (~ 0.94) and could also be the signature of wet graupel (due to melting or wet growth) or a mixture of graupel and hail, as suggested

by Straka et al (2000) and Kumjian et al (2008). This cloud region is surrounded by low-density graupel, characterized by cluster 9C (Figures 11-12). This hydrometeor type shows 60 % agreement with this microphysical type within contingency Table 6 and is close to the DR09 T-matrix outputs. Cluster 10C shares more than 50 % with the aggregates type and 30 % with the low-density graupel type, whereas cluster 8C is associated in general with ice crystals and aggregates types (Table 6). With Figures 11-12 and the aforementioned description, one can analyse cluster 9C as low-density graupel, cluster 10C as aggregates, and, finally, cluster 8C as ice crystals.

510 **6) Discussion**

a) Impact of the clustering method and location

The present results allow making a brief comparison between the classical supervised fuzzy logic technique commonly used in the literature and the unsupervised AHC method. In opposition to the rigid structure of a fuzzy logic algorithm, the flexibility of the clustering approach allows better identification of the bright band region. Indeed, the liquid-solid delineation around the 0 °C isotherm is better captured and distinguished by the AHC method, which preferentially follows the polarimetric signatures instead of the stratified temperature region. Additionally, one can see the ability of the AHC method to fully exploit the high sensitivity of the X-band radar frequency to distinguish between three different (light, moderate, and heavy) rainfall regimes such as in GR15. This enhancement allows, for instance, putting more emphasis onto severe convective precipitation cells and may open new perspectives for nowcasting issues.

Note that the present clustering method has been distinctly subdivided into stratiform and convective regions. Although they are characterized by different thermodynamic structures (Houze, 1997), the stratiform and convective regions may be related in terms of microphysical distributions, such as ice
525 particles which might be ejected from the top of an active convective cell into the upper part of the stratiform region. This microphysical continuity could be further considered either by merging stratiform and convective hydrometeor types that present close DPOL characteristics (Figures 7-8-10-12), or by implementing an a posteriori continuity analysis.

The location of the present study also offers the possibility to discuss mid-latitude and tropical
530 microphysical differences. As described in section 5, the dominant tropical hydrometeor classification overlaps some mid-latitude microphysical species definitions. For instance, one can see that both the aggregate and ice crystal microphysical species are skewed to higher horizontal (differential) reflectivity, regardless of the season and region (stratiform/convective) considered. These discrepancies might be attributed either to an inaccurate attenuation correction or inherent tropical characteristics involved
535 within microphysical ice growth. Although we considered a limited radar coverage, regions with high SNR values, as well as only precipitation events having a dry radome, the ZPHI method may still lead to overcorrection, especially on Z_{DR} in strong convective cases when the Mie-scattering may dominate the precipitation regions. Another explanation of these discrepancies may rely on tropical atmospheric characteristics that present higher tropospheric humidity profiles together with higher incident solar
540 radiation, playing an important role in comparison to mid-latitudes.

b) Wet-Dry season differences

The investigation of some Amazonian wet-dry season differences has already been explored by a few
545 studies. For instance, Machado et al. (2018) noted that during both the GoAmazon2014/5 and
ACRIDICON-CHUVA field campaigns, the wet season overall mean cumulative rain was four times as
much as that during the dry season. However, though characterized by a low amount of total rainfall,
the dry season presents the higher rainfall rate (Dolan et al, 2013; Machado et al, 2018). According to
Machado et al (2018), these discrepancies can partly be explained by the fact that the dry season
550 presents higher convective available potential energy (CAPE) and lower cloud cover than those during
the wet season. Another study conducted by Giangrande et al (2017) also examined the wet-dry season
differences through convective clouds. The authors showed that warm clouds exhibit larger cloud
droplets and that the stratiform region during the wet season is much more developed than that during
the dry season (due to surrounding monsoon ambient characteristics).

555 All these differences are expected to contribute to the wet-dry season differences. Here, one can address
for the first time these discrepancies through the dominant microphysical patterns in terms of
stratiform/convection precipitation regimes associated with the Central Amazonas (Manaus region).
Based on this new hydrometeor classification adapted to the tropical region, this section explores the
differences among the clouds related to these two seasons.

560

1) Stratiform region

Figure 13 presents a comparison of pairs of stratiform hydrometeor types between the wet and dry
seasons. For positive temperatures, both the drizzle and rain microphysical species present higher Z_H

and lower Z_{DR} values during the dry season than during the wet season. These polarimetric signatures
565 might be attributed to the evaporation and collisional processes that tend to reduce the particle diameters
(Kumjian and Ryzhkov 2010; Penide et al, 2013). The separation between the drizzle/light rain and the
rain microphysical species is defined for a rainfall rate of approximately 2.5 mm/h (American
Meteorological Society, 2018). The classical Marshall-Palmer Z-R relationship allows estimation of the
rainfall rate for stratiform precipitation. In this regard, the wet rain microphysical species is
570 characterized, on average, by a rainfall rate of 1.84 mm/h, whereas the rate is up to 3 mm/h during the
dry season. The general wet rain microphysical species distribution thus still contains drizzle/light rain
observations, which might be due to the different cloud cover patterns associated with stratiform echoes
during the two seasons. As noted by Machado et al (2018), stratiform cloud cover related to the rainy
season is more associated with a monsoon cloud regime than during the remaining season. While the
575 dry season stratiform regime is directly the result of the rain convective cells, the wet stratiform cover
may also refer to large ambient unrelated residual precipitation far outside the original convective cloud.
Overall, the melting layer, which is represented here through the wet snow microphysical species, is
consistent with the results of previous studies (Durdin et al, 1997; Giangrande et al, 2008; Heymsfield
et al, 2015; Wolfensberger et al, 2015; Wang et al, 2018). The vertically restricted layer of wet snow
580 presents the most widespread distribution of Z_H , Z_{DR} , K_{DP} and ρ_{HV} of all the retrieved microphysical
species and for both seasons. One can see that the wet season distribution differs from the dry season, as
its distribution is more associated with lower (higher) Z_H (Z_{DR}) values. The main discrepancy here is
related to the Z_{DR} distribution, which has stronger values during the wet season by approximately 1 dB.
According to the study of Wang et al. (2018) which put emphasis onto mature Mesoscale Convective

585 System events during the GoAmazon2014/5 experiment, the wet season always presents stronger bright band signatures that might be attributed to more prominent aggregation processes. Indeed, the moist conditions in midlevels could promote more ice growth in the stratiform regions (as compared to the dry season) and could lead to stronger bright band signatures when those aggregates melt.

One of the main differences in the cloud structure between the wet and dry season relies on the cloud
590 top altitudes. Indeed, during the dry season, clouds can easily reach 16-17 km in the tropics compared to only 13-14 km during the wet season. Therefore, the microphysical processes for negative temperatures are distributed over two different thickness layers and moisture profiles. In this cloud region, ice crystals grow by vapor diffusion until to have a sufficient weight to start falling and forming aggregates (Houze, 1997). Although they present quite similar distributions, they both spread at about a 1.5 km
595 interval difference in altitude. Additionally, the Z_{DR} values associated with aggregates and ice crystals are generally slightly higher than those retrieved in DR09 or GR15. However, this result is consistent with the study of Wendisch et al (2016) that identified shaped plates of aggregates/crystals in the anvil outflow with in situ airplane observations.

600 **2) Convective region**

Figure 14 presents a comparison of pairs of convective microphysical species between the wet and dry seasons. As aforementioned in section 5, the dry season is composed of 7 hydrometeor types compared to 6 for the wet season. While the rainy season only has a graupel microphysical species, the dry season allows distinguishing between low- and high-density graupel. Therefore, the graupel microphysical

605 species defined during the wet season has been associated with the low-density graupel of the dry season to make this comparison possible.

Convective regions are characterized by three different rainfall regimes: light, moderate and heavy rain. Overall, the Z_H , Z_{DR} , and K_{DP} distributions associated with the dry season are generally shifted towards higher values. The dry season is known to exhibit the most intense convective cells (Machado et al, 610 2018). Their corresponding precipitation formation mechanism is generally dominated by ice microphysical processes, wherein the melting of graupel particles lead to large raindrops (Rosenfeld and Ulbrich, 2003; Dolan et al., 2013). One can see here that although growth by coalescence could be very efficient during the wet season, the production of larger raindrops results mostly from ice microphysical processes.

615 Overall, the combination of the wet season graupel microphysical species with the dry season low-density graupel makes sense in Figure 14. Indeed, they have almost the same polarimetric range distributions and are in agreement with each other. By contrast, the high-density graupel signatures are correlated with high Z_H , Z_{DR} , and K_{DP} values and low ρ_{HV} values. As mentioned in section 5.b.2, high-density graupel would have been associated with a mixture of wet graupel/small hail. Nevertheless, 620 these three related graupel categories are even consistent with the DR09 T-matrix definitions.

The main discrepancy between the aggregate and ice crystal microphysical species concerns their altitude definitions, wherein the dry season allows generating these hydrometeor types at higher altitudes. Systematically, the aggregate and ice crystal Z_H and Z_{DR} distributions are shifted to higher values during the wet season. These shifts may be due to an unreliable estimation of the attenuation 625 correction or explained by the results of Rosenfeld et al (1998) and Giangrande et al (2016). Both of

these studies showed that during the dry season, updrafts are more intense and, therefore, do not allow enough time for small ice crystals to properly develop. In terms of aerosol concentrations, the wet Amazonian season is known to be much cleaner than the dry season (Artaxo et al. 2002). With this regard, Williams et al (2002), Cecchini et al (2016), or even Braga et al (2017) highlighted its impact on
630 the microphysical development of tropical cloud particles, showing that high aerosol concentrations may lead to smaller liquid particles within strong updraft regions. Well, small drops are known to freeze at colder temperatures by inhibiting the ice multiplication processes (Hallet and Mossop, 1974), and may account for the wet/dry season differences observed.

635

7. Conclusions

Based on an innovative clustering approach, the first hydrometeor classification for Amazon tropical-equatorial precipitation systems has been realized by using research X-band DPOL radar deployed during both the GoAmazon2014/5 and ACRIDICON-CHUVA field experiments. The AHC method
640 was broadly equivalent to GR15 and built using Z_H , Z_{DR} , K_{DP} and p_{HV} polarimetric radar variables together with temperature information extracted from sounding balloons. The clustering approach allowed gathering of polarimetric radar observations that exhibit similarities amongst themselves within both wet and dry seasons and both stratiform and convective regions. Sensitivity analysis during the wet season was performed through different linkage rules and showed that both the weighted and Ward
645 linkage rules were the most suitable for this hydrometeor classification task. In this regard, a novel approach was tested to improve the 0 °C hydrometeor layer representation within the convective region.

While the 0 °C isotherm region is generally binarily represented, one can allow the liquid water content to overpass this region by setting simple rules. The final representation showed a realistic distribution and created new perspectives to respect polarimetric radar signatures as much as possible.

650 The AHC clustering outputs for both the wet and dry seasons and the stratiform and convective regions were investigated over the Manaus region with the complete datasets collected during 2014. Although previous studies were conducted for different latitudes and/or wavelengths, the retrieved hydrometeor types were found to be generally in agreement. Overall, typical cloud microphysical distributions within the stratiform precipitation regimes are characterized by five hydrometeors: drizzle/light rain, rain, wet
655 snow, aggregates, and ice crystals. On the other hand, convective regions exhibit more diversified microphysical populations with six (seven) retrieved hydrometeor types for the wet (dry) season: light rain, moderate rain, heavy rain, low-density graupel, (high-density graupel), aggregates, and ice crystals.

The present study also highlighted the potential of the clustering approach in comparison to a more
660 “classical” supervised fuzzy logic algorithm. For instance, the clustering results showed a better ability to delimit and distinguish the bright band region. The AHC method also allowed exploiting the higher sensitivity of the X-band radar and permitted retrieving three different rainfall regimes by exhibiting light, moderate, and heavy intensities.

The retrieved labelled clusters allowed making comparisons of the dominant microphysical species
665 involved during both the wet and dry seasons of Brazilian tropical precipitation systems. Thus, the main discrepancy relies on the presence of one more microphysical species within the convective region of

the dry season, defined as high-density graupel. This microphysical species is probably the result of a deeper convection associated with precipitation systems that occur during this period of the year.

Overall, the dry season Z_H , Z_{DR} , and K_{DP} distribution shapes were quite similar to those of the rainy
670 period; however, the distributions were shifted towards higher (lower) values for positive (negative) temperatures. The different rainfall intensities associated with the dry season generally exhibited higher Z_H , Z_{DR} , and K_{DP} values than those during the wet season, leading us to believe that ice microphysical processes outweigh warm rain microphysical mechanisms. Finally, the retrieved tropical microphysical species distribution showed that both aggregates and ice crystals were shifted towards higher radar
675 observable values in comparison to the mid-latitude X-band definition. These signatures might be due to the presence of a higher humidity amount within tropical regions, which may allow more dendritic-plate growth of aggregates and ice crystals microphysical species.

Although the year 2014 was representative and complied with typical tropical precipitation events, the
680 present study could be strengthened by an extended dataset as well as the use of i) in situ observations for validation tasks and ii) aerosols information to investigate microphysical differences between the wet and dry season. Nevertheless, this first detailed analysis of dominant hydrometeor distributions within tropical precipitation systems is promising and could also be extended to other radar frequencies and operational DPOL radars. Such improvements could be useful to identify key microphysical
685 parameters for nowcasting issues, which are expected to be investigated in the near future through both the SOS-CHUVA (Brazil) and RELAMPAGO (Argentina) research projects. In this regard, the clustering methodology could be enhanced by taking into account the Doppler velocities to explore the

microphysical processes involved within vigorous updraft/downdraft regions of the cloud. Finally, these results could also be helpful in evaluating the microphysical parameterization schemes used within
690 high-resolution numerical weather prediction models.

695

Acknowledgements

The authors would like to especially thank Jacopo Grazioli for fruitful discussions about the clustering method that helped refine the ideas developed in this study. The contribution of the first author was
700 supported by the São Paulo Research Foundation (FAPESP) under grants 2016/16932-8 and 2015/14497-0 for the SOS-CHUVA project. Also, the ACRIDICON-CHUVA campaign was partly funded by the German Research Foundation (Deutsche Forschungsgemeinschaft, DFG Priority Program SPP 1294).

705

References

710 Al-Sakka H, Boumahmoud AA, Fradon B, Frasier SJ and Tabary P. 2013. A New Fuzzy Logic Hydrometeor Classification Scheme Applied to the French X-, C-, and S-Band Polarimetric Radars. *J. Appl. Meteor. Climatol.*, **52**, 2328-2344.

American Meteorological Society, cited 2018: Rain. Glossary of Meteorology. [Available online at
715 <http://glossary.ametsoc.org/wiki/rain.>]

Artaxo, P., Martins, J. V., Yamasoe, M. A., Procópio, A. S., Pauliquevis, T. M., Andreae, M. O., ... & Leal, A. M. C. 2002. Physical and chemical properties of aerosols in the wet and dry seasons in Rondônia, Amazonia. *Journal of Geophysical Research: Atmospheres*, *107*(D20).

720

Augros, C., Caumont, O., Ducrocq, V., Gaussiat, N., & Tabary, P. 2016. Comparisons between S-, C-and X-band polarimetric radar observations and convective-scale simulations of the HyMeX first special observing period. *Quarterly Journal of the Royal Meteorological Society*, *142*(S1), 347-362.

725 Aydin K, Seliga TA, Balaji V. 1986. Remote sensing of hail with a dual linear polarization radar. *J. Clim. Appl. Meteorol.* *25*: 1475–1484.

Bechini, R., Chandrasekar, V., Cremonini, R., & Lim, S. (2010, September). Radome attenuation at X-band radar operations. In *Proc. Sixth European Conf. on Radar in Meteorology and Hydrology*.

730

Bechini, R. and V. Chandrasekar, 2015: A Semisupervised Robust Hydrometeor Classification Method for Dual-Polarization Radar Applications. *J. Atmos. Oceanic Technol.*, *32*, 22–47, <https://doi.org/10.1175/JTECH-D-14-00097.1>

- 735 Besic, N., Figueras i Ventura, J., Grazioli, J., Gabella, M., Germann, U., and Berne, A.: Hydrometeor
classification through statistical clustering of polarimetric radar measurements: a semi-supervised
approach, *Atmos. Meas. Tech.*, 9, 4425-4445, <https://doi.org/10.5194/amt-9-4425-2016>, 2016
- 740 Braga, R. C., Rosenfeld, D., Weigel, R., Jurkat, T., Andreae, M. O., Wendisch, M., Pöschl, U., Voigt,
C., Mahnke, C., Borrmann, S., Albrecht, R. I., Molleker, S., Vila, D. A., Machado, L. A. T., and
Grulich, L.: Further evidence for CCN aerosol concentrations determining the height of warm rain and
ice initiation in convective clouds over the Amazon basin, *Atmos. Chem. Phys.*, 17, 14433-14456,
<https://doi.org/10.5194/acp-17-14433-2017>, 2017.
- 745 Bringi, V. N., and V. Chandrasekar. *Polarimetric Doppler weather radar: principles and applications*.
Cambridge university press, 2001.
- Bringi, V. N., Thurai, R., and Hanesen, R.: *Dual-Polarization Weather Radar Handbook*, AMS-
Gematronik GmbH, 2007.
- 750 Cazenave, F., Gosset, M., Kacou, M., Alcoba, M., Fontaine, E., Duroure, C., & Dolan, B. (2016).
Characterization of hydrometeors in Sahelian convective systems with an X-band radar and comparison
with in situ measurements. Part I: Sensitivity of polarimetric radar particle identification retrieval and
case study evaluation. *Journal of Applied Meteorology and Climatology*, 55(2), 231-249.
- 755 Cecchini, M. A., Machado, L. A. T., Wendisch, M., Costa, A., Krämer, M., Andreae, M. O., Afchine,
A., Albrecht, R. I., Artaxo, P., Borrmann, S., Fütterer, D., Klimach, T., Mahnke, C., Martin, S. T.,
Minikin, A., Molleker, S., Pardo, L. H., Pöhlker, C., Pöhlker, M. L., Pöschl, U., Rosenfeld, D., and
Weinzierl, B.: Illustration of microphysical processes in Amazonian deep convective clouds in the
gamma phase space: introduction and potential applications, *Atmos. Chem. Phys.*, 17, 14727-14746,
760 <https://doi.org/10.5194/acp-17-14727-2017>, 2017.

Chandrasekar, V., Keranen, R., Lim, S., and D., M.: Recent advances in classification of observations from dual polarization weather radars, *Atmos. Res.*, 119, 9–111, 2013.

765 Dolan B. and Rutledge SA. 2009. A Theory-Based Hydrometeor Identification Algorithm for X-Band Polarimetric Radars. *J. Atmos. Oceanic Technol.*, **26**, 2071-2088.

Dolan B, Rutledge SA, Lim S, Chandrasekar V and Thurai M. 2013. A robust C-Band hydrometeor identification algorithm and application to a long-term polarimetric radar dataset. *J. Appl. Meteor. Climatol.*, **52**, 2162-2186.

775 Durden, S. L., Kitlyakara, A., Im, E., Tanner, A. B., Haddad, Z. S., Li, F. K., & Wilson, W. J. 1997. ARMAR observations of the melting layer during TOGA COARE. *IEEE transactions on geoscience and remote sensing*, 35(6), 1453-1456.

El-Magd A, Chandrasekar V, Bringi V, Strapp W. 2000. Multiparameter radar and in situ aircraft observation of graupel and hail. *IEEE Trans. Geosci. Remote Sens.* 38: 570–578.

780 Grazioli, J., Tuia, D., and Berne, A.: Hydrometeor classification from polarimetric radar measurements: a clustering approach, *Atmos. Meas. Tech.*, 8, 149-170, <https://doi.org/10.5194/amt-8-149-2015>, 2015.

Giangrande, S. E., Krause, J. M., & Ryzhkov, A. V. 2008. Automatic designation of the melting layer with a polarimetric prototype of the WSR-88D radar. *Journal of Applied Meteorology and Climatology*, 47(5), 1354-1364.

785

- Giangrande, S. E., T. Toto, M. P. Jensen, M. J. Bartholomew, Z. Feng, A. Protat, C. R. Williams, C. Schumacher, and L. Machado. 2017. Convective cloud vertical velocity and mass-flux characteristics from radar wind profiler observations during GoAmazon2014/5, *J. Geophys. Res. Atmos.*, 121, 12,891–12,913, doi:10.1002/2016JD025303.
- 790
- Grazioli, J., Genthon, C., Boudevillain, B., Duran-Alarcon, C., Del Guasta, M., Madeleine, J.-B., and Berne, A.: Measurements of precipitation in Dumont d'Urville, Adélie Land, East Antarctica, *The Cryosphere*, 11, 1797-1811, <https://doi.org/10.5194/tc-11-1797-2017>, 2017.
- 795
- Hall MPM, Goddard JW F and Cherry SM. 1984. Identification of hydrometeors and other targets by dual-polarization radar. *Radio Science*, **19**, 132-140.
- Hallett, J. and Mossop, S. C. C.: Production of secondary ice particles during the riming process, *Nature*, 249, 26–28, 1974.
- 800
- Heymsfield, A.J., A. Bansemer, M.R. Poellot, and N. Wood, 2015: Observations of Ice Microphysics through the Melting Layer. *J. Atmos. Sci.*, **72**, 2902–2928, <https://doi.org/10.1175/JAS-D-14-0363.1>
- 805
- Höllner H, Hagen M, Meischner PF, Bringi VN and Hubbert J. 1994. Life Cycle and Precipitation Formation in a Hybrid-Type Hailstorm Revealed by Polarimetric and Doppler Radar Measurements. *J. Atmos. Sci.*, **51**, 2500-2522.
- 810
- Houze, R.A., 1997: Stratiform Precipitation in Regions of Convection: A Meteorological Paradox?, *Bull. Amer. Meteor. Soc.*, **78**, 2179–2196, [https://doi.org/10.1175/1520-0477\(1997\)078<2179:SPIROC>2.0.CO;2](https://doi.org/10.1175/1520-0477(1997)078<2179:SPIROC>2.0.CO;2)

Hubbert, J., and V. N. Bringi. "An iterative filtering technique for the analysis of copolar differential
815 phase and dual-frequency radar measurements." *Journal of Atmospheric and Oceanic Technology* 12.3
1995: 643-648.

Illingworth AJ, Blackman TM. 2002. The need to represent raindrop size spectra as normalized gamma
distributions for the interpretation of polarization radar observations. *J. Appl. Meteorol.* 41:286–297.

820

Jain, A. K., Duin, R. P. W., and Mao, J. C.: Statistical pattern recognition: A review, *IEEE Trans. Pattern Analysis Machine Intell.*, 22, 4–37, doi:10.1109/34.824819, 2000.

Jäkel, E., Wendisch, M., Krisna, T. C., Ewald, F., Kölling, T., Jurkat, T., Voigt, C., Cecchini, M. A.,
825 Machado, L. A. T., Afchine, A., Costa, A., Krämer, M., Andreae, M. O., Pöschl, U., Rosenfeld, D., and
Yuan, T.: Vertical distribution of the particle phase in tropical deep convective clouds as derived from
cloud-side reflected solar radiation measurements, *Atmos. Chem. Phys.*, 17, 9049-9066,
<https://doi.org/10.5194/acp-17-9049-2017>, 2017.

830 Kumjian, M.R. and A.V. Ryzhkov, 2008: Polarimetric Signatures in Supercell Thunderstorms. *J. Appl. Meteor. Climatol.*, **47**, 1940–1961, <https://doi.org/10.1175/2007JAMC1874.1>

Kumjian, M. R., & Ryzhkov, A. V. 2010. The impact of evaporation on polarimetric characteristics of
rain: Theoretical model and practical implications. *Journal of Applied Meteorology and Climatology*,
835 *49*(6), 1247-1267.

Leary, C. A., & Houze Jr, R. A. (1979). Melting and evaporation of hydrometeors in precipitation from
the anvil clouds of deep tropical convection. *Journal of the Atmospheric Sciences*, *36*(4), 669-679.

840 Liu H and Chandrasekar V. 2000. Classification of Hydrometeors Based on Polarimetric Radar Measurements: Development of Fuzzy Logic and Neuro-Fuzzy Systems, and In Situ Verification. *J. Atmos. Oceanic Technol.*, **17**, 140-164.

Machado, L. A. T., Laurent, H., Dessay, N., & Miranda, I. 2004. Seasonal and diurnal variability of
845 convection over the Amazonia: a comparison of different vegetation types and large scale forcing. *Theoretical and Applied Climatology*, **78**(1-3), 61-77.

Machado, L. A. T., Calheiros, A. J. P., Biscaro, T., Giangrande, S., Silva Dias, M. A. F., Cecchini, M. A., Albrecht, R., Andreae, M. O., Araujo, W. F., Artaxo, P., Borrmann, S., Braga, R., Burleyson, C.,
850 Eichholz, C. W., Fan, J., Feng, Z., Fisch, G. F., Jensen, M. P., Martin, S. T., Pöschl, U., Pöhlker, C., Pöhlker, M. L., Ribaud, J.-F., Rosenfeld, D., Saraiva, J. M. B., Schumacher, C., Thalman, R., Walter, D., and Wendisch, M.: Overview: Precipitation characteristics and sensitivities to environmental conditions during GoAmazon2014/5 and ACRIDICON-CHUVA, *Atmos. Chem. Phys.*, **18**, 6461-6482, <https://doi.org/10.5194/acp-18-6461-2018>, 2018.

855

Martin, S.T.; Artaxo, P.; Machado, L.A.T.; Manzi, A.O.; Souza, R.A.F.; Schumacher, C.; Wang, J.; Andreae, M.O.; Barbosa, H.M.J.; Fan, J.; et al. Introduction: Observations and Modeling of the Green Ocean Amazon (GoAmazon2014/5). *Atmos. Chem. Phys.* 2016, **16**, 4785–4797.

860 Martin, S.T., , and coauthors, 2017. The Green Ocean Amazon Experiment (GoAmazon2014/5) Observes Pollution Affecting Gases, Aerosols, Clouds, and Rainfall over the Rain Forest. *Bulletin of the American Meteorological Society* **98**, no. 5 (2017): 981-997.

Marzano F, Scaranari D, Celano M, Alberoni PP, Vulpiani G and Montopoli M. 2006. Hydrometeor
865 classification from dual-polarized weather radar: extending fuzzy logic from S-band to C-band data. *Advances in Geosciences*, 2006, **7**, 109-114.

Marzano F, D. Scaranari, M. Montopoli, and G. Vulpiani, 2008: Supervised classification and estimation of hydrometeors from C-band dual-polarized radars: A Bayesian approach. IEEE Trans. Geosci. Remote, 46, 85–98, doi:10.1109/TGRS.2007.906476.

Marzano, F. S., Botta, G., and Montopoli, M.: Iterative Bayesian retrieval of hydrometeor content from X-band polarimetric weather radar, IEEE T. Geosci. Remote Sens., 48, 3059–3074, 2010.

875 Matrosov, S. Y., Clark, K. A., & Kingsmill, D. E. (2007). A polarimetric radar approach to identify rain, melting-layer, and snow regions for applying corrections to vertical profiles of reflectivity. *Journal of applied meteorology and climatology*, 46(2), 154-166.

Mendel J. M., “Fuzzy logic systems for engineering: A tutorial,” Proc. IEEE, vol. 83, no. 3, pp. 345–
880 377, Mar. 1995.

Mishchenko, M. I. and Travis, L. D.: Capabilities and limitations of a current Fortran implementation of the T-Matrix method for randomly oriented, rotationally symmetric scatterers, *Journal of Quantitative Spectroscopy and Radiative Transfer*, 60, 3, 309–324, 1998.

885 Müllner D., 2011. Modern hierarchical, agglomerative clustering algorithms. *arXiv preprint arXiv:1109.2378*.

Oliveira, R., Maggioni, V., Vila, D., & Morales, C. (2016). Characteristics and diurnal cycle of GPM
890 rainfall estimates over the central amazon region. *Remote Sensing*, 8(7), 544.

Park HS, Ryzhkov AV, Zrnić D and Kim KE. 2009. The Hydrometeor Classification Algorithm for the Polarimetric WSR-88D: Description and Application to an MCS. *Wea. Forecasting*, 24, 730-748.

895 Penide, G., Kumar, V. V., Protat, A., & May, P. T. (2013). Statistics of drop size distribution parameters and rain rates for stratiform and convective precipitation during the north Australian wet season. *Monthly Weather Review*, 141(9), 3222-3237.

Ribaudo J-F., O. Bousquet, S. Coquillat, Relationships between total lightning activity, microphysics and
900 kinematics during the 24 September 2012 HyMeX bow-echo system, *Quarterly Journal of the Royal Meteorological Society*, 2016a, 142, 298

Ribaudo J-F., Bousquet O, Coquillat S, Al-Sakka H, Lambert D, Ducrocq V, Fontaine E. 2016b. Evaluation and application of hydrometeor classification algorithm outputs inferred from multi-
905 frequency dual-polarimetric radar observations collected during HyMeX. *Q. J. R. Meteorol. Soc.*, doi:10.1002/qj.2589

Rosenfeld, D., and C. W. Ulbrich, 2003: Cloud microphysical properties, processes, and rainfall estimation opportunities. *Radar and Atmospheric Science: A Collection of Essays in Honor of David*
910 *Atlas. Meteor. Monogr.*, No. 52, Amer. Meteor. Soc., 237–258.

Ryzhkov, A. V., Schuur, T. J., Burgess, D. W., Heinselman, P. L., Giangrande, S. E., and Zrnic, D. S.: The joint polarization experiment, polarimetric rainfall measurements and hydrometeor classification, *Bull. Amer. Meteor. Soc.*, 86, 809–824, doi:10.1175/BAMS-86-6-809, 2005.

915

Ryzhkov, A. V., Kumjian, M. R., Ganson, S. M., & Khain, A. P. 2013. Polarimetric radar characteristics of melting hail. Part I: Theoretical simulations using spectral microphysical modeling. *Journal of Applied Meteorology and Climatology*, 52(12), 2849-2870.

920 Schneebeli, M., Sakuragi, J., Biscaro, T., Angelis, C. F., Carvalho da Costa, I., Morales, C., Baldini, L., and Machado, L. A. T.: Polarimetric X-band weather radar measurements in the tropics: radome and

rain attenuation correction, *Atmos. Meas. Tech.*, 5, 2183-2199, <https://doi.org/10.5194/amt-5-2183-2012>, 2012.

925 Segond M.-L., Tabary, P., Parent du Châtelet, J., 2007. Quantitative precipitation estimations from operational polarimetric radars for hydrological applications, Preprints. In: 33rd Int. Conf. on Radar Meteorology, AMS, Cairns, Australia, August 2007.

Seliga, T. A., and V. N. Bringi, 1976: Potential use of radar differential reflectivity measurements at
930 orthogonal polarizations for measuring precipitation. *J. Appl. Meteor.*, 15, 69–76, doi:10.1175/1520-0450(1976)015,0069:PUORDR.2.0.CO;2.

Smyth, T. J., & Illingworth, A. J. (1998). Radar estimates of rainfall rates at the ground in bright band and non-bright band events. *Quarterly Journal of the Royal Meteorological Society*, 124(551), 2417-
935 2434.

Steiner M, Houze Jr RA, Yuter SE. Climatological characterization of three-dimensional storm structure from operational radar and rain gauge data. *Journal of Applied Meteorology*. 1995 Sep;34(9):1978-2007.

940

Straka J and Zrnić DS. 1993. An algorithm to deduce hydrometeor types and contents from multiparameter radar data. Preprints, *26th Conf. on Radar Meteorology*, Norman, OK, Amer. Meteor. Soc., 513-515.

945 Straka, J. M., 1996: Hydrometeor fields in a supercell storm as deduced from dual polarization radar. Preprints, 18th Conf. on Severe Local Storms, San Francisco, CA, Amer. Meteor. Soc., 551–554.

- Straka, Jerry M., Dusan S. Zrnić, and Alexander V. Ryzhkov. "Bulk hydrometeor classification and quantification using polarimetric radar data: Synthesis of relations." *Journal of Applied Meteorology* 950 39.8 (2000): 1341-1372.
- Testud, J., E. Le Bouar, E. Obligis, and M. Ali-Meheni, 2000: The rain profiling algorithm applied to polarimetric weather radar. *J. Atmos. Oceanic Technol.*, 17, 332–356.
- 955 Thompson, E. J., S. A. Rutledge, B. Dolan, V. Chandrasekar, and B. L. Cheong, 2014: A dual-polarization radar hydrometeor classification algorithm for winter precipitation. *J. Atmos. Oceanic Technol.*, 31, 1457–1481, doi:10.1175/JTECH-D-13-00119.1.
- Vivekanandan J, Ellis SM, Oye R, Zrnić DS, Ryzhkov AV and Straka J. 1999. Cloud Microphysics 960 Retrieval Using S-band Dual-Polarization Radar Measurements. *Bull. Amer. Meteor. Soc.*, **80**, 381-388.
- Wang, D., Giangrande, S. E., Bartholomew, M. J., Hardin, J., Feng, Z., Thalman, R., and Machado, L. A. T.: The Green Ocean: precipitation insights from the GoAmazon2014/5 experiment, *Atmos. Chem. Phys.*, 18, 9121-9145, <https://doi.org/10.5194/acp-18-9121-2018>, 2018.
- 965 Ward, J.: Hierarchical grouping to optimize an objective function, *J. Am. Stat. Assoc.*, 58, 236–244, 1963.
- Wen G, Protat A, May PT, Wang X, Moran W. A cluster-based method for hydrometeor classification 970 using polarimetric variables. Part I: Interpretation and analysis. *Journal of Atmospheric and Oceanic Technology*. 2015 Jul;32(7):1320-40.
- Wen G, Protat A, May PT, Moran W, Dixon M. A cluster-based method for hydrometeor classification using polarimetric variables. Part II: Classification. *Journal of Atmospheric and Oceanic Technology*. 975 2016 Jan;33(1):45-60.

Wendisch, M., and coauthors, 2016. ACRIDICON–CHUVA CAMPAIGN Studying Tropical Deep Convective Clouds and Precipitation over Amazonia Using the New German Research Aircraft HALO. *Bull. Amer. Meteor. Soc.*, **97**, 1885–1908, <https://doi.org/10.1175/BAMS-D-14-00255.1>

980

Wolfensberger, D., Scipion, D., & Berne, A. 2016. Detection and characterization of the melting layer based on polarimetric radar scans. *Quarterly Journal of the Royal Meteorological Society*, *142*(S1), 108-124.

985 Wolfensberger, D. and Berne, A.: From model to radar variables: a new forward polarimetric radar operator for COSMO, *Atmos. Meas. Tech. Discuss.*, <https://doi.org/10.5194/amt-2017-427>, 2018

Zrnić, D. S., A. Ryzhkov, J. Straka, Y. Liu, and J. Vivekanandan, 2001: Testing a procedure for automatic classification of hydrometeor types. *J. Atmos. Oceanic Technol.*, *18*, 892–913, [doi:10.1175/1520-0426\(2001\)018,0892:TAPFAC.2.0.CO;2](https://doi.org/10.1175/1520-0426(2001)018,0892:TAPFAC.2.0.CO;2).

990

995

1000

List of Tables

Table 1: *X-band dual-polarization radar characteristics*

1005

Table 2: *Distance formulas for the weighted, centroid and Ward linkage rules. Here, S and T are two clusters joined into a new cluster, whereas V is any another cluster. n_S , n_T , n_V are the number of objects contained in the clusters S , T , V , respectively.*

1010 **Table 3:** *Confusion matrix comparing the clustering outputs from the stratiform region of the wet season and hydrometeor species retrieved from the adapted fuzzy logic.*

Table 4: *Same as Table 3, but for the convective region of the wet season.*

1015 **Table 5:** *Same as Table 3, but for the stratiform region of the dry season.*

Table 6: *Same as Table 3, but for the stratiform region of the dry season.*

1020

1025

1030 **List of figures**

Figure 1: Schematic representation of the different hydrometeor classification techniques and their principal associated benchmarks.

1035 **Figure 2:** (a) Geographical localization of the GoAmazon2014/5 and ACRIDICON-CHUVA experiments. (b) X-band DPOL radar coverage and its associated topography.

Figure 3: Evolution of the variance explained for different clustering linkage rules. Each linkage method is subdivided in terms of stratiform (dashed line) and convective (solid line) regions. The orange vertical span highlights the interval potentially associated with the optimal number of clusters.

1040

Figure 4: X-band DPOL radar observables and the corresponding retrieved hydrometeor classification outputs at 12:07 UTC on 21 February 2014, along the azimuth 290°. DPOL radar observables are shown in panels: (a) Z_H , (b) Z_{DR} , (c) K_{DP} , and (d) p_{HV} . Comparisons of retrieved hydrometeors for clustering outputs based on (e) weighted, (f) centroid, and (g) Ward linkage rules and (h) fuzzy logic scheme outputs. In panels (e)-(f)-(g), each number corresponds to a different cluster. 'S' stands for stratiform regimes, whereas 'C' is for convective regimes.

1045

Figure 5: Same as Figure 4, but for 13:57 UTC on 13 February 2014, along the azimuth 200°.

1050 **Figure 6:** Clustering hydrometeor classification retrieved from the X-band radar at 12:07 UTC on 21 February 2014, along the azimuth 290°. (a) With temperature constraint, (b) without temperature constraint.

Figure 7: Violin plot of cluster outputs retrieved for the stratiform regime of the wet season (DZ: drizzle, RN: rain, WS: wet snow, AG: aggregates, IC: ice crystals). The thick black bar in the centre represents the interquartile range, and the thin black line extended from it represents the 95 % confidence intervals, while the white dot is the median.

1055

Figure 8: Same as Figure 7, but for the convective regime of the wet season (LR: light rain, MR: moderate rain, HR: heavy rain, GR: graupel, AG: aggregates, IC: ice crystals).

1060

Figure 9: X-band DPOL radar observables and the corresponding retrieved hydrometeor classification outputs at 21:26 UTC on 08 September 2014, along the azimuth 200°. DPOL radar observables are shown in panels: (a) Z_H , (b) Z_{DR} , (c) K_{DP} , and (d) p_{HV} . Comparisons of retrieved hydrometeors for

1065 clustering outputs based on (e) weighted linkage rules and (f) the fuzzy logic scheme. In panels (e)-(f),
each number corresponds to a different cluster. 'S' stands for the stratiform region, whereas 'C' is for
the convective region.

Figure 10: Same as Figure 7, but for the stratiform regime of the dry season (DZ: drizzle, RN: rain,
1070 WS: wet snow, AG: aggregates, IC: ice crystals).

Figure 11: Same as Figure 9, but for an RHI at 18:16 UTC on 06 October 2014, along the azimuth
200°.

1075 **Figure 12:** Same as Figure 7, but for the convective regime of the dry season (LR: light rain, MR:
moderate rain, HR: heavy rain, LDG: low-density graupel, HDG: high-density graupel, AG:
aggregates, IC: ice crystals).

Figure 13: Violin plot comparison of pairs of stratiform hydrometeor types between the wet and dry
1080 seasons (DZ: drizzle, RN: rain, WS: wet snow, AG: aggregates, and IC: ice crystals).

Figure 14: Same as Figure 13, but for the convective precipitation regime (LR: light rain, MR:
moderate rain, HR: heavy rain, LDG: low-density graupel, HDG: high-density graupel, AG: aggregates,
and IC: ice crystals).

1085

1090

1095

1100

Location	(3.21°S; 60.6°W; 60.9m)
Radar Type	Pulsed
Polarization	H-V orthogonal
Transmission/reception	Simultaneous
Antenna	1.8 m diameter, 1.3° 3dB beamwidth
Antenna gain	43dB
Frequency	9.345 GHz
Maximum range detection	100 km
Range resolution	200 m
10 min PPI elevation angles	0.5°/1.3°/2.1°/3.2°/4.3°/5.6°/7.1°/8.8°/10.8°/13.0°/ 15.6°/18.5°/21.8°/25.6°/30.0°

Table 1: X-band dual-polarization radar characteristics

Linkage method	Distance formula for $d(S \cup T, V)$
Weighted	$\frac{d(S, V) + d(T, V)}{2}$
Centroid	$\sqrt{\frac{n_S d(S, V) + n_T d(T, V) - \frac{n_S n_T d(S, T)}{(n_S + n_T)^2}}{n_S + n_T}}$
Ward	$\sqrt{\frac{(n_S + n_V) d(S, V) + (n_T + n_V) d(T, V) - n_V d(S, T)}{n_S + n_T + n_V}}$

1105

Table 2: Distance formulas for the weighted, centroid and Ward linkage rules. Here, S and T are two clusters joined into a new cluster, whereas V is any another cluster. n_S , n_T , n_V are the number of objects contained in the clusters S , T , V , respectively.

1110

TYPE	DZ	RN	MH	WS	AG	LDG	HDG	VI	CR
1S	38.64 %	0.01 %	0.00 %	10.34 %	32.91 %	1.31 %	0.00 %	4.47 %	12.34 %
2S	0.02 %	0.21 %	0.00 %	43.51 %	42.66 %	11.91 %	0.00 %	0.02 %	1.67 %
3S	64.36 %	27.55 %	0.21 %	7.88 %	0.00 %	0.00 %	0.00 %	0.00 %	0.00 %
4S	5.75 %	7.27 %	0.02 %	86.02 %	0.53 %	0.11 %	0.00 %	0.03 %	0.27 %
5S	98.04 %	0.00 %	0.27 %	1.68 %	0.00 %	0.00 %	0.00 %	0.00 %	0.00 %

Table 3: Confusion matrix comparing the clustering outputs from the stratiform region of the wet season and hydrometeor species retrieved from the adapted fuzzy logic.

1115

1120

TYPE	DZ	RN	MH	WS	AG	LDG	HDG	VI	CR
6C	77.00 %	21.70 %	0.99 %	0.31 %	0.00 %	0.00 %	0.00 %	0.00 %	0.00 %
7C	0.00 %	0.16 %	0.00 %	21.69 %	7.70 %	69.01 %	1.44 %	0.00 %	0.00 %
8C	0.78 %	2.70 %	0.02 %	27.24 %	44.51 %	23.71 %	0.00 %	0.27 %	0.77 %
9C	0.10 %	0.00 %	0.00 %	9.86 %	55.90 %	5.83 %	0.00 %	9.15 %	19.16 %
10C	96.47 %	0.14 %	1.46 %	1.92 %	0.00 %	0.00 %	0.00 %	0.00 %	0.00 %
11C	31.42 %	62.98 %	1.24 %	4.36 %	0.00 %	0.00 %	0.00 %	0.00 %	0.00 %

Table 4: Same as Table 3, but for the convective region of the wet season.

1125

TYPE	DZ	RN	MH	WS	AG	LDG	HDG	VI	CR
1S	76.30 %	22.17 %	0.10 %	1.43 %	0.00 %	0.00 %	0.00 %	0.00 %	0.00 %
2S	92.32 %	4.36 %	0.65 %	2.63 %	0.02 %	0.00 %	0.00 %	0.01 %	0.00 %
3S	0.25 %	0.00 %	0.00 %	2.65 %	41.61 %	2.19 %	0.00 %	21.18 %	32.12 %
4S	0.97 %	1.30 %	0.00 %	49.30 %	18.46 %	26.83 %	0.23 %	0.44 %	2.48 %
5S	0.30 %	0.03 %	0.00 %	8.28 %	68.48 %	3.99 %	0.00 %	5.29 %	13.62 %

Table 5: Same as Table 3, but for the stratiform region of the dry season.

1130

1135

TYPE	DZ	RN	MH	WS	AG	LDG	HDG	VI	CR
6C	73.71 %	23.34 %	2.60 %	0.34 %	0.00 %	0.00 %	0.00 %	0.00 %	0.00 %
7C	21.61 %	73.56 %	1.00 %	3.83 %	0.01 %	0.00 %	0.00 %	0.00 %	0.00 %
8C	0.07 %	0.01 %	0.00 %	5.62 %	51.01 %	2.70 %	0.00 %	12.72 %	27.87 %
9C	0.16 %	2.32 %	0.00 %	27.80 %	7.41 %	60.40 %	1.86 %	0.00 %	0.04 %
10C	0.79 %	0.17 %	0.00 %	13.48 %	51.19 %	30.91 %	0.00 %	0.83 %	2.63 %
11C	0.00 %	15.29 %	0.51 %	64.19 %	0.19 %	11.4 %	7.72 %	0.00 %	0.00 %
12C	97.19 %	0.00 %	0.41 %	2.34 %	0.06 %	0.00 %	0.00 %	0.01 %	0.00 %

Table 6: Same as Table 3, but for the convective region of the dry season.

1140

1145

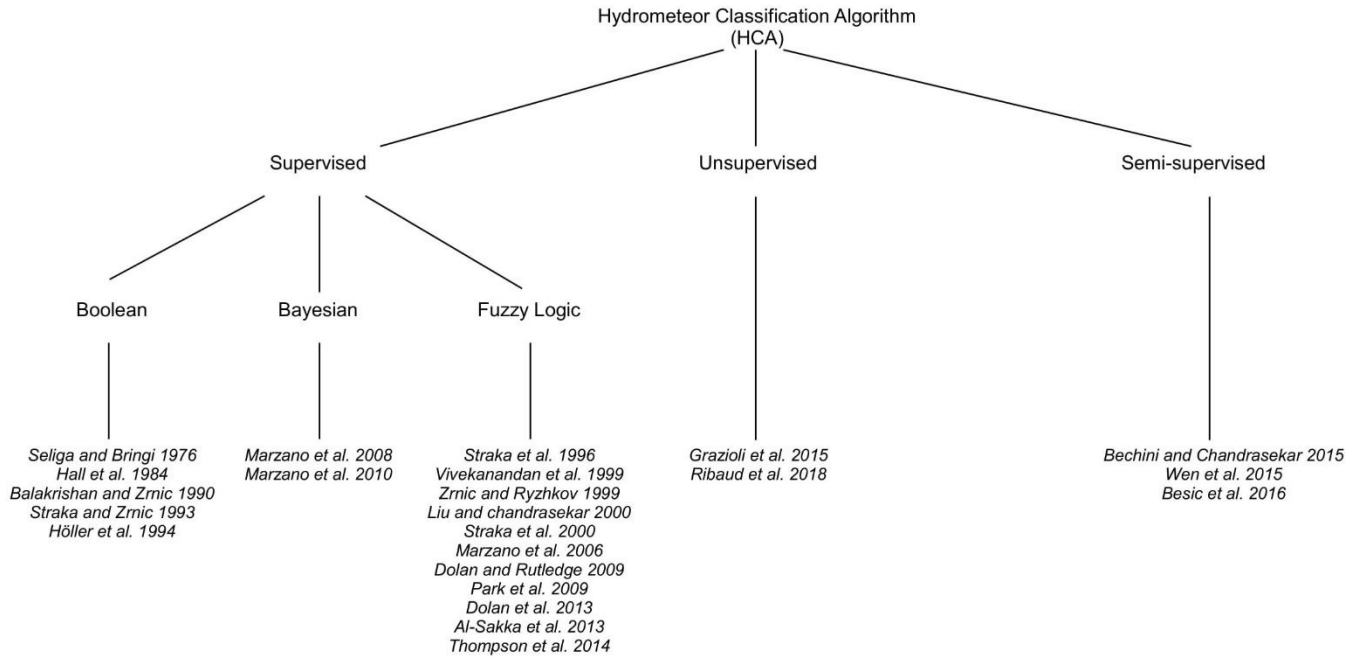


Figure 1: Schematic representation of the different hydrometeor classification techniques and their principal associated benchmarks.

1150

1155

1160

1165

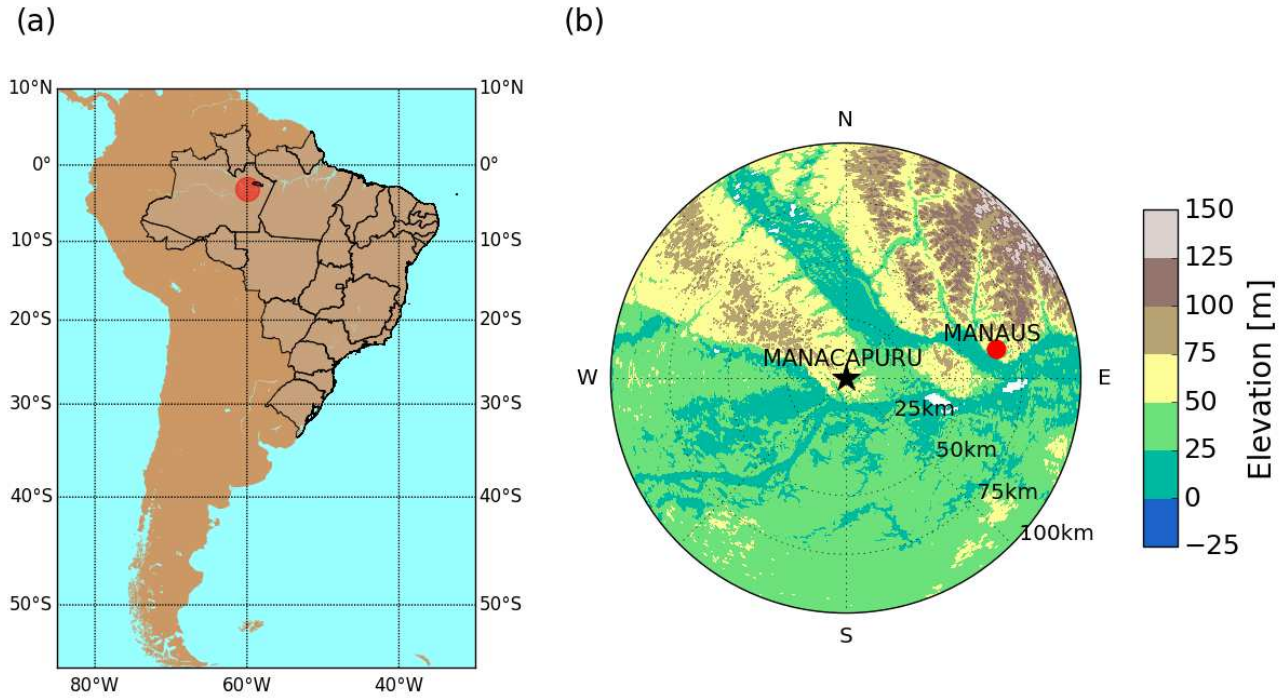
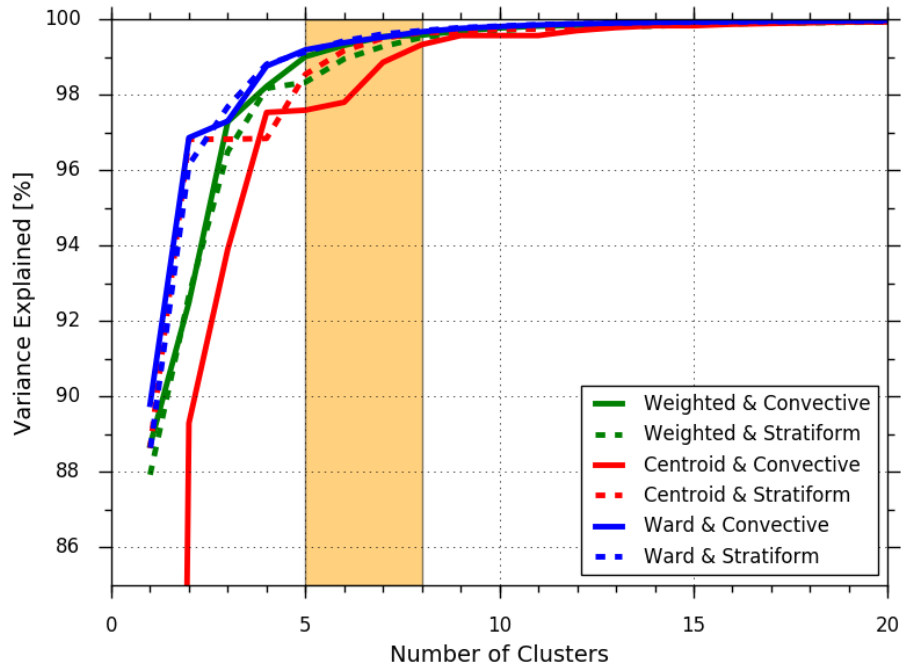


Figure 2: (a) Geographical localization of the GoAmazon2014/5 and ACRIDICON-CHUVA experiments. (b) X-band DPOL radar coverage and its associated topography.

1170

1175



1193

1200 **Figure 3:** Evolution of the variance explained for different clustering linkage methods. Each linkage
 1205 method is subdivided in terms of stratiform (dashed line) and convective (solid line) regions. The
 1210 orange vertical span highlights the interval potentially associated with the optimal number of clusters.

1205

1210

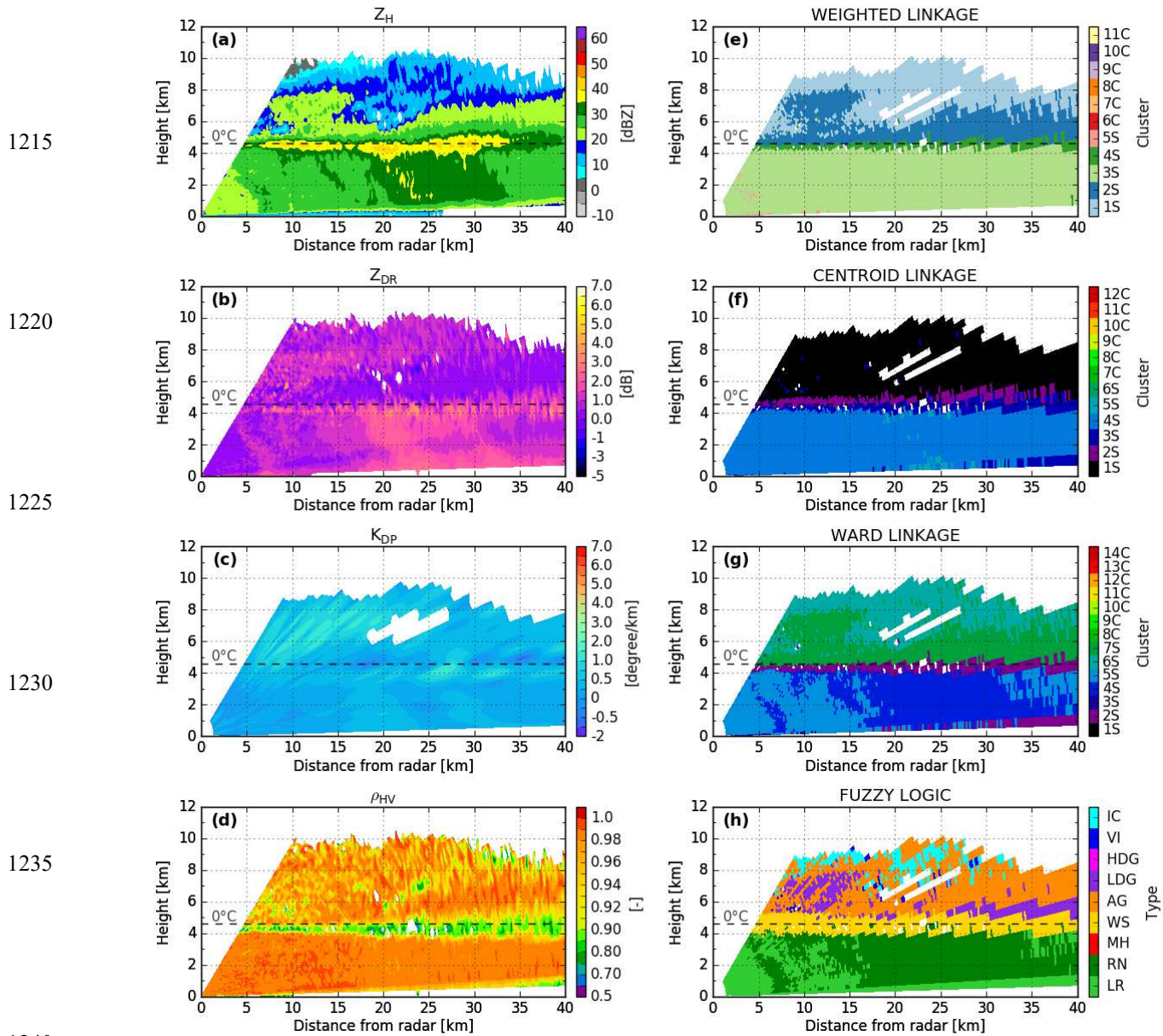


Figure 4: X-band DPOL radar observables and corresponding retrieved hydrometeor classification outputs at 12:07 UTC on 21 February 2014, along the azimuth 290°. DPOL radar observables are shown in panels (a) Z_H , (b) Z_{DR} , (c) K_{DP} , and (d) ρ_{HV} . Comparisons of retrieved hydrometeors for clustering outputs based on (e) weighted, (f) centroid, and (g) Ward linkage rules and (h) fuzzy logic scheme outputs. In panels (e)-(f)-(g), each number corresponds to a different cluster. 'S' stands for stratiform regimes, whereas 'C' is for convective regimes.

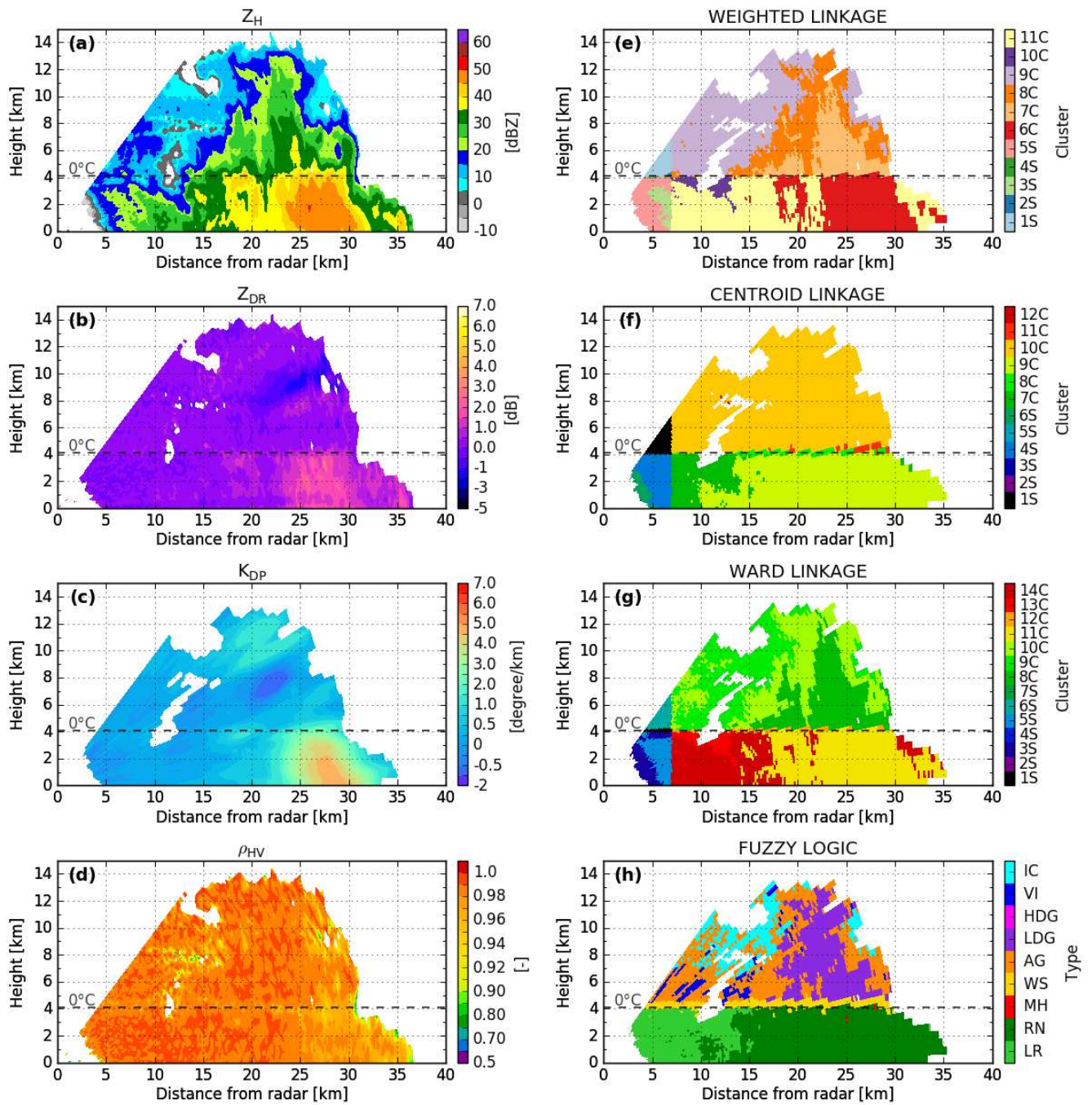


Figure 5: Same as Figure 4, but for 13:57 UTC on 13 February 2014, along the azimuth 200°.

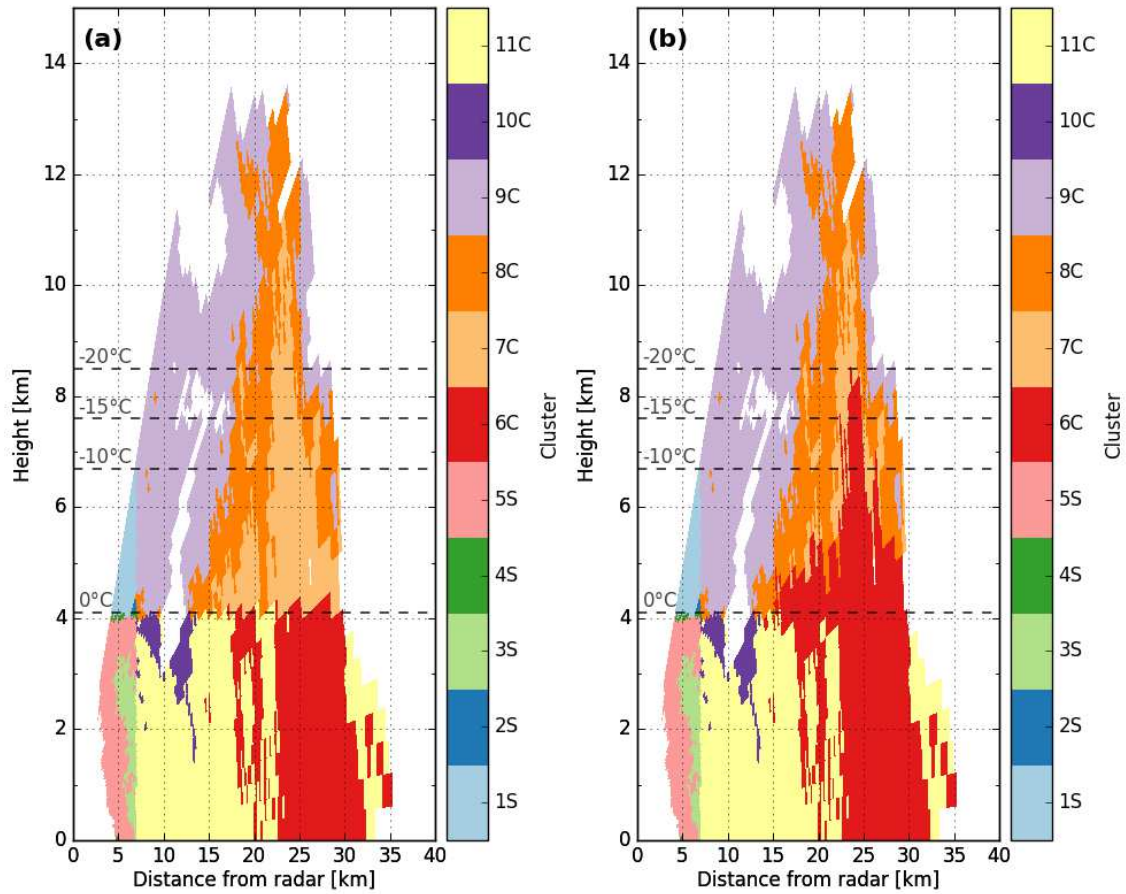
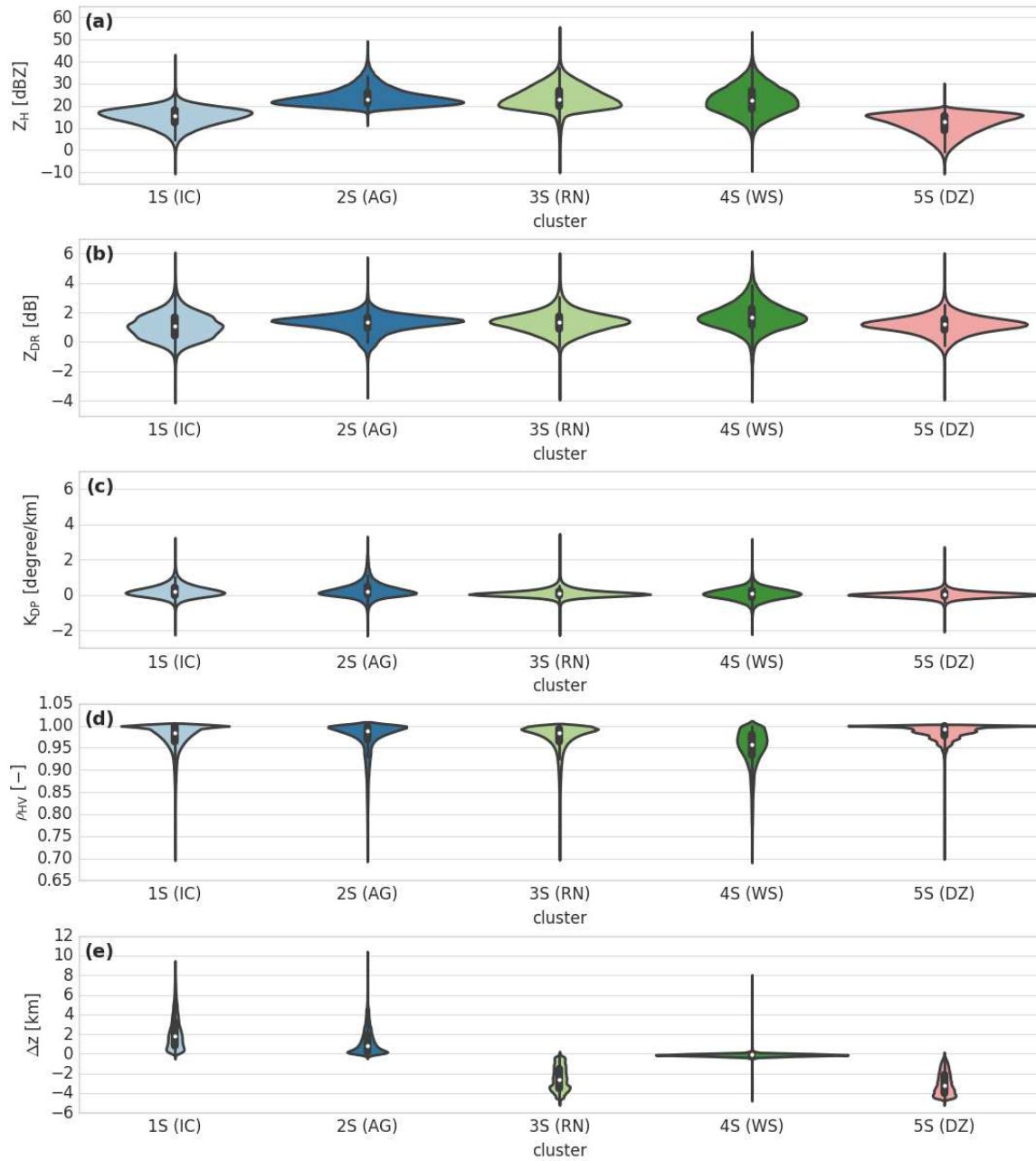


Figure 6: Clustering hydrometeor classification retrieved from the X-band radar at 12:07 UTC on 21 February 2014, along the azimuth 290°. (a) With temperature constraint, (b) without temperature constraint.

1255

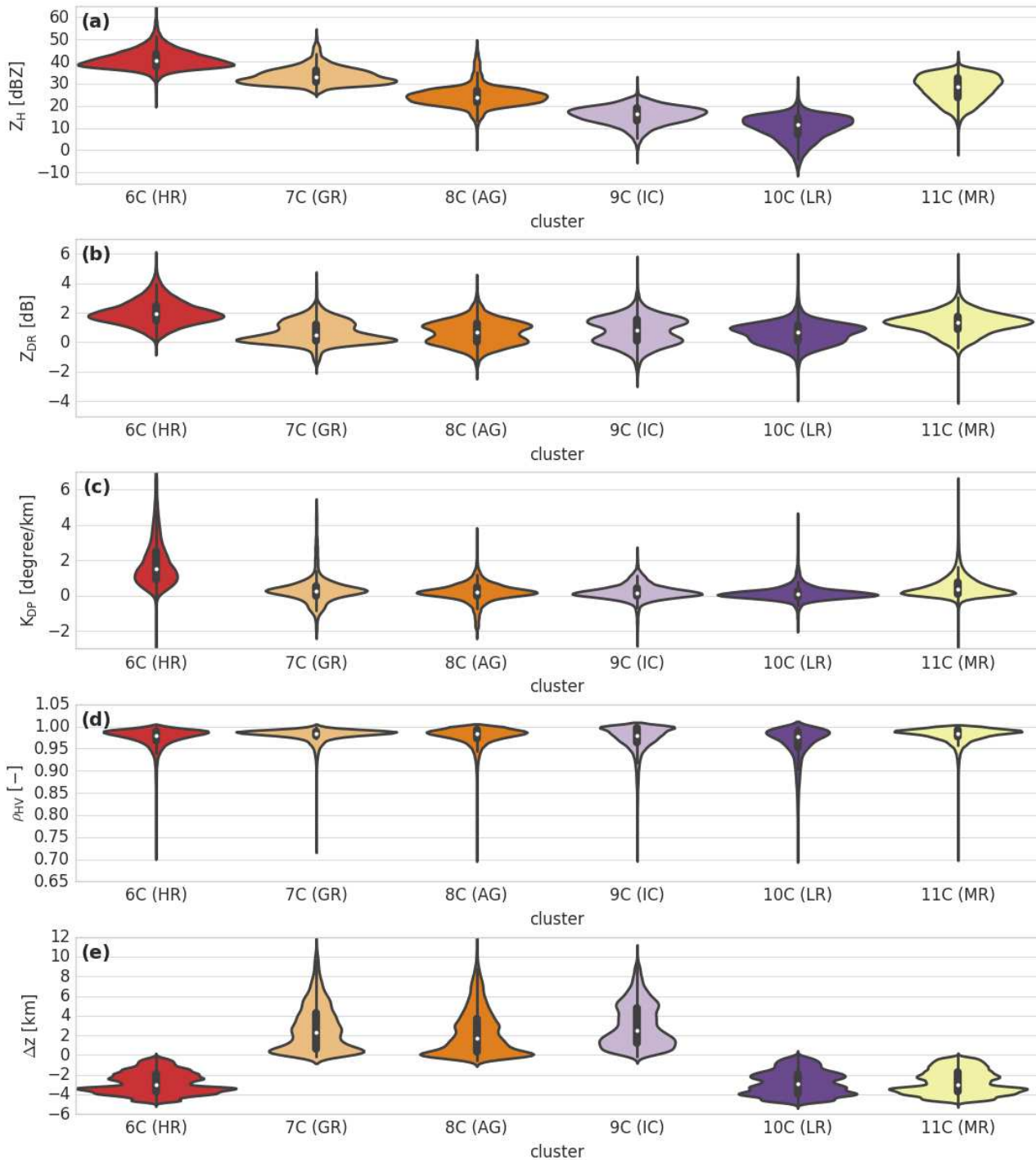
1260

1265



1295

Figure 7: Violin plot of cluster outputs retrieved for the stratiform regime of the wet season (DZ: drizzle, RN: rain, WS: wet snow, AG: aggregates, IC: ice crystals). The thick black bar in the centre represents the interquartile range, and the thin black line extended from it represents the 95 % confidence intervals, while the white dot is the median.



1300 **Figure 8:** Same as Figure 7, but for the convective regime of the wet season (LR: light rain, MR: moderate rain, HR: heavy rain, GR: graupel, AG: aggregates, IC: ice crystals).

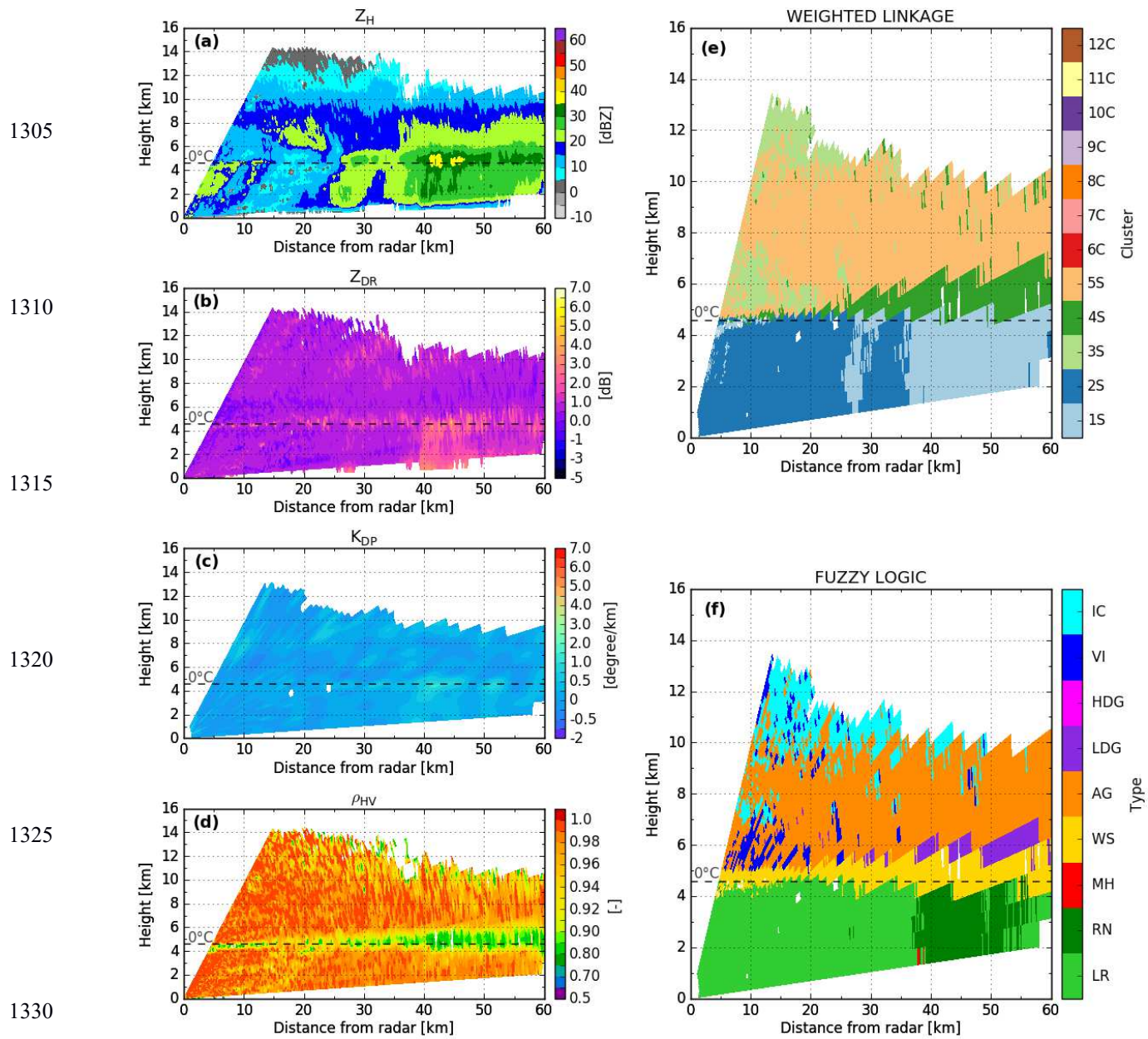


Figure 9: X-band DPOL radar observables and corresponding retrieved hydrometeor classification outputs at 21:26 UTC on 08 September 2014, along the azimuth 200°. DPOL radar observables are shown in panels (a) Z_H , (b) Z_{DR} , (c) K_{DP} , and (d) ρ_{HV} . Comparisons of the retrieved hydrometeor for clustering outputs based on (e) weighted linkage rules and (f) the fuzzy logic scheme. In panels (e)-(f), each number corresponds to a different cluster. ‘S’ stands for the stratiform region, whereas ‘C’ is for the convective region.

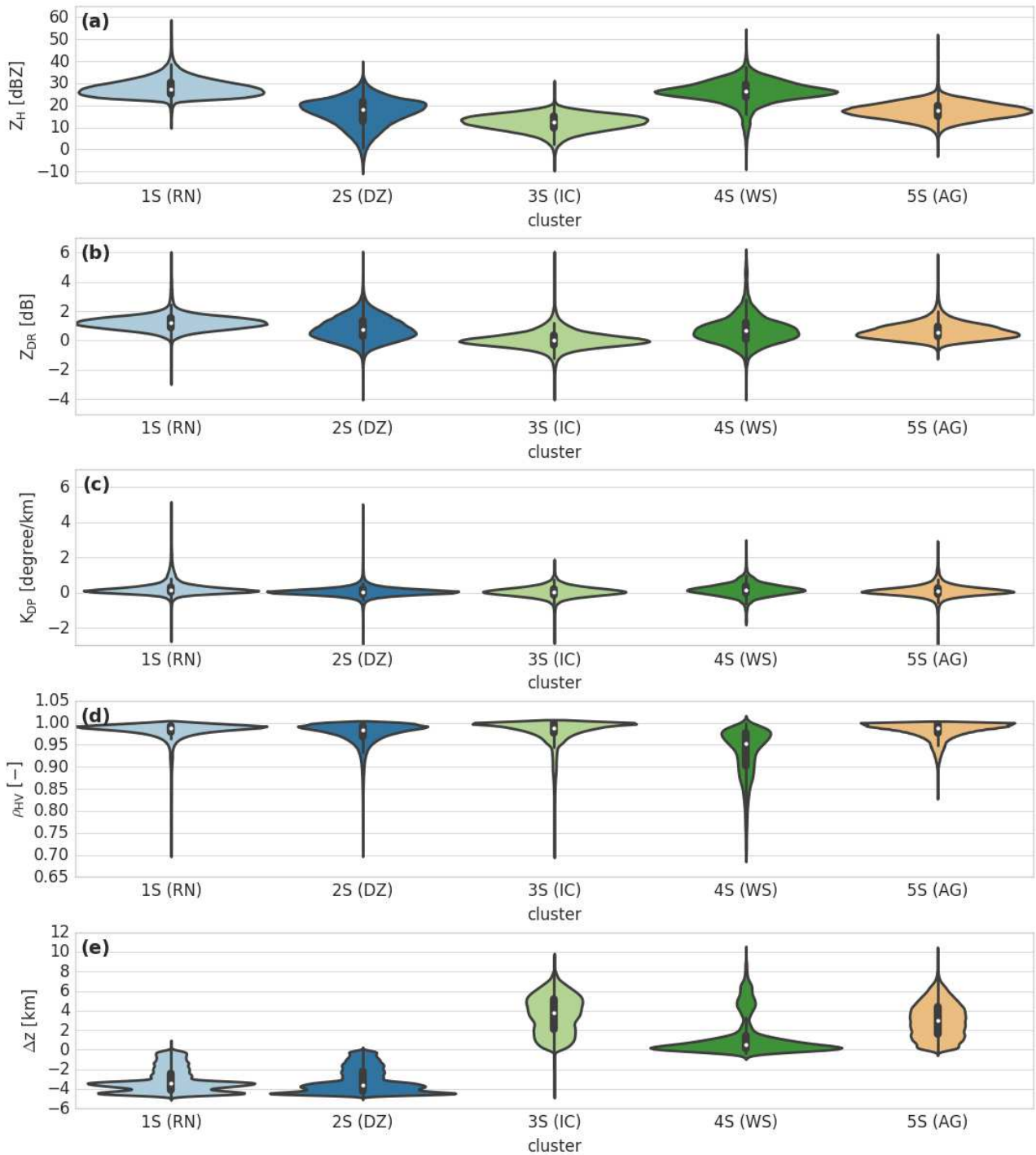
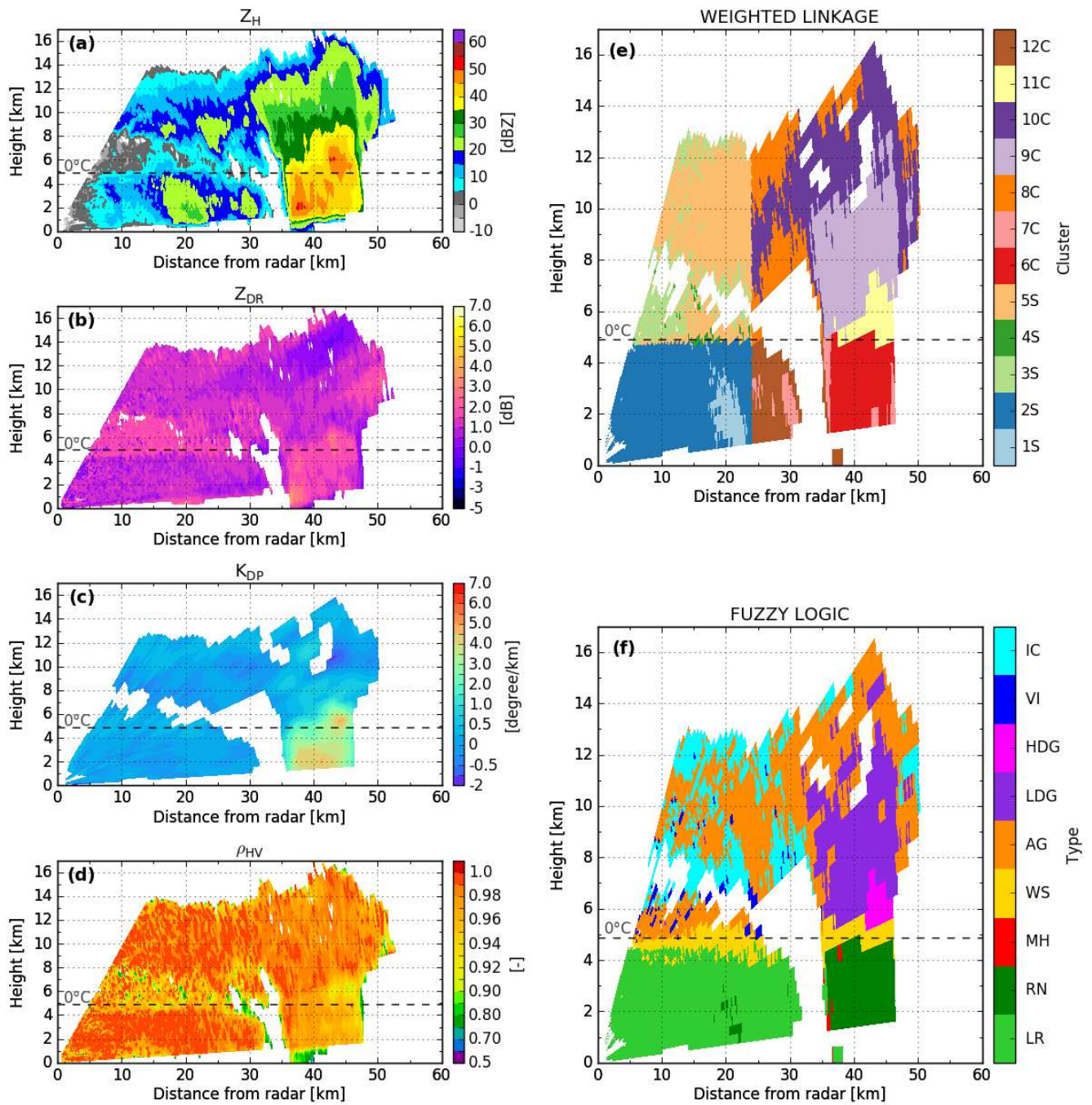


Figure 10: Same as Figure 7, but for the stratiform regime of the dry season (DZ: drizzle, RN: rain, WS: wet snow, AG: aggregates, IC: ice crystals).



1340

Figure 11: Same as Figure 9, but for an RHI at 18:16 UTC on 06 October 2014, along the azimuth 200°.

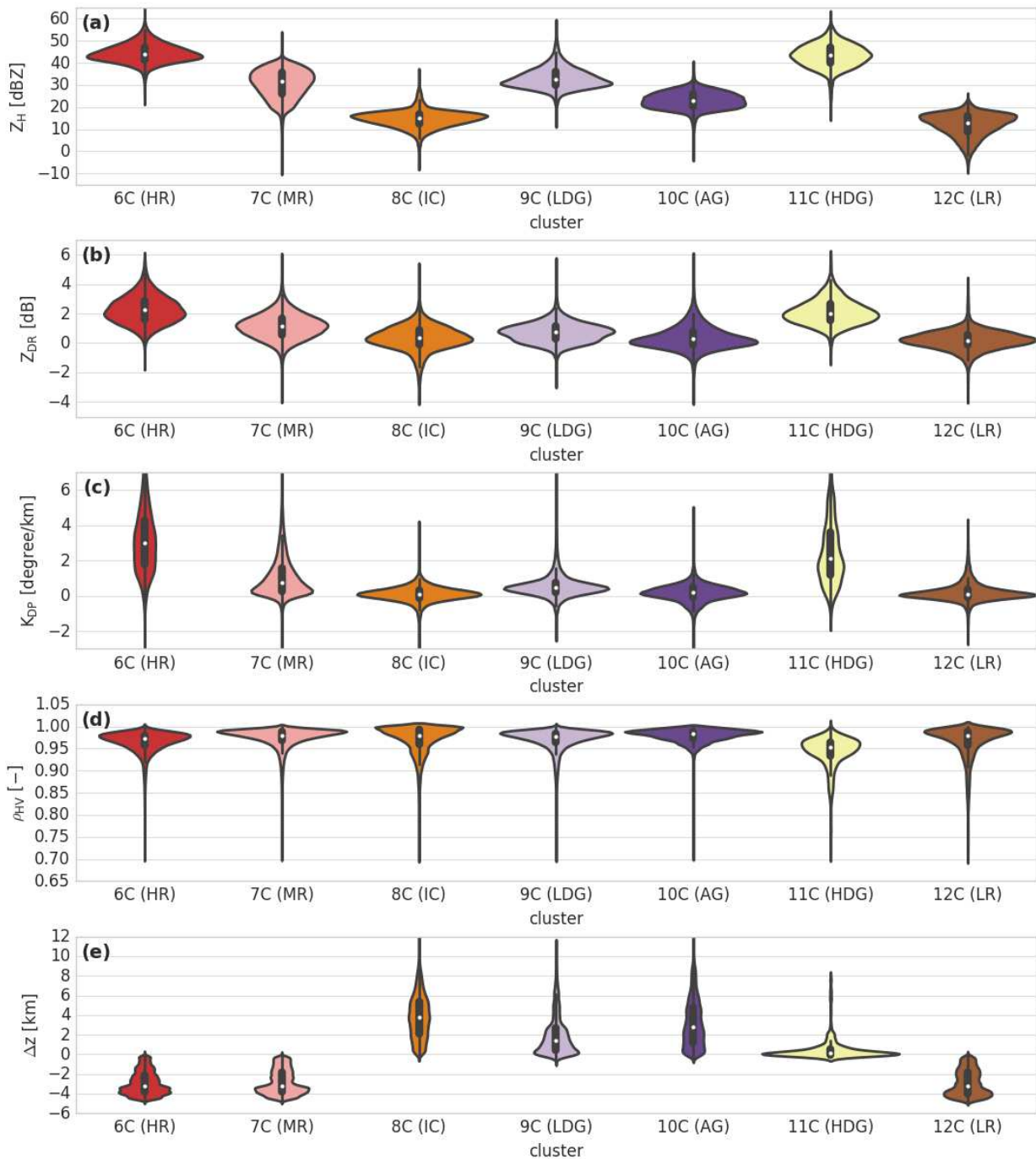


Figure 12: Same as Figure 7, but for the convective regime of the dry season (LR: light rain, MR: moderate rain, HR: heavy rain, LDG: low-density graupel, HDG: high-density graupel, AG: aggregates, IC: ice crystals).

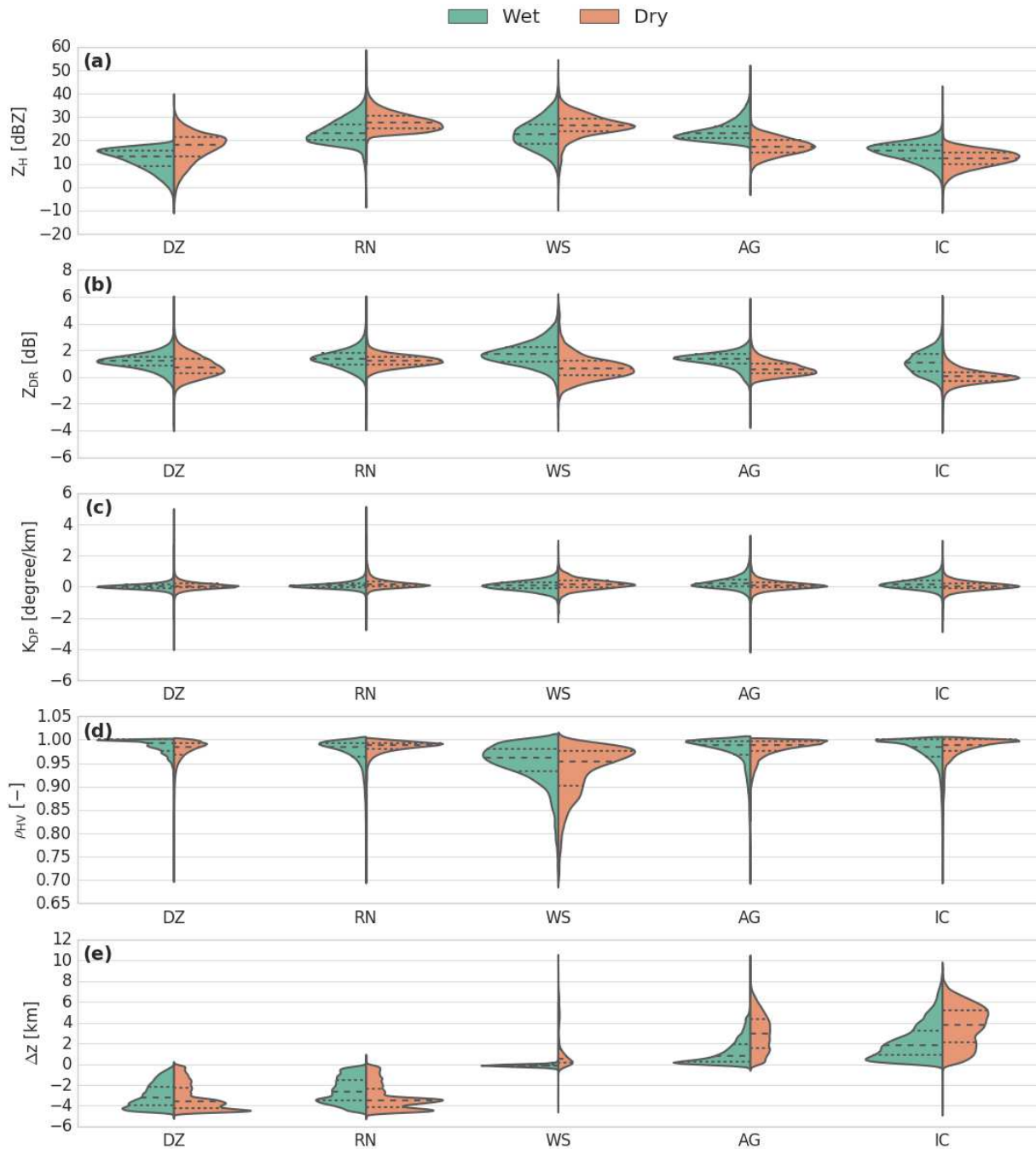
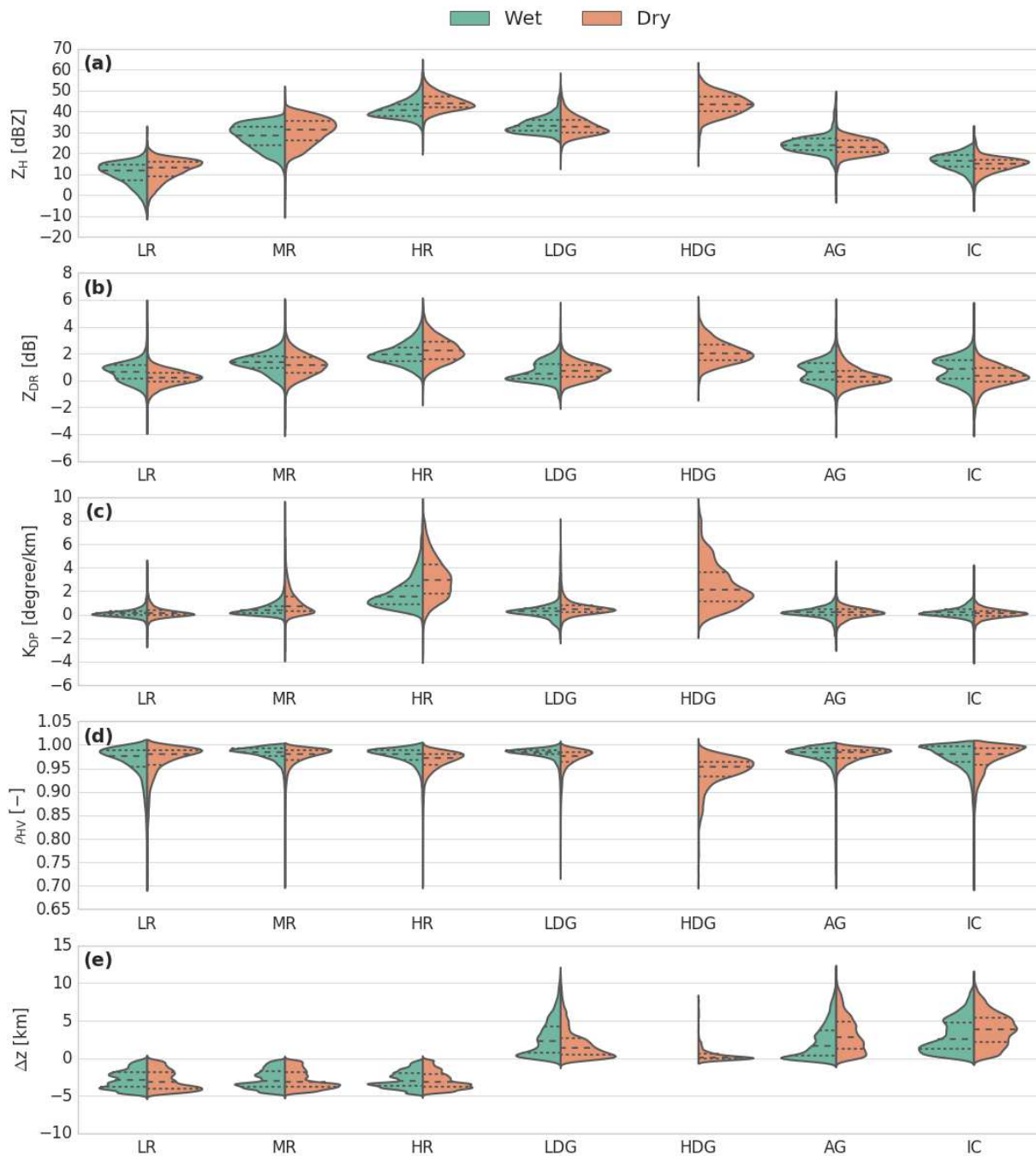


Figure 13: Violin plot comparison of pairs of stratiform hydrometeor types between the wet and dry seasons (DZ: drizzle, RN: rain, WS: wet snow, AG: aggregates, and IC: ice crystals).



1350 **Figure 14:** Same as Figure 13, but for the convective precipitation regime (LR: light rain, MR: moderate rain, HR: heavy rain, LDG: low-density graupel, HDG: high-density graupel, AG: aggregates, and IC: ice crystals).

APPENDIX A: Wet and Dry Season cluster centroids

1355

Cluster	Label	Z _H [dBZ]	Z _{DR} [dB]	K _{DP} [degree/km]	P _{HV} [-]	Δz [km]
1S	Ice Crystals Small Aggregates	17.18	1.17	0.21	0.98	+ 2.23
2S	Aggregates	27.09	1.31	0.27	0.97	+ 1.25
3S	Rain	27.28	1.43	0.10	0.97	- 2.49
4S	Wet Snow	27.54	1.83	0.07	0.95	- 0.10
5S	Drizzle	13.84	1.21	0.02	0.99	- 3.00
6C	Heavy Rain	44.18	2.09	1.88	0.98	- 2.81
7C	Graupel	36.28	0.74	0.34	0.98	+ 2.76
8C	Aggregates	28.94	0.75	0.20	0.98	+ 2.32
9C	Ice Crystals Small Aggregates	17.62	0.91	0.22	0.97	+ 3.07
10C	Light Rain	13.21	0.68	0.14	0.96	- 2.81
11C	Moderate Rain	31.09	1.39	0.50	0.98	- 2.74

Table A.1: Cluster centroids for the wet season.

1360

1365

Cluster	Label	Z _H [dBZ]	Z _{DR} [dB]	K _{DP} [degree/km]	P _{HV} [-]	Δz [km]
1S	Rain	31.43	1.27	0.25	0.98	- 3.12
2S	Drizzle	20.66	0.89	0.07	0.98	- 3.16
3S	Ice Crystals Small Aggregates	13.61	0.11	0.06	0.98	+ 3.65
4S	Wet Snow	29.18	0.85	0.17	0.93	+ 1.40
5S	Aggregates	19.65	0.71	0.11	0.98	+ 3.04
6C	Heavy Rain	46.7	2.38	3.12	0.97	- 2.90
7C	Moderate Rain	34.18	1.24	1.06	0.97	- 2.82
8C	Ice Crystals Small Aggregates	16.69	0.43	0.11	0.97	+ 3.85
9C	Low-Density Graupel	36.79	0.78	0.59	0.97	+ 1.96
10C	Aggregates	24.75	0.45	0.18	0.98	+ 3.20
11C	High-Density Graupel	46.36	2.20	2.50	0.94	+ 0.50
12C	Light Rain	14.47	0.27	0.21	0.97	- 2.89

Table A.2: Cluster centroids for the dry season.

ANEXO 2:

Ribaud, J-F and Machado L.A.T. *Insight into brazilian microphysical convective clouds observed during SOS-CHUVA*. Weather and Forecasting, to be submitted, 2019.

Insights into Brazilian microphysical convective clouds observed during SOS-CHUVA

Jean-François Ribaud¹ and Luiz Augusto Toledo Machado¹

5

¹National Institute of Space Research (INPE), Center for Weather Forecast and Climate Studies (CPTEC), Rodovia Presidente Dutra, km 40, Cachoeira Paulista, SP, 12 630-000, Brazil

10

Submitted to Weather and Forecasting

15

January 2019

20

Correspondence to: Jean-François Ribaud (jean-francois.ribaud@inpe.br)

Abstract.

Although Hydrometeor Classification Algorithms (HCAs) exist since several decades, their potential uses such as an additional tool for nowcasting issues related to high-impact weather events are relatively
25 limited. Here, an unsupervised technique is firstly used to retrieve the dominant hydrometeor types associated with stormy days of the SOS-CHUVA field experiment thanks to an X-band dual-polarization research radar. With this regard, stratiform echoes are composed of five microphysical species (light rain, rain, wet snow, aggregates and ice crystals), whereas convective regions have eight (light/moderate/heavy rain, hail, low/high density graupel, aggregates and ice crystals). Then the
30 dominant microphysical life cycle of 23 severe convective cells is investigated with particular emphasis on their maximum activities in relation to lightning information (mature stage). It is shown that heavy rain, hail, graupels, and aggregates increase in terms of volumes as the SOS-CHUVA convective cells grow up. The time evolution of those four hydrometeor types, and especially graupels and ice crystals which are key microphysical species for thunderstorm electrification, are closely related to lightning
35 rate and could help to prevent subsequent natural hazards associated to severe convective cells.

40

Keywords: hydrometeor classification, tropical microphysics, dual-polarization radar, lightning, nowcasting

1. Introduction

Although worldwide meteorological weather services have made considerable advances over past
45 decades, forecasts accuracy associated to potential high-impact weather events for very short time
periods (nowcasting) are still not yet enough at both space and time scales to avoid or at least
sufficiently mitigate socio-economical disasters (Wilson et al, 1998). Convective storms manifest
through various meteorological systems ranging from isolated thunderstorm to complex Mesoscale
Convective Systems (MCSs). Associated damages caused by those meteorological events can be
50 numerous over very short periods (hail, downburst, flash floods, lightning) and directly may affect
human activities (road safety, flight assistance, power utilities). Therefore, a better understanding of
physical processes at play within these intense events is required in order to improve forecast
capabilities and also to provide objective procedures to meteorologists for anticipating their rapid
evolution.

55 Dual-polarimetric (DPOL) weather radar is one of the most widely and reliable used instruments
nowadays for nowcasting by the research community and the national weather services. By using the
high sensitivity resulting from the combination of two orthogonal polarized microwaves, numerous
benefits have been learned from polarimetric radars for the detection of hazards in convective clouds
over the last 30 years. For instance, the exploitation of polarimetric variables has allowed to improve
60 the detection of damaging hail (Bringi et al, 1986), whereas Ryzhkov et al (2013) have proposed a
method to differentiate the size of hail regardless of the DPOL radar wavelength. Recently, studies have
suggested that precursors of hail could be associated to specific polarimetric radar signatures such as
low coefficient correlation ρ_{HV} or even high specific differential phase K_{DP} for temperatures lower than

0 °C (Picca and Ryzhkov, 2012; Kumjian and Lebo, 2016). Another interesting feature deduced from
65 polarimetric radars is the presence of positive differential reflectivity Z_{DR} columns above ambient 0°C
isotherm, which are directly related to convective storm updrafts (Kumjian et al, 2014). With this
regard, Snyder et al (2015) have developed an algorithm based on the detection of Z_{DR} columns in order
to detect initiation of new intense convective storms and to examine the evolution of related updrafts.
Closely spaced to positive Z_{DR} columnar regions, positive K_{DP} columns above the melting level ($T < 0$
70 °C) have also shown to be good proxies of deep convection updrafts (Hubbert et al, 1998; Kumjian and
Ryzhkov, 2008; Van Lier-Walqui et al, 2016). Finally, the exploitation of polarimetric radar variables
has allowed to improve the forecast of tornadoes by focusing on the low level signatures and especially
the Z_{DR} and K_{DP} footprints (Romine et al, 2008; Kumjian and Ryzhkov, 2008).

One of the most important advantages from DPOL radars is their high sensitivity to hydrometeors and
75 their related ability to discriminate between them (e.g. Vivekanandan et al, 1999; Ryzhkov et al, 2005).
To date, various Hydrometeor Classification Algorithms (HCAs) have been developed by using the
synergy of the dual-polarimetric observables (horizontal reflectivity, Z_H ; Z_{DR} ; K_{DP} ; ρ_{HV}) along with
external temperature information (Park et al, 2009; Dolan and Rutledge, 2009; Al-Sakka et al, 2013;
Dolan et al, 2013; Bechini and Chandrasekar et al 2014; Grazioli et al, 2015; Ribaud et al, 2018; among
80 others). Such HCAs have already demonstrated their utilities by improving quantitative precipitation
estimation and helped to prevent flooding (Giangrande and Ryzhkov, 2008; Boodoo et al, 2015). For
instance, Météo-France's meteorologists have started to use hydrometeor identification as an
complementary reliable nowcasting tool for anticipating potential high-impact severe weather related to
specific convective storms.

85 Microphysical characteristics deduced from polarimetric radar in conjunction with lightning
information have also demonstrated potential benefits in order to better understand convective clouds.
For instance, Schultz et al (2015) have noticed that lightning jumps (rapid increase in lightning activity)
are especially correlated to increases in graupel volume and updrafts characterized by vertical motion
higher than 10 m/s within the [-10°C; -40°C] layer. According to Ribaud et al (2016), graupel volumes
90 are good proxies for lightning initiation, whereas wet hail growth processes may have negative impact on
lightning occurrences. Also, graupel intrusion within ice crystals layer can disturb lightning activity
by producing significantly higher lightning activity (Ribaud et al, 2016). Polarimetric signatures along
with hydrometeor identification have also shown appealing capabilities to diagnose the evolution of
different storm electrification stages in Brazil (Mattos et al, 2016; Mattos et al, 2017). Fuchs et al
95 (2018) have also noticed that anomalous electrical charge structures are mainly associated with larger
and stronger updrafts.

Most of the aforementioned results are, or could be, used by forecasters in their decision-making to
track and put more emphasis on potential hazards in a severe storm. To date, the time evolution of
dominant hydrometeor relative to convective storms is not available in terms of a nowcasting tool. By
100 statistically following the microphysical evolution of convective storms could lead to another objective
diagnose for nowcasting purposes. The present study aims at investigating the temporal evolution of
each hydrometeor type volumes for sets of convective storms that occurred during the SOS-CHUVA
project in Brazil, an extension of CHUVA project applied to nowcasting (Machado et al, 2017). With
this regard, section 2 provides a brief overview of the SOS-CHUVA project and a description of the
105 radar dataset. Section 3 deals with the HCA technique and retrieved hydrometeor types for the São

Paulo region, while section 4 presents the microphysical life cycle of convective cells in terms of volumes and altitudes. Finally, the main conclusions of this study are provided in section 5.

2. Field experiment and datasets

110 The present study is based upon data collected in the state of São Paulo during the SOS-CHUVA project which was conducted during intensive Operation Periods from 2016 to 2018. SOS-CHUVA is a multi-institutional research program focusing on nowcasting of severe weather events that occurred in South-East of Brazil during the wet season (November – March). To achieve this goal, the development of nowcasting tools for improving the forecasts capabilities and providing objective procedures for
115 meteorologists is expected to rely on meaningful results learned from the CHUVA research program (Machado et al, 2014). The ability to get access to the microphysical structures of precipitating systems represents also an important objective of the SOS-CHUVA project. Among all the instruments deployed during this research program, a DPOL X-band weather radar was located in Campinas in complement of pre-existing operational Doppler radar network. Concurrently, dense ground-based observations via
120 raingauges measurements have also been set up in the cities of Piracicaba and Jaguariuna to document intense rain events. Figure 1 shows the map of the facilities used in this particular study.

The DPOL X-band radar was operated in Simultaneous Transmission And Reception (STAR mode) and provided Z_H , Z_{DR} , the differential phase Φ_{DP} , and ρ_{HV} . The polarimetric Campinas radar was designed to perform full volumetric scans every 10 minutes, each cycle was composed of 17 elevations ranging
125 from 0.5° to 50° with a 1.3° beam width at -3 dB. In addition, a vertical pointing scan for calibration purposes along with a 180° RHI scan over the Jaguariuna raingauges network were performed.

The radar raw dataset has been pre-processed according to the procedure presented in Ribaud et al (2018). The processing chain consists in: (i) Z_{DR} calibration by removing offset deduced from vertical pointing in precipitation; (ii) discrimination between nonmeteorological and meteorological echoes; (iii) 130 correction of Φ_{DP} offset and filtering; (iv) estimation of K_{DP} (Hubbert and Bringi, 1995); and (iv) attenuation correction applied to both Z_H and Z_{DR} (Testud et al, 2000). To mitigate as much as possible potential bias or errors, dataset has been restricted to precipitation events wherein the radome was dry. In addition, a high Signal-Noise-Ratio ≥ 10 dB along with a reduced radar coverage ranging from 5 to 60 km have been considered. Finally, the stratiform-convective separation described in Steiner et al 135 (1995) has been applied to the radar dataset from horizontal reflectivity field at a constant altitude plan position indicator (CAPPI) generated at 3 km ($T > 0^\circ\text{C}$).

3. Hydrometeor classification for São Paulo region

3.a) methodology

140 As mentioned in the introduction, there is plenty of HCAs proposed in the literature at all wavelengths and based on the combination of DPOL radar observables (Z_H , Z_{DR} , K_{DP} , ρ_{HV}) and temperature data inferred from radio-soundings or model outputs. In this study one makes the use of two particular hydrometeor identification techniques: (i) the clustering approach, and (ii) the fuzzy logic.

The core of the hydrometeor classification presented in this paper relies on an Agglomerative 145 Hierarchical Clustering (AHC) method, which aims at identifying similar polarimetric observables signatures and gathering them into clusters. This technique is a bottom-up algorithm that considers each observation as a singleton cluster at the outset. Based on their similarities, pairs of clusters are then

iteratively aggregated until all clusters form an unique cluster containing all observations at the end. Finally, a posteriori analysis is performed by the user to determine the optimal number of clusters. With
150 this respect, the reader is referred to Grazioli et al (2015) for background on clustering techniques, and Ribaud et al (2018) for the analysis of the clustering scheme sensitivity. Note that only relevant information that are needed for the understanding of the present analysis are detailed hereafter, while the entire description of the methodology is described in Grazioli et al (2015; hereafter G15) and have been taken over by Ribaud et al (2018; hereafter R18).

155 The AHC method relies on the definition of objects which are five-dimensional vectors defined for each valid radar resolution volume as follows:

$$x = \{Z_H, Z_{DR}, K_{DP}, \rho_{HV}, \Delta z\}$$

and where Δz is the difference between the radar resolution height and the isotherm 0°C deduced either from sounding balloons or NCEP reanalysis. Objects are standardized in order to not mislead the
160 clustering method with the different order of magnitude of each object's components. With this regard, polarimetric radar observations are concatenated into a $[0; 1]$ common space thanks to minimum-maximum boundaries rule, whereas the temperature information is mitigated into a $[0; 0.5]$ range based on a soft sigmoid transformation where 0 (0.5) corresponds to altitude below (over) the brightband. In order to evaluate similarities/dissimilarities between clusters, the Ward linkage rule is considered along
165 with the euclidean distance as metric (R18). As described in G15, the AHC algorithm do not only evaluate similarities/dissimilarities between clusters at each iteration step, but also check the spatial homogeneity of the clustering distribution by assuming a smooth spatial transition between clusters (i.e. hydrometeor types). Once the present setup is complete, the AHC method is applied to a subset of 25

000 observations randomly chosen from the SOS-CHUVA database and before being assigned to the
170 remaining dataset using the nearest clustering rule due to time consuming issues when dealing with very
large dataset.

Concurrently, the X-band fuzzy logic algorithm of Dolan et al (2009; hereafter DR09) has been used to
evaluate the clustering outputs from the AHC method. Initially it allows the discrimination between:
175 Light Rain (LR), Rain (RN), Aggregates (AG), Low Density Graupel (LDG), High Density Graupel
(HDG), Ice Crystals (IC), and Vertical Ice (VI). This classification has been slightly enriched of the Wet
Snow (WS) and Melting Hail (MH) microphysical species by Besic et al (2016) through scattering
simulations. In total, the adapted fuzzy logic allows to distinguish between 10 hydrometeor types and
will refer as DR09 algorithm hereafter.

180

3.b) Hydrometeor classification

According to the AHC method described in section 3.a, the algorithm has been conducted on the DPOL
radar dataset for 13 case studies of intense rainfall events. Initially the AHC method randomly picked
25 000 radar observations considering each of them as a singleton cluster. A simple hierarchical
185 aggregation has been conducted until to reach 50 clusters (i.e. far from the final partition), whereas the
following iteration step has also considered the analysis of the spatial smoothness. This setup has been
separately conducted over both stratiform and convective regions. Here, the clustering outputs retrieved
by the AHC method are identified and associated with their corresponding microphysical species. With
this respect, the choice of the best trade-off about the optimal number of clusters have been manually

190 investigated beforehand, due to the intrinsic high complexity of representing all clustering partitions in this paper. Note that the complete SOS-CHUVA cluster centroids are given in Appendix A.

3.b.1) Stratiform echoes classification

Figure 2 exhibits clustering outputs extracted from an RHI presenting typical stratiform echoes on 3
195 December 2016 in the region of Campinas. Overall, clustering outputs are consistent with hydrometeor types retrieved by the fuzzy logic and DPOL radar signatures. For positives temperatures, clusters 3S and 5S (# referred to the cluster's number and S stands for Stratiform clouds) are in agreement with the DR09 Rain and Light Rain microphysical species, respectively. Nevertheless, one can notice that the fuzzy logic Light Rain ($x[25; 35 \text{ km}]$) ?? is more pronounced than the cluster 5S, whereas the clustering
200 outputs present a more homogeneous region according to cluster 3S. The melting layer, characterized by very low (high) ρ_{HV} (Z_H-Z_{DR}) values, is well represented by the cluster 4S. Note that the DR09 algorithm is mainly driven by temperature information within this specific layer, whereas the clustering algorithm allows to closely follow the DPOL signatures ($x[3; 20\text{km}]$). Finally, negatives temperatures are characterized by clusters 1S-2S which appear to correspond to Aggregates and Ice Crystals regions
205 retrieved by the DR09 algorithm.

To further investigate clusters' characteristics, the Z_H , Z_{DR} , K_{DP} , ρ_{HV} and Δz distributions are represented through violin plots in Figure 3, while the contingency table between the clustering outputs and the microphysical species retrieved by the DR09 algorithm is presented in Table 1. With this regard, clusters 1S and 2S are defined for negative temperatures and are associated with low Z_H and K_{DP}
210 values together with a high coefficient correlation. One can see from the contingency Table 1 that

cluster 1S is mostly divided into Aggregates (47 %) and Ice Crystals (35 %), whereas cluster 2S is related to Aggregates (55%) and Wet Snow (30 %). The main discrepancy between both clusters 1S and 2S relies on Z_H distributions which spread around 17 dBZ and 25 dBZ, respectively. In this respect, R18 has retrieved similar DPOL values for ice crystals and aggregates hydrometeor types associated with stratiform regions in Manaus and one can consider hereafter that cluster 1S correspond to Ice Crystals and cluster 2S to Aggregates. As noticed previously in Figure 2, cluster 4S exhibits all the melting layer characteristics on corresponding violin plots with low ρ_{HV} values (~ 0.91) and high Z_H (~ 40 dBZ) and Z_{DR} (2.9 dB) values. With 75% of agreement with DR09 algorithm cluster 4S is thus associated with Wet Snow hydrometeor type. Finally, only clusters 3S and 5S remain for positive temperatures. Cluster 5S is characterized by lower Z_H and Z_{DR} distributions than cluster 3S, and is mainly associated with Drizzle (95 %) from contingency Table 1. With this regard, one considers that cluster 5S stands for Drizzle and cluster 3S for Rain.

3.b.2) Convective echoes classification

Figure 4 shows a RHI of a convective cell that occurred on 29 November 2016 in the vicinity of Campinas. Overall the cell is characterized by a deep convective “tower” (x[26; 31 km]) that exhibits horizontal reflectivity up to 55 dBZ, high Z_{DR} and K_{DP} values for positive temperatures along with low coefficient correlation. With this respect, one can see that the clustering outputs are in agreement with DPOL signatures. While the DR09 retrieves three hydrometeor types for positive temperatures (Light Rain, Rain, and Melting Hail), the AHC method finds four different clusters (9C-10C-11C-13C). Those clusters seem to gradually follow the gradient of horizontal reflectivity until to define cluster 9C (#

referred to the cluster's number and C stands for Convective clouds) as highly correlated to Z_H up to 50dBZ, Z_{DR} up to 4dB, K_{DP} up to 3°/km, and low ρ_{HV} values (< 0.92). Around the isotherm 0°C, the fuzzy logic scheme exhibits a melting layer defined by the Wet Snow hydrometeor type, whereas either
235 radar observables do not present a bright band signature or clustering outputs. Finally, negative temperatures are characterized by clusters 6C-7C-8C-12C. Clusters 7C-8C seem to correspond to a mix of Low and High Density Graupel from the DR09 algorithm, whereas clusters 6C and 11C are in relation with Aggregates and Ice crystals, respectively.

The violin plots in Figure 5 and the contingency Table 2 allow to fully characterize and identify
240 clustering outputs for the convective regions. With this regard, one can notice that cluster 13C is defined for low Z_H (~ 17 dBZ) and high ρ_{HV} values (~ 0.98), and shares more than 85% with the Drizzle hydrometeor type (Table 2). The main differences between clusters 10C-11C rely on the Z_H and K_{DP} distributions. From the contingency Table 2, cluster 11C is divided into Drizzle (29%) and Rain (57%), while 90% of the cluster 10C correspond to Rain hydrometeor type. Thus, one consider hereafter that
245 clusters 13C-11C-10C stand for Light, Moderate and Heavy Rain, respectively. Cluster 9C is characterized by very high Z_H (~ 51 dBZ), Z_{DR} (4 dB) and K_{DP} (3°/km) distributions along with quite low ρ_{HV} values (~ 0.97). Although it mainly corresponds to Rain, 12% is in agreement with Melting Hail. Note that in the region of Campinas-São-Paulo it is not rare to observe hail during very convective events. Although hail falls have been noticed several times during the SOS-CHUVA, none of the
250 hailpads deployed have unfortunately detected once. Therefore, one let the possibility to discriminate between purely liquid Heavy Rain (cluster 10C) and Melting Hail (cluster 9C). For negative temperatures, half of cluster 6C is associated with Aggregates, $\sim 25\%$ with Low Density Graupel and \sim

20% with Wet Snow. Also, polarimetric signatures agree well with the Aggregates DR09 T-matrix microphysical features and the work of R18. Although cluster 12C presents similar DPOL distributions, 255 the main difference with cluster 6C resides in lower ZH values (19 vs 28 dBZ). According to Figure 4 and those polarimetric characteristics, one attributes cluster 6C to Aggregates and cluster 12C to Ice Crystals. Also defined at $T < 0^{\circ}\text{C}$, cluster 7C is highly in agreement with the Low Density Graupel of DR09 algorithm ($\sim 68\%$) and same hydrometeor DPOL signatures retrieved in R18. Finally, cluster 8C exhibits all the brightband characteristics and shares more than 75% with the Wet Snow (Table 2). As 260 previously noticed on Figure 4, the convective cell do not exhibit a melting layer together with another PPIs and RHIs extracted from the AHC (not shown). With this respect, one might attribute cluster 8C as High Density Graupel, i.e. as ... (Dolan def ???).

3.b.3) Ground validations

265 Although making differences between different types of rain may be somewhat questionable, Figure 6 presents comparisons of hydrometeor types retrieved from the clustering outputs defined for $T > 0^{\circ}\text{C}$ in both stratiform and convective regions, with raingauge measurements observed in both Piracicaba and Jaguariuna sites during SOS-CHUVA (cf. Figure 1). The rationale for this approach is that the clustering outputs should be in agreement with ground observations. The analysis has been performed 270 by considering the 3x3 neighborhood radar measurements for each raingauge station. Overall, one can notice that clustering outputs are in agreement with ground observations. Indeed, stratiform rains are characterized by rain rates (RR) lower than 5mm/h, whereas convective precipitations are defined for

RR ranging in average from 8mm/h to 15mm/h. Note that both convective Heavy Rain and Melting Hail clusters present large distributions and can sometimes reach more than 40mm/h.

275

3.b.4) Discrepancies and similarities with Manaus region

The present hydrometeor classification allows to make a brief comparison with microphysical species retrieved through the work of R18 based on both the same AHC methodology and the DPOL X-band radar deployed during both the Go-Amazon2014/5 (Martin et al; 2017) and ACRIDICON-CHUVA (Wendisch et al, 2016) in the region of Manaus in Amazonas (Latitude: -3.21°; Longitude: -60.60°). Note that Manaus is surrounded by an equatorial forest whereas Campinas is located in a deeply urban region, nearly the Tropic of Capricorn. Overall, one can notice that the stratiform regions exhibit the same hydrometeors in terms of number and types, whereas the convective echoes associated with Manaus wet (dry) season do not show Melting Hail and High Density Graupel (Melting Hail) in comparison to Campinas region cloud microphysics.

Nevertheless, the hydrometeor type presenting the highest difference with Manaus region is the Wet Snow that characterized the melting layer. The Amazonas region is characterized by horizontal (differential) reflectivities around 30 dBZ (1dB) against 40 dBZ (2 dB) in São Paulo. Also, the coefficient correlation is lower in São Paulo than Manaus region (0.91 vs 0.93). This is probably related to the larger ice size and concentration in Campinas region where deep convective processes are stronger than the monsoon convective clouds.

Independently of the region between Campinas and Manaus, the cluster exhibiting the highest similarities in terms of DPOL signatures is the Heavy Rain category associated with convective regions.

This hydrometeor type is always characterized by mean Z_H [43; 47 dBZ], Z_{DR} [2; 3 dB], K_{DP} [2; 3 °/km] and ρ_{HV} [0.97; 0.98]. Although the convective region can be affected by different kinematic and microphysical processes, it appears the dominant hydrometeor types for both Manaus and Campinas regions are very similar whereas the discrepancies are more related to how they are distributed inside the cloud.

300 **4. Microphysical life cycle of convective cells**

Getting access to the microphysical structure of severe weather events that occurred in the vicinity of Sao Paulo is part of the SOS-CHUVA objectives and is essential for assessing the severity of storm's potential. As discussed previously, the development of nowcasting tools for meteorologists is needed to improve weather warnings.

305

4a. Cell tracking and lightning selection

The Forecasting and Tracking the Evolution of Cloud Clusters (ForTraCc, Vila et al; 2008) has been used in order to put emphasis on microphysical life cycle of convective cells. This automated cell tracking algorithm has been adapted to work onto convective-stratiform outputs extracted from the Steiner et al (1995) methodology initially conducted on CAPPIs of Z_H at 3 km ($T < 0^\circ\text{C}$) with a grid resolution of 1km x 1km. By using geometrical overlapping in successive time steps, the ForTraCc system aims at identifying each convective cell (via the center of mass) and following them in both space and time. With this regard, the reflectivity threshold employed was 40 dBZ, and the minimum size considered has been set up to 36 pixels in order to get geometrical overlapping in the 10 minutes

315 time step. Figure 7 presents 23 convective cell trajectories retrieved by the ForTraCC algorithm during the studied period. Overall, one can noticed that convective cells are associated with meteorological events crossing the radar domain from Northwest to Southeast.

According to the identified convective cells, lightning information have been extracted from the BrasilDAT network, which is based on Earth Networks technology. The signals radiations associated
320 with lightning discharges are received in the very large frequency band (1 Hz – 12 MHz), and lightning events (flashes) are retrieved by the Time of Arrival technique. Naccarato et al (2012) assessed the performance of the BrasilDat Network in the vicinity of São Paulo, which is composed of a higher number of sensors than elsewhere in Brazil. The authors found that the network efficiency was up to 88% for cloud-to-ground flashes.

325 In order to gather all the convective cells and explore the general microphysical evolution of the SOS-CHUVA events, lightning information have been considered here to set a t_0 time (synchronizing). With this respect, one assumed that the maximum of lightning activity (normalized by the convective area) corresponds to the maximum convective stage of the convective cell (t_0). Then a time-window of one hour has been considered to put emphasis onto the microphysical life cycle from time evolution ranging
330 from 0 to ± 30 minutes behind/ahead the t_0 time. The choice of one hour interval has been motivated by previous results from TITAN project (Dixon et al, 1993) along with May and Ballinger (2007) which showed that the majority of convective cells exhibit a lifetime less than 60min, although global lifetimes associated to the parent cloud can be longer.

335

4b. Microphysical evolution of convective clouds

The first microphysical aspect that has been investigated relies on the time evolution of volumes of hydrometeor types (Figure 8). With this regard, radar pulse volume has been associated with each hydrometeor type retrieved by the AHC method for the 23 convective cells. Results are presented in terms of “equivalent height”, hereafter referred to as H^* and defined as:

$$H_i(n) = \frac{V_i}{S(n)}$$

where V refers to the volume associated to the hydrometeor type i , and S corresponds to the surface area of the convective cell n . Overall the time evolution of the volumes associated with each hydrometeor type agree quite well with the representation of microphysical life cycle within convective cells (Figure 8a). With this regard, volumes associated with Heavy Rain, Low and High Density Graupel, Aggregates, and to a lesser extent Melting Hail, sharply increase from $t-30$ min before reaching their peaks at t_0 , and progressively decaying afterwards. Those hydrometeor types are well correlated with the time evolution of the convective cell structure which can be divided into initiation, mature, and dissipating stages. Although the evolution of Ice Crystals volumes are similar to those previous hydrometeor types, it presents a delayed by 20 minutes. This is due to the mature-dissipating transition, which acts to die out the storm from the bottom to the top and allows the growth of Ice Crystals for a longer time. Finally, both light and moderate rains exhibit the same signatures with low increase of weak precipitations until t_0 before to sharply strengthen as the storm tends to dissipate. These results indicate that the microphysical life cycle is in agreement with the general representation associated with convective cell in terms of dynamics and model parametrization.

In order to assess the potential from monitoring hydrometeor type volumes for nowcasting perspectives, Figure 8b shows the first time derivative of microphysical volumes in relation to the “mean” convective cell. With this respect, one can noticed that the best precursors are Low and High Density Graupel along with the Aggregates hydrometeor types. They present variations of about 4 m/min between $t-20\text{min}$ and t_0 , and thus could be considered to put more emphasis onto convective cells that present high positive volume variations of Graupels and/or Aggregates. Nevertheless, one should underline that the microphysical cloud representation is highly constrained by radar time resolution to complete an entire volume scan (i.e. 10 minutes here). For instance, microphysical processes may be affected and subject to quicker variations driven by dynamical effects.

365

The time evolution of the mean altitude associated to the solid hydrometeor types ($T < 0\text{ }^\circ\text{C}$) is presented in Figure 9 from the same 23 convective cells extracted from the SOS-CHUVA dataset. While the mean altitude of High Density Graupel does not vary with height significantly and oscillate around 6 km, the Low Density Graupel hydrometeor type raises from 6.5 km to ~ 7.5 km between the initiation to the mature stage of the convective cell. This elevation of Low Density Graupel is particularly in agreement with the electrification processes at play for separating charge within the storm (and known as non-inductive mechanism, Takahashi et al 1978). Indeed, by lifting from 6.5 to 7.5 km this microphysical type reaches cloud environment presenting negative temperatures of about $[-15; -20^\circ\text{C}]$ and according to Krehbiel et al (1986), “strong electrification does not occur until the cloud and precipitation develop above 7-8 km above MSL in the summer, corresponding to air temperature of -15

375

to -20°C ". Finally, both Aggregates and Ice Crystals follow the same evolution, presenting mean altitude differences between the initiation and 10min delayed from t_0 of about 1 km.

5) Conclusion

380 The dominant microphysical species associated with convective systems that occurred during the SOS-CHUVA field experiment have been investigated through combining X-band dual-polarization radar measurements and lightning information.

According to the methodology initially developed by GR15 and the study of R18, an unsupervised HAC method has been developed to retrieve the dominant hydrometeor types of high-impact weather events.

385 With this regard, it has been shown that SOS-CHUVA precipitating systems are composed of five hydrometeor types for stratiform regions (light rain, rain, wet snow, aggregates, and ice crystals), whereas convective echoes are defined by height microphysical species (light/moderate/heavy rain, hail, low/high density graupel, aggregates, and ice crystals). Although the validation of such HCA is a difficult task, it has been shown that ground observations via raingauges are in agreement with the
390 different intensity of convective rains retrieved by the hydrometeor classification. Finally it has been noticed that the diversity of dominant hydrometeor types are quite similar between the tropical city of Campinas located in southeast of Brazil and the equatorial city of Manaus, suggesting that potential microphysical discrepancies may be more related to their own distribution within the cloud through dynamical processes.

395 In a second step, a particular emphasis has been placed on 23 convective cells that occurred during the wet season of the SOS-CHUVA project. Microphysical aspects associated to the critical one hour period

focused on the mature stage of the convective systems have been investigated thanks to retrieved hydrometeor data and lightning information. With this regard, the time evolution of hydrometeor volumes and their respective first time derivative has reveal that heavy rain, low/high density graupel, aggregates and to a lesser extent hail are correlated to the development of the convective cell, making them good precursors for nowcasting tasks. As expected the height evolution related to low density graupel and ice crystals which are key microphysical species in relation to electrification processes, are also a good indicator to the convective cell development and potential resulting lightning.

The present study could be extended by making use of extensive polarimetric radar measurements to reinforce retrieved microphysical properties associated to each hydrometeor type but also by investigating more severe convective cells. Results presented in this paper could be used to constrain and/or validate information derived by high-resolution numerical weather prediction suites, such as microphysical parametrization schemes. Finally, hydrometeor classification and the time evolution of heavy rain, low/high density graupel, and ice crystals volumes will be used by Brazilian forecasters in a near future.

415

Acknowledgements

The authors are thankful to Thiago Biscarro for data acquisition and processing during this study. We
420 also gratefully acknowledge Douglas Uba who performed the adapted cell-tracking algorithm, and Alan
J.P. Calheiros who helped with the raingauges data acquisition and analysis. The contribution of the
first author was supported by the São Paulo Research Foundation (FAPESP) under grants 2016/16932-8
and 2015/14497-0 for the SOS-CHUVA project.

425

430

435

References

- 440 Al-Sakka H, Boumahmoud AA, Fradon B, Frasier SJ and Tabary P. 2013. A New Fuzzy Logic Hydrometeor Classification Scheme Applied to the French X-, C-, and S-Band Polarimetric Radars. *J. Appl. Meteor. Climatol.*, 52, 2328-2344.
- 445 Bechini, R., & Chandrasekar, V. (2015). A semisupervised robust hydrometeor classification method for dual-polarization radar applications. *Journal of Atmospheric and Oceanic Technology*, 32(1), 22-47.
- 450 Bringi, V. N., Vivekanandan, J., & Tuttle, J. D. (1986). Multiparameter radar measurements in Colorado convective storms. Part II: Hail detection studies. *Journal of the atmospheric sciences*, 43(22), 2564-2577.
- 455 Boodoo, S., Hudak, D., Ryzhkov, A., Zhang, P., Donaldson, N., Sills, D., & Reid, J. (2015). Quantitative precipitation estimation from a C-band dual-polarized radar for the 8 July 2013 flood in Toronto, Canada. *Journal of Hydrometeorology*, 16(5), 2027-2044.
- 460 Dixon, M., & Wiener, G. (1993). TITAN: Thunderstorm identification, tracking, analysis, and nowcasting—A radar-based methodology. *Journal of atmospheric and oceanic technology*, 10(6), 785-797.
- 465 Dolan B. and Rutledge SA. 2009. A Theory-Based Hydrometeor Identification Algorithm for X-Band Polarimetric Radars. *J. Atmos. Oceanic Technol.*, 26, 2071-2088.
- 470 Dolan B, Rutledge SA, Lim S, Chandrasekar V and Thurai M. 2013. A robust C-Band hydrometeor identification algorithm and application to a long-term polarimetric radar dataset. *J. Appl. Meteor. Climatol.*, 52, 2162-2186.
- 475 Emersic, C., Heinselman, P. L., MacGorman, D. R., & Bruning, E. C. (2011). Lightning activity in a hail-producing storm observed with phased-array radar. *Monthly Weather Review*, 139(6), 1809-1825.
- 480 Fuchs, B. R., Rutledge, S. A., Dolan, B., Carey, L. D., & Schultz, C. (2018). Microphysical and kinematic processes associated with anomalous charge structures in isolated convection. *Journal of Geophysical Research: Atmospheres*.
- 485 Grazioli, J., Tuia, D., & Berne, A. (2015). Hydrometeor classification from polarimetric radar measurements: a clustering approach. *Atmospheric Measurement Techniques*, 8(1), 149.
- 490 Giangrande, S. E., & Ryzhkov, A. V. (2008). Estimation of rainfall based on the results of polarimetric echo classification. *Journal of applied meteorology and climatology*, 47(9), 2445-2462.

- 480 Hubbert, J., and V. N. Bringi. "An iterative filtering technique for the analysis of copolar differential
phase and dual-frequency radar measurements." *Journal of Atmospheric and Oceanic Technology* 12.3
1995: 643-648.
- 485 Hubbert, J. C. V. N., Bringi, V. N., Carey, L. D., & Bolen, S. (1998). CSU-CHILL polarimetric radar
measurements from a severe hail storm in eastern Colorado. *Journal of Applied Meteorology*, 37(8),
749-775.
- Krehbiel, P. R. (1986). The electrical structure of thunderstorms. *The Earth's electrical environment*,
90-113.
- 490 Kumjian, M. R., & Ryzhkov, A. V. (2008). Polarimetric signatures in supercell thunderstorms. *Journal
of applied meteorology and climatology*, 47(7), 1940-1961.
- Kumjian, M.R., A.P. Khain, N. Benmoshe, E. Ilotoviz, A.V. Ryzhkov, and V.T. Phillips, 2014: The
Anatomy and Physics of ZDR Columns: Investigating a Polarimetric Radar Signature with a Spectral
495 Bin Microphysical Model, *J. Appl. Meteor. Climatol.*, **53**, 1820–1843, <https://doi.org/10.1175/JAMC-D-13-0354.1>
- Kumjian, M.R., and Z.J. Lebo. 2016. Large accumulations of small hail. In 28th Conference on Severe
Local Storms. Portland, OR: American Meteorological Society.
- 500 Machado, L.A.T., E. Freitas, E. Vendrasco, K. Nacaratto, R. Albrecht, D. Vila, A. Avila, F. Pilau, M.
Sanchez, L. Guarino, and J.-F. Ribaud. SOS-CHUVA - A Nowcasting Project. 9th European
Conference on Severe Storms, Pula, Croatia, 18-22 September 2017.
- 505 Machado, L. A., Silva Dias, M. A., Morales, C., Fisch, G., Vila, D., Albrecht, R., ... & Cohen, J. (2014).
The CHUVA project: How does convection vary across Brazil?. *Bulletin of the American
Meteorological Society*, 95(9), 1365-1380.
- Martin, S.T., and coauthors, 2017. The Green Ocean Amazon Experiment (GoAmazon2014/5)
510 Observes Pollution Affecting Gases, Aerosols, Clouds, and Rainfall over the Rain Forest. *Bulletin of
the American Meteorological Society* 98, no. 5 (2017): 981-997.
- Mattos, E. V., Machado, L. A., Williams, E. R., & Albrecht, R. I. (2016). Polarimetric radar
characteristics of storms with and without lightning activity. *Journal of Geophysical Research:
515 Atmospheres*, 121(23).
- Mattos, E. V., Machado, L. A., Williams, E. R., Goodman, S. J., Blakeslee, R. J., & Bailey, J. C. (2017).
Electrification life cycle of incipient thunderstorms. *Journal of Geophysical Research: Atmospheres*,
122(8), 4670-4697.

May, P. T., & Ballinger, A. (2007). The statistical characteristics of convective cells in a monsoon regime (Darwin, Northern Australia). *Monthly weather review*, 135(1), 82-92.

525 Naccarato, K., A. C. V. Saraiva, M. M. F. Sabo, and C. Schumann (2012), First performance analysis of BrasilDat total lightning network in southeastern Brazil, paper presented at International Conference on Grounding and Earthing and 5th International Conference on Lightning Physics and Effects, Bonito, MS, Brazil.

530 Park, H. S., Ryzhkov, A. V., Zrnić, D. S., & Kim, K. E. (2009). The hydrometeor classification algorithm for the polarimetric WSR-88D: Description and application to an MCS. *Weather and Forecasting*, 24(3), 730-748.

Picca, J., & Ryzhkov, A. (2012). A dual-wavelength polarimetric analysis of the 16 May 2010 Oklahoma City extreme hailstorm. *Monthly Weather Review*, 140(4), 1385-1403.

535

Ribaudo, J. F., Bousquet, O., & Coquillat, S. 2016. Relationships between total lightning activity, microphysics and kinematics during the 24 September 2012 HyMeX bow-echo system. *Quarterly Journal of the Royal Meteorological Society*, 142, 298-309.

540 Ribaudo, J.-F., Machado, L. A. T., and Biscaro, T. 2018. X-band dual-polarization radar-based hydrometeor classification for Brazilian tropical precipitation systems, *Atmos. Meas. Tech. Discuss.*, <https://doi.org/10.5194/amt-2018-174>, in review.

545 Romine, G. S., Burgess, D. W., & Wilhelmson, R. B. (2008). A dual-polarization-radar-based assessment of the 8 May 2003 Oklahoma City area tornadic supercell. *Monthly weather review*, 136(8), 2849-2870.

550 Ryzhkov, A. V., Schuur, T. J., Burgess, D. W., Heinselman, P. L., Giangrande, S. E., & Zrnic, D. S. (2005). The Joint Polarization Experiment: Polarimetric rainfall measurements and hydrometeor classification. *Bulletin of the American Meteorological Society*, 86(6), 809-824.

Ryzhkov, A. V., Kumjian, M. R., Ganson, S. M., & Zhang, P. (2013). Polarimetric radar characteristics of melting hail. Part II: Practical implications. *Journal of Applied Meteorology and Climatology*, 52(12), 2871-2886.

555

Schultz, C. J., Carey, L. D., Schultz, E. V., & Blakeslee, R. J. (2015). Insight into the kinematic and microphysical processes that control lightning jumps. *Weather and Forecasting*, 30(6), 1591-1621.

560 Snyder, J. C., Ryzhkov, A. V., Kumjian, M. R., Khain, A. P., & Picca, J. (2015). AZ DR column detection algorithm to examine convective storm updrafts. *Weather and Forecasting*, 30(6), 1819-1844.

Steiner, M., Houze Jr, R. A., & Yuter, S. E. (1995). Climatological characterization of three-dimensional storm structure from operational radar and rain gauge data. *Journal of Applied Meteorology*, 34(9), 1978-2007.

565

Takahashi, Tsutomu. "Riming electrification as a charge generation mechanism in thunderstorms." *Journal of the Atmospheric Sciences* 35, no. 8 (1978): 1536-1548.

Testud, J., E. Le Bouar, E. Obligis, and M. Ali-Meheni, 2000: The rain profiling algorithm applied to polarimetric weather radar. *J. Atmos. Oceanic Technol.*, 17, 332–356.

570

Van Lier-Walqui, M., Fridlind, A. M., Ackerman, A. S., Collis, S., Helmus, J., MacGorman, D. R., ... & Posselt, D. J. (2016). On polarimetric radar signatures of deep convection for model evaluation: columns of specific differential phase observed during MC3E. *Monthly weather review*, 144(2), 737-758.

575

Vila, D. A., Machado, L. A. T., Laurent, H., & Velasco, I. (2008). Forecast and Tracking the Evolution of Cloud Clusters (ForTraCC) using satellite infrared imagery: Methodology and validation. *Weather and Forecasting*, 23(2), 233-245.

580

Vivekanandan, J., D.S. Zrnic, S.M. Ellis, R. Oye, A.V. Ryzhkov, and J. Straka, 1999: Cloud Microphysics Retrieval Using S-band Dual-Polarization Radar Measurements. *Bull. Amer. Meteor. Soc.*, 80, 381–388, [https://doi.org/10.1175/1520-0477\(1999\)080<0381:CMRUSB>2.0.CO;2](https://doi.org/10.1175/1520-0477(1999)080<0381:CMRUSB>2.0.CO;2)

Wendisch, M., and coauthors, 2016. ACRIDICON–CHUVA CAMPAIGN Studying Tropical Deep Convective Clouds and Precipitation over Amazonia Using the New German Research Aircraft HALO. *Bull. Amer. Meteor. Soc.*, 97, 1885–1908, <https://doi.org/10.1175/BAMS-D-14-00255.1>

585

Wilson, J. W., Crook, N. A., Mueller, C. K., Sun, J., & Dixon, M. (1998). Nowcasting thunderstorms: A status report. *Bulletin of the American Meteorological Society*, 79(10), 2079-2100.

590

595

600

LIST OF TABLES

Table 1: Confusion matrix comparing the clustering outputs from the stratiform region and hydrometeor species retrieved from the adapted fuzzy logic.

605

Table 2: Same as Table 3, but for the convective region.

610

LIST OF FIGURES

Figure 1: (a) Geographical localization of the SOS-CHUVA project. (b) X-band DPOL radar domain and its associated topography, together with the raingauges locations for both Piracicaba and Jaguariúna sites.

615

Figure 2: X-band DPOL radar observables and corresponding retrieved hydrometeor classification outputs at 20:37 UTC on 03 December 2016, along the azimuth 19° . DPOL radar observables are shown in panels (a) Z_H , (b) Z_{DR} , (c) K_{DP} , and (d) ρ_{HV} . Comparisons of the retrieved hydrometeor for (e) the clustering method and (f) fuzzy logic scheme. In panel (e), each number corresponds to a different cluster. ‘S’ stands for the stratiform region, whereas ‘C’ is for the convective region.

620

Figure 3: Violin plot of cluster outputs retrieved for the stratiform regime (DZ: drizzle, RN: rain, WS: wet snow, AG: aggregates, IC: ice crystals). The thick black bar in the centre represents the interquartile range, and the thin black line extended from it represents the 95 % confidence intervals, while the white dot is the median.

625

Figure 4: Same as Figure 9, but for an RHI at 20:27 UTC on 29 November 2016,, along the azimuth 19° .

630

Figure 5: Same as Figure 7, but for the convective regime of the dry season (LR: light rain, MR: moderate rain, HR: heavy rain, MH: Melting Hail, LDG: low-density graupel, HDG: high-density graupel, AG: aggregates, IC: ice crystals).

635

Figure 6: Boxplot comparisons for the hydrometeor types defined for $T > 0^\circ\text{C}$ in both stratiform and convective regions with raingauge measurements for the whole dataset period. The black dot represents the mean, whereas the thin black vertical line is the median.

640

Figure 7: Trajectories of convective cells considered. The green and red dots indicate respectively the start and the end if the trajectories.

Figure 8: Time series of (a) the microphysical equivalent heights, (b) the first time derivative of microphysical equivalent heights for the [t-30min; t+30min] life cycle of convective cells. t+0min corresponds to the maximum of lightning activity defined for each individual convective cell.

645

Figure 9: Time evolution of the mean altitude associated to solid hydrometeor types ($T < 0^{\circ}\text{C}$) for the SOS-CHUVA convective cell.

650

655

660

665

TYPE	DZ	RN	MH	WS	AG	LDG	HDG	VI	CR
1S	0.01 %	0.00 %	0.00 %	13.49 %	47.37 %	0.82 %	0.00 %	3.55 %	34.76 %
2S	0.02 %	0.17 %	0.00 %	29.9 %	55.39 %	8.59 %	0.01 %	0.29 %	5.64 %
3S	42.49 %	47.92 %	1.06 %	8.52 %	0.00 %	0.00 %	0.00 %	0.00 %	0.00 %
4S	0.04 %	3.44 %	0.05 %	75.14 %	1.01 %	16.98 %	3.05 %	0.00 %	0.29 %
5S	95.2 %	0.01 %	1.73 %	3.06 %	0.00 %	0.00 %	0.00 %	0.00 %	0.00 %

Table 1: Confusion matrix comparing the clustering outputs from the stratiform region and hydrometeor species retrieved from the adapted fuzzy logic.

670

TYPE	DZ	RN	MH	WS	AG	LDG	HDG	VI	CR
6C	0.09 %	0.10 %	0.00 %	19.19 %	53.33 %	26.88 %	0.02 %	0.16 %	0.24 %
7C	0.00 %	0.68 %	0.28 %	21.76 %	0.00 %	67.82 %	9.47 %	0.00 %	0.00 %
8C	0.37 %	0.61 %	0.05 %	75.33 %	4.49 %	15.01 %	3.70 %	0.15 %	0.29 %
9C	0.00 %	87.88 %	11.94 %	0.18 %	0.00 %	0.00 %	0.00 %	0.00 %	0.00 %
10C	0.01 %	90.33 %	5.41 %	4.25 %	0.00 %	0.00 %	0.00 %	0.00 %	0.00 %
11C	29.42 %	57.30 %	0.44 %	12.84 %	0.00 %	0.00 %	0.00 %	0.00 %	0.00 %
12C	0.08 %	0.00 %	0.00 %	20.00 %	49.49 %	1.23 %	0.00 %	4.33 %	24.87 %
13C	85.38 %	0.34 %	2.26 %	12.01 %	0.00 %	0.00 %	0.00 %	0.00 %	0.00 %

Table 2: Same as Table 3, but for the convective region

675

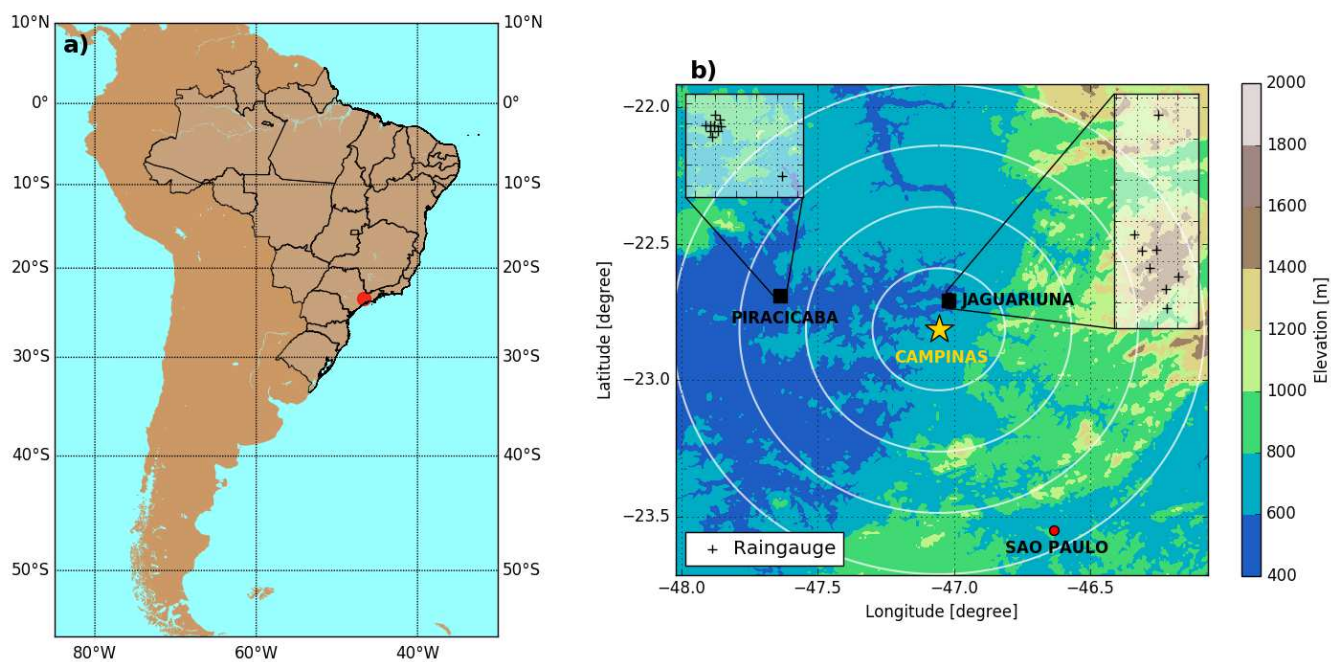
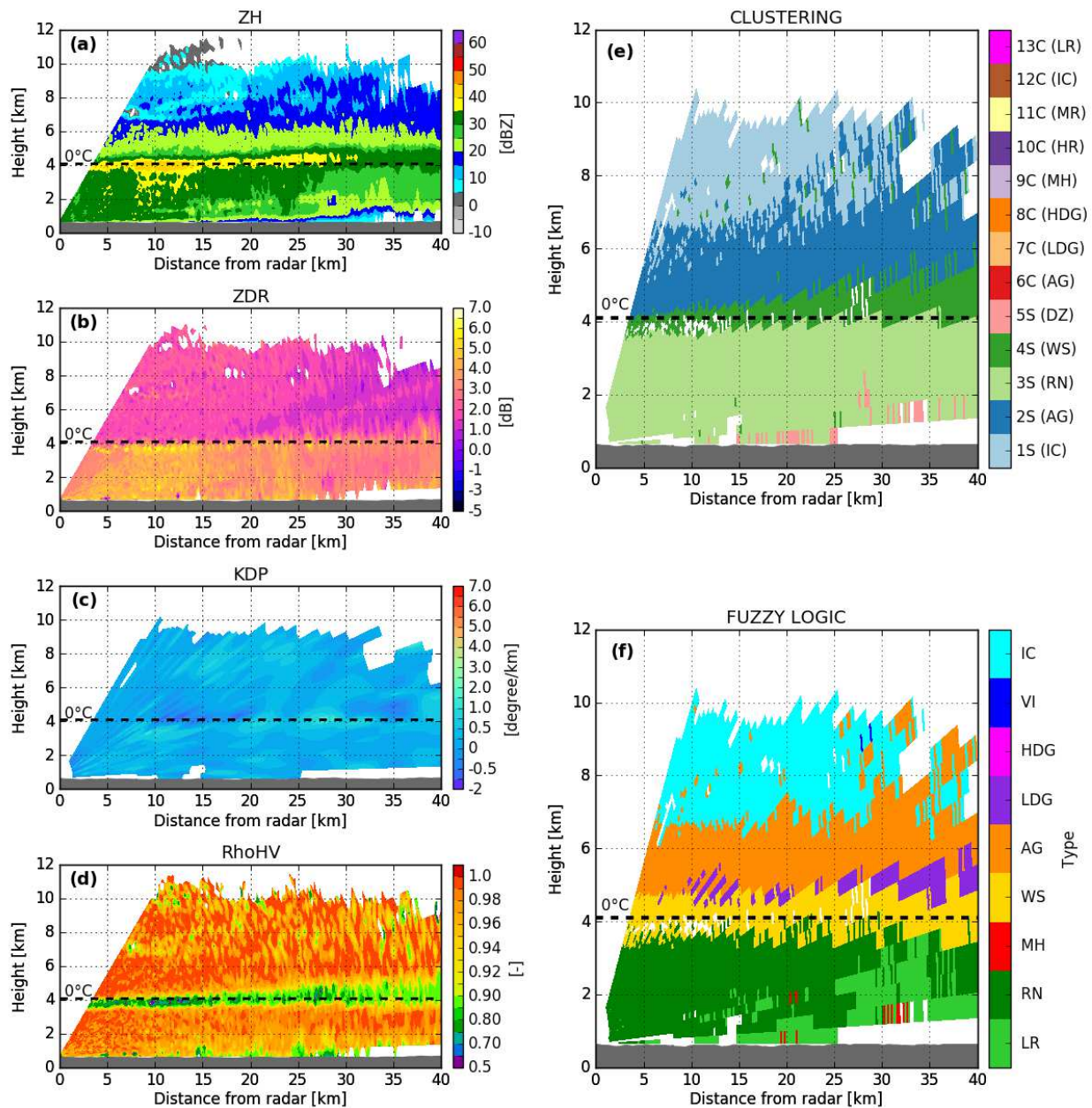
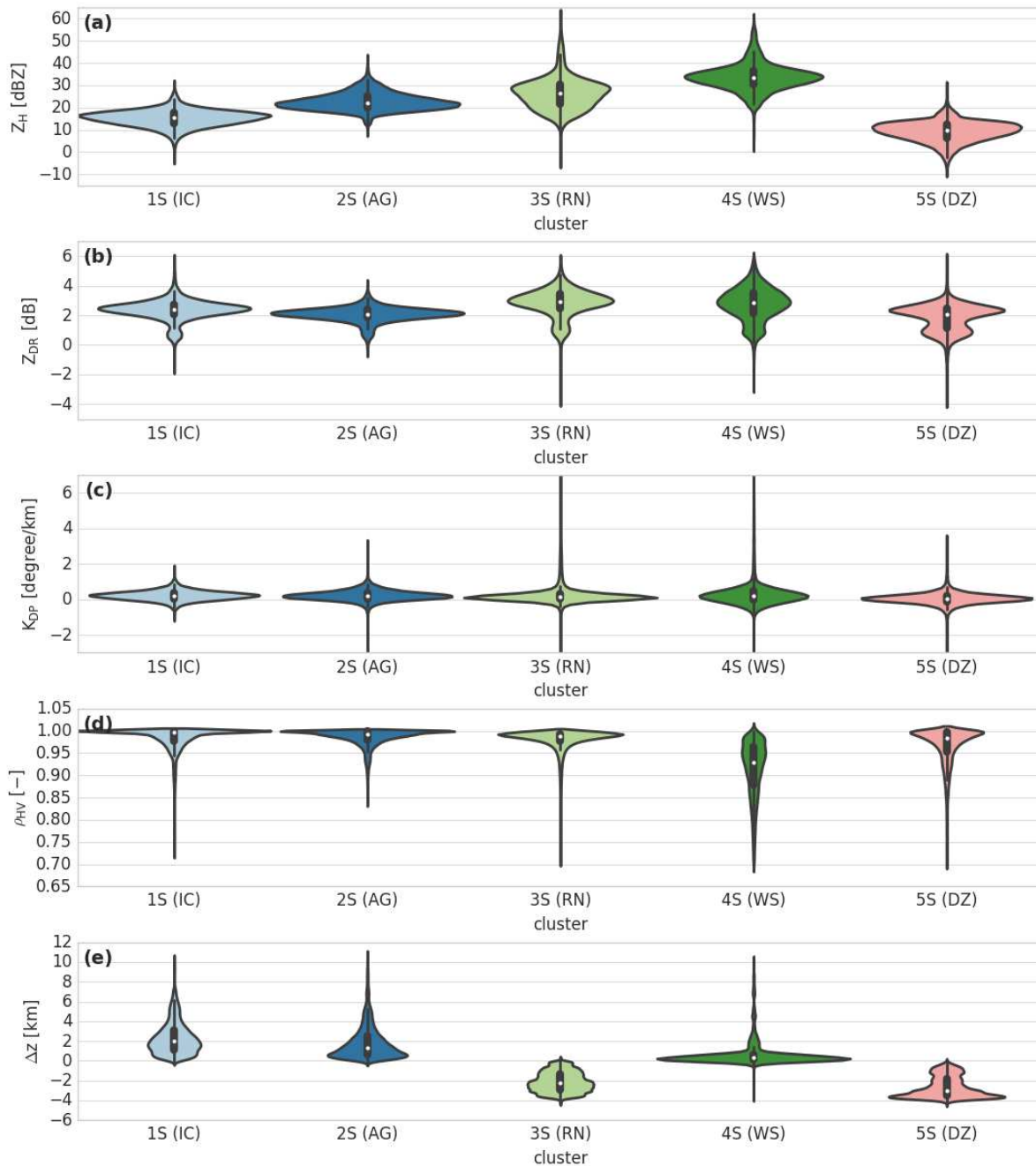


Figure 1: (a) Geographical localization of the SOS-CHUVA project. (b) X-band DPOL radar domain and its associated topography, together with the raingauges locations for both Piracicaba and Jaguariúna sites.

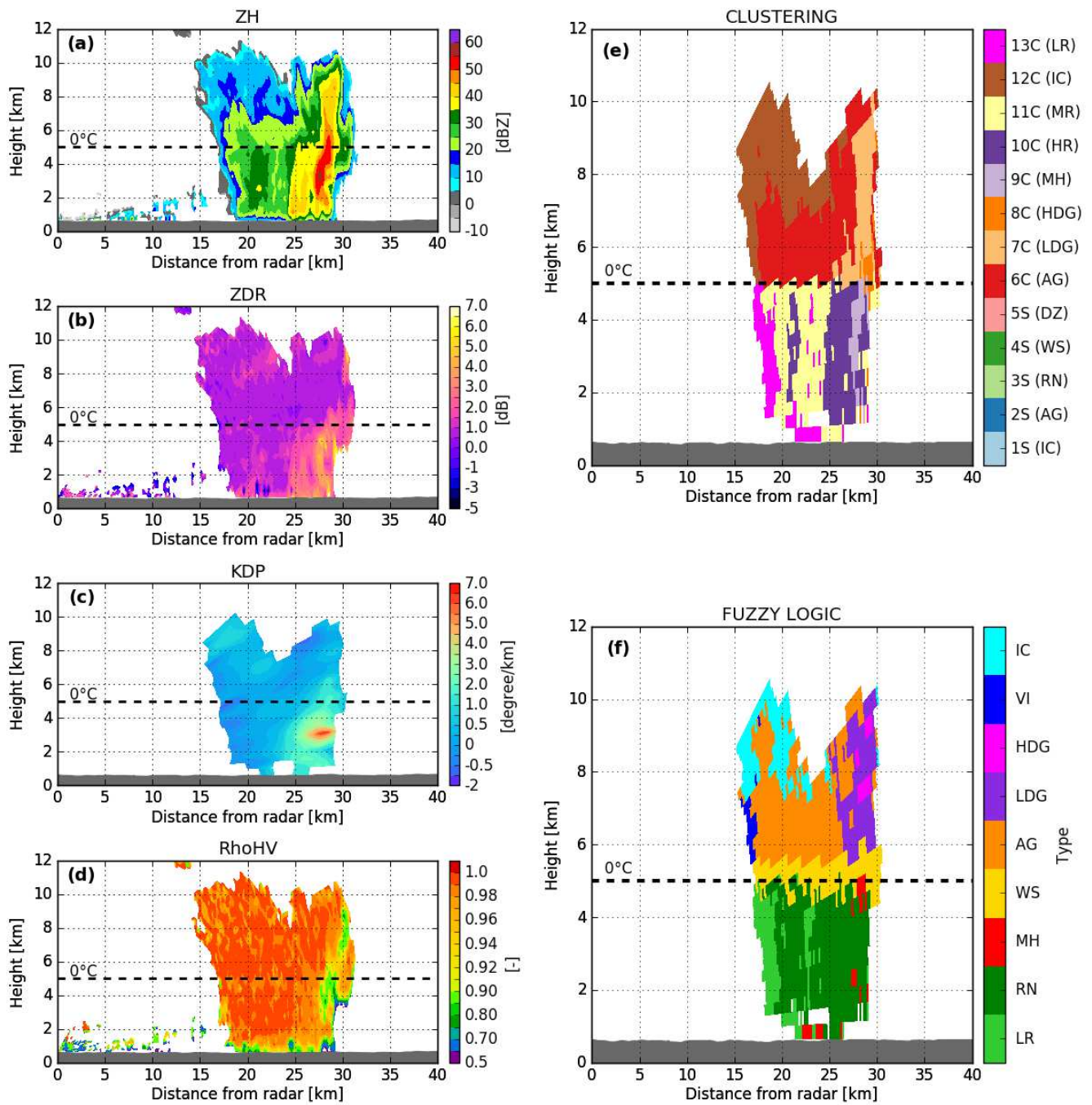
680



700 **Figure 2:** X-band DPOL radar observables and corresponding retrieved hydrometeor classification outputs at 20:37 UTC on 03 December 2016, along the azimuth 19°. DPOL radar observables are shown in panels (a) Z_H , (b) Z_{DR} , (c) K_{DP} , and (d) ρ_{HV} . Comparisons of the retrieved hydrometeor for (e) the clustering method and (f) fuzzy logic scheme. In panel (e), each number corresponds to a different cluster. ‘S’ stands for the stratiform region, whereas ‘C’ is for the convective region.



725 **Figure 3:** Violin plot of cluster outputs retrieved for the stratiform regime (DZ: drizzle, RN: rain, WS: wet snow, AG: aggregates, IC: ice crystals). The thick black bar in the centre represents the interquartile range, and the thin black line extended from it represents the 95 % confidence intervals, while the white dot is the median.



730 **Figure 4:** Same as Figure 9, but for an RHI at 20:27 UTC on 29 November 2016, along the azimuth 19°.

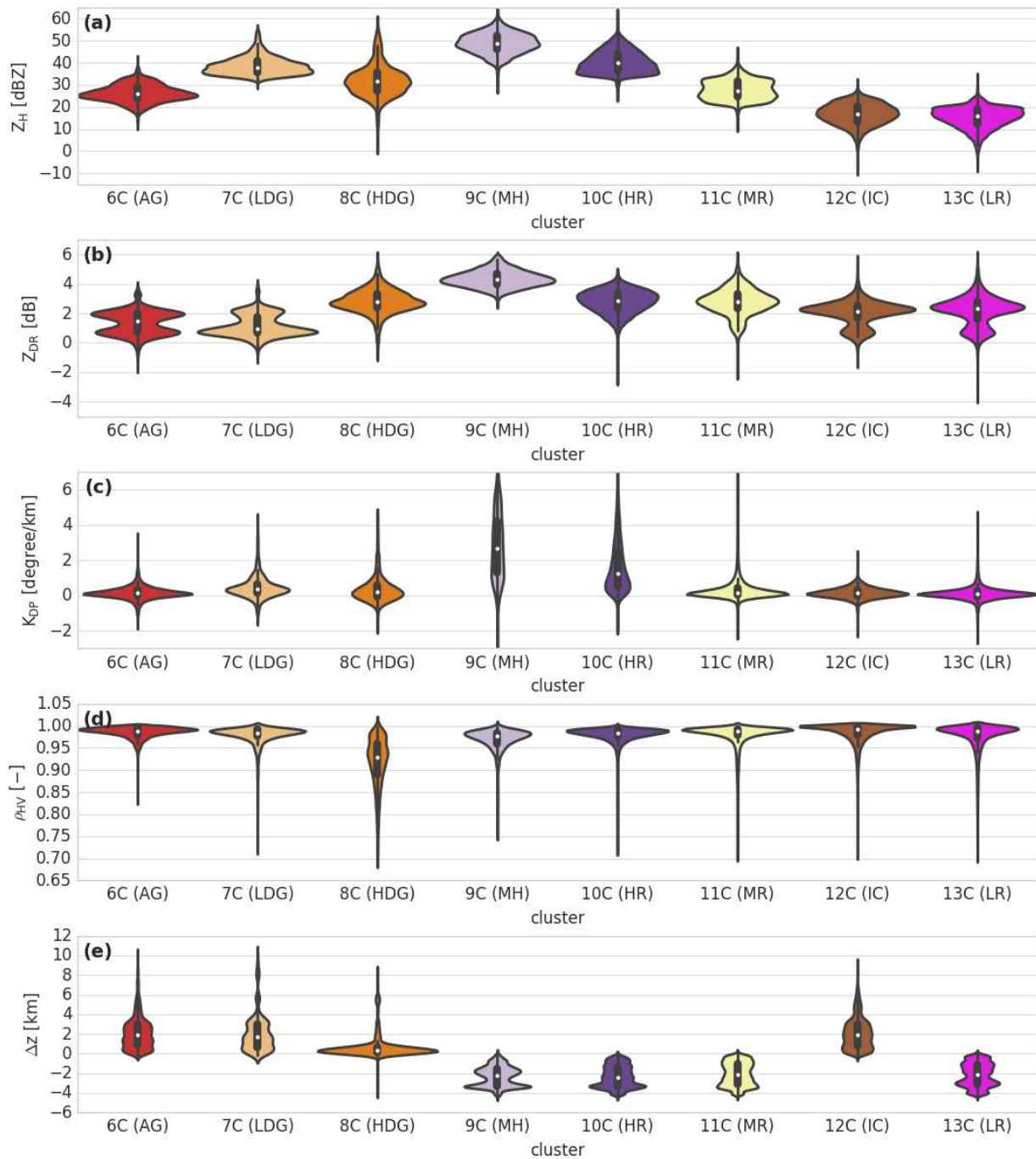


Figure 5: Same as Figure 7, but for the convective regime of the dry season (LR: light rain, MR: moderate rain, HR: heavy rain, MH: Melting Hail, LDG: low-density graupel, HDG: high-density graupel, AG: aggregates, IC: ice crystals).

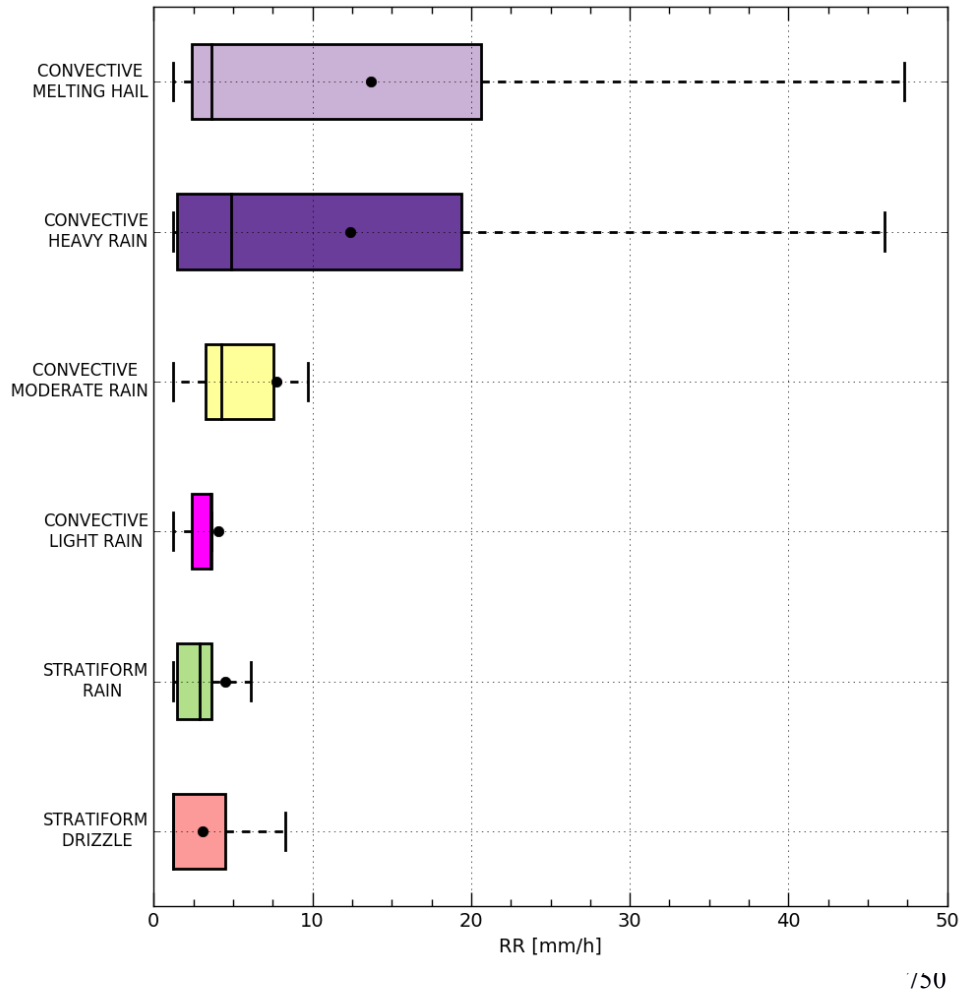
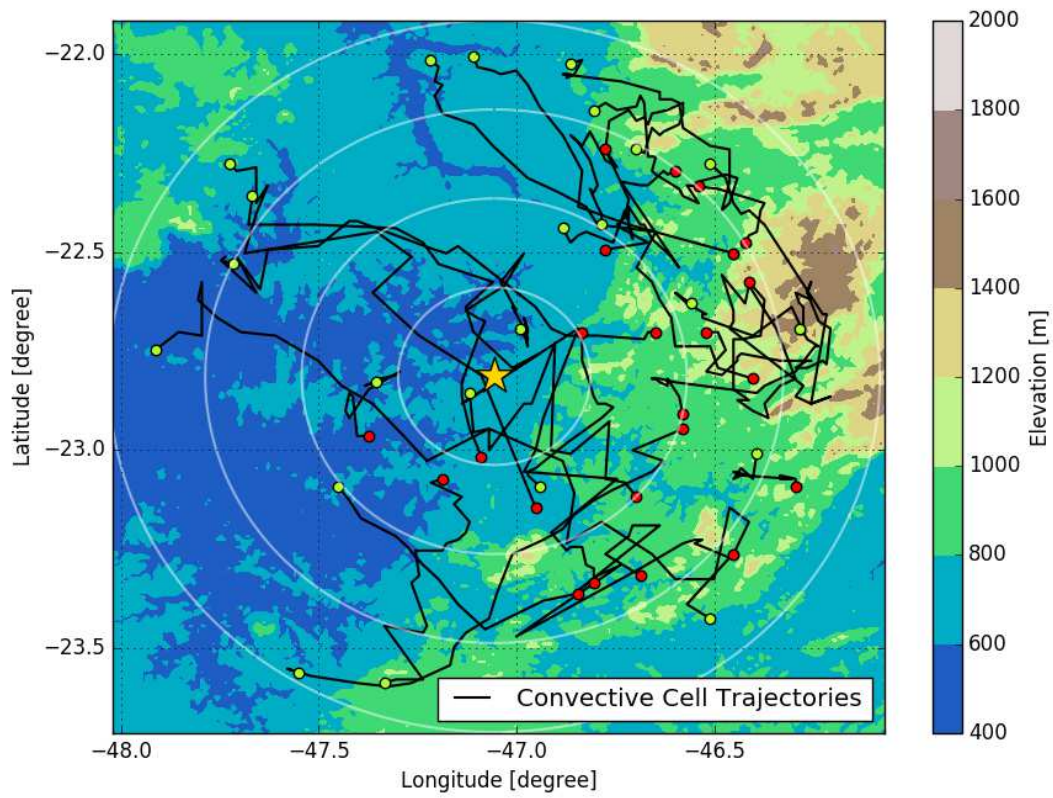


Figure 6: Boxplots comparisons for hydrometeor types defined for $T > 0$ °C in both stratiform and convective regions with raingauge measurements for the whole dataset period. The black dots represent the mean, whereas thin black vertical lines are the median.



775 **Figure 7:** Trajectories of convective cells considered. The green and red dots indicate respectively the start and the end of the trajectories.

780

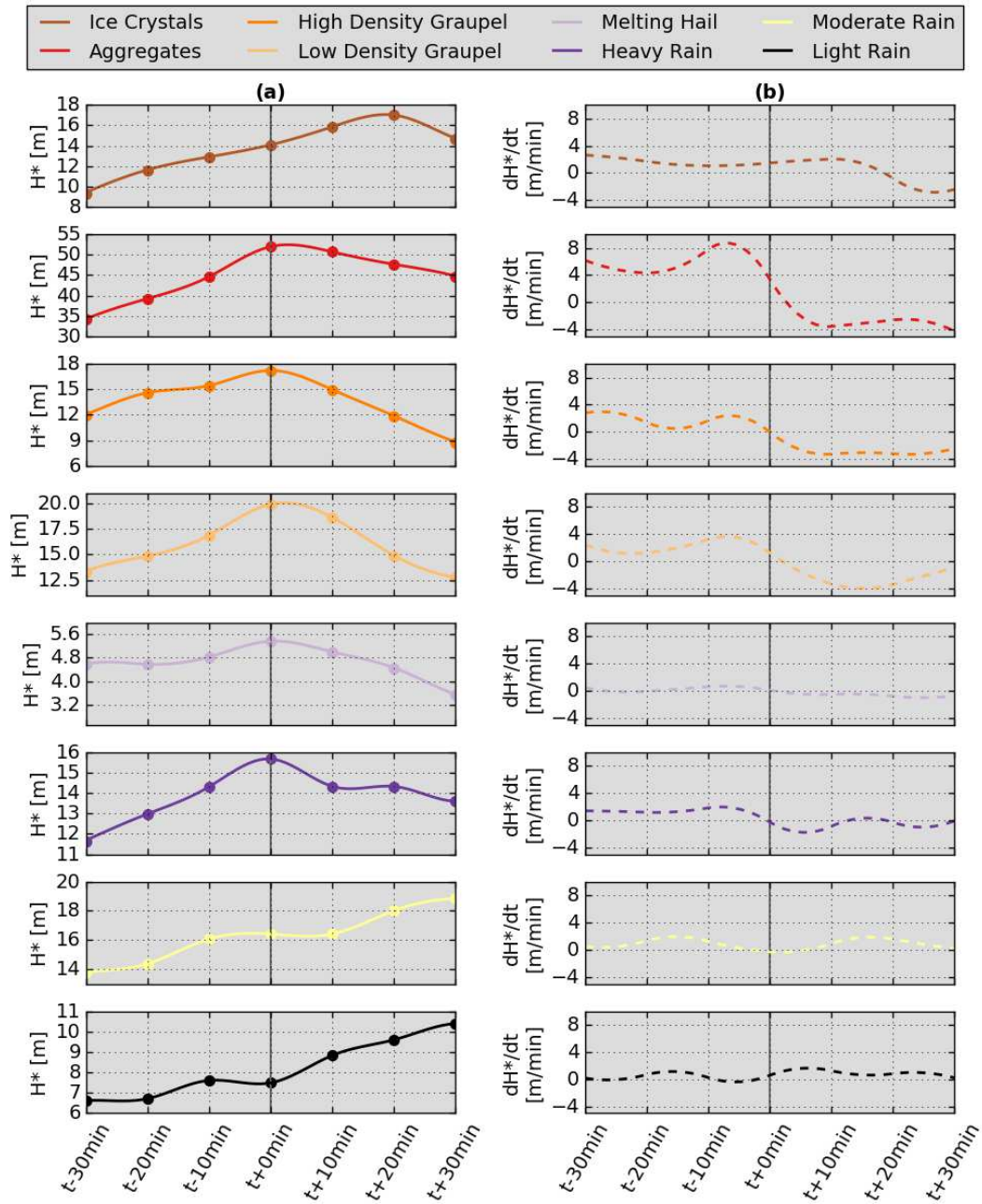


Figure 8: Time series of (a) the microphysical equivalent heights, (b) the first time derivative of microphysical equivalent heights for the $[t-30\text{min}; t+30\text{min}]$ life cycle of convective cells. $t+0\text{min}$ corresponds to the maximum of lightning activity defined for each individual convective cell.

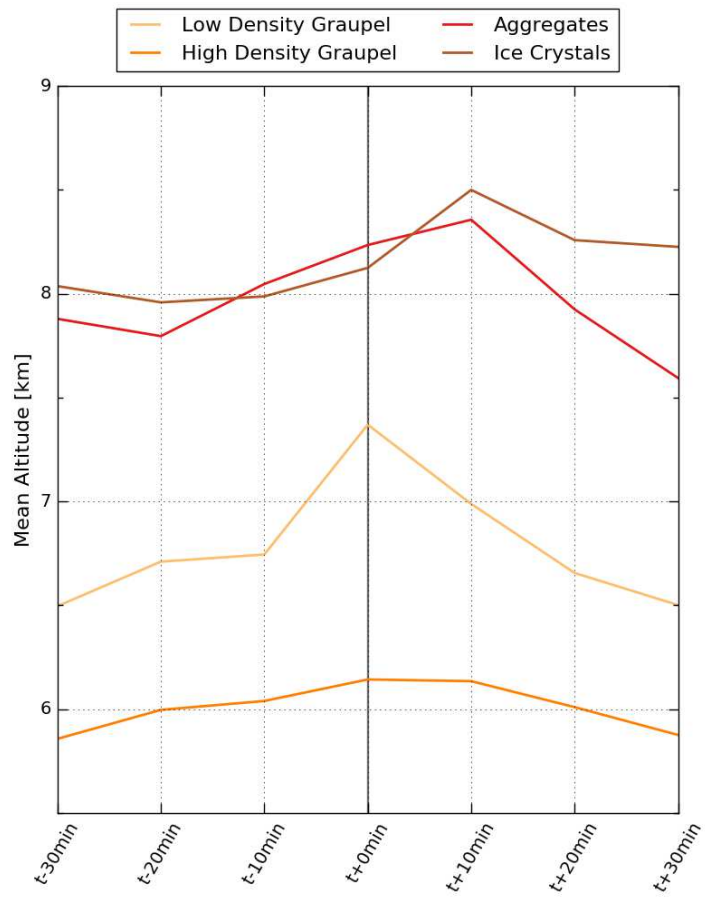


Figure 9: Time evolution of the mean altitude associated to solid hydrometeor types ($T < 0^{\circ}\text{C}$) for the SOS-CHUVA convective cell.

820

825

Appendix A: SOS-CHUVA cluster centroids

Cluster	Label	Z_H [dBZ]	Z_{DR} [dB]	K_{DP} [deg/km]	ρ_{HV} [-]	Δz [km]
1S	Ice Crystals Small Aggregates	16.88	2.42	0.23	0.98	+ 2.33
2S	Aggregates	24.83	2.1	0.23	0.99	+ 1.85
3S	Rain	35.77	2.94	0.27	0.98	- 2.11
4S	Wet Snow	39.83	2.91	0.29	0.91	+ 0.69
5S	Drizzle	11.59	1.94	0.06	0.97	- 2.66
6C	Aggregates	28.08	1.45	0.15	0.99	+ 2.13
7C	Low Density Graupel	41.4	1.24	0.47	0.98	+ 2.09
8C	High Density Graupel	39.48	2.9	0.36	0.92	+ 0.68
9C	Melting hail	51.32	4.39	2.85	0.97	- 2.32
10C	Heavy Rain	43.56	2.88	1.65	0.98	- 2.33
11C	Moderate Rain	30.23	2.88	0.31	0.98	- 2.08
12C	Ice Crystals Small Aggregates	19.14	2.1	0.15	0.98	+ 2.11
13C	Light Rain	17.45	2.28	0.11	0.98	- 2.13

Table A.1: Cluster centroids for the SOS-CHUVA project.

ANEXO 3:

J.-F. Ribaud, L.A.T. Machado, and T. Biscaro. *Dominant Hydrometeor Type Distributions within Brazilian Tropical Precipitation Systems Inferred from X-Band Dual Polarization Radar Measurements.*

Poster, 38th Conference on Radar Meteorology, Chicago, IL, USA, 28 August-1 September 2017.

ANEXO 4:

Declaração de participação na banca examinadora final de aluna de Mestrado – Carolina de Souza

Araújo, 28 de Maio de 2018, INPE/CPTEC, Cachoeira Paulista, SP, Brasil.



Declaração

Declaro para os devidos fins que o (a) **Dr. Jean-François Ribaud** participou da Banca Examinadora Final de :

Aluno (a) *Carolina de Souza Araujo*

Nível *Mestrado*

Curso *Meteorologia*

Título *"A PROPOSAL FOR GLM DATA ASSIMILATION IN CLOUD RESOLVING MODELS".*

Data *28 de maio de 2018*

Horário *14h00min*

Local *Auditório do CPTEC em Cachoeira Paulista*

Membros da Banca Examinadora

Dr. Éder Paulo Vendrasco	Presidente	INPE
Dr. Luiz Augusto Toledo Machado	Orientador(a)	INPE
Dr. Jean-François Ribaud	Orientador(a)	INPE
Dr. Christian Kummerow	Convidado(a)	CSU

São José dos Campos, 28 de maio de 2018

Dr. Éder Paulo Vendrasco
Presidente da Banca Examinadora